



HAL
open science

Swelling induced debonding of thin hydrogel films grafted on silicon substrate: the role of interface physical-chemistry

Anusree Augustine

► To cite this version:

Anusree Augustine. Swelling induced debonding of thin hydrogel films grafted on silicon substrate: the role of interface physical-chemistry. Material chemistry. Université Paris sciences et lettres, 2022. English. NNT: 2022UPSLS040 . tel-03994884

HAL Id: tel-03994884

<https://pastel.hal.science/tel-03994884v1>

Submitted on 17 Feb 2023

HAL is a multi-disciplinary open access archive for the deposit and dissemination of scientific research documents, whether they are published or not. The documents may come from teaching and research institutions in France or abroad, or from public or private research centers.

L'archive ouverte pluridisciplinaire **HAL**, est destinée au dépôt et à la diffusion de documents scientifiques de niveau recherche, publiés ou non, émanant des établissements d'enseignement et de recherche français ou étrangers, des laboratoires publics ou privés.



THÈSE DE DOCTORAT
DE L'UNIVERSITÉ PSL

Préparée à l'Ecole Supérieure de Physique et de Chimie
Industrielles de la ville de Paris (ESPCI Paris)

Sciences et Ingénierie de la Matière Molle (SIMM)

**Décollement induit par le gonflement
de films minces d'hydrogel greffés sur un substrat de
silicium : rôle de la physico-chimie de l'interface**

**Swelling induced debonding of thin hydrogel films grafted on
silicon substrate: the role of interface physical-chemistry**

Soutenue par

Anusree AUGUSTINE

Le 23 septembre 2022

Ecole doctorale n° 397

**Physique et chimie des
Matériaux**

Spécialité

Chimie des Matériaux

Composition du jury :

| | |
|---|------------------------------|
| Olivier SANDRE Directeur de recherche, LCPO - Bordeaux | <i>Président</i> |
| Olivier FELIX Chargé de recherche, ICS – Strasbourg | <i>Rapporteur</i> |
| Frédéric RESTAGNO Directeur de recherche, LPS - Paris-Saclay | <i>Rapporteur</i> |
| Corinne SOULIE-ZIAKOVIC Maître de conférences, C3M - ESPCI Paris | <i>Examinatrice</i> |
| Yvette TRAN Maître de conférences, SIMM - ESPCI Paris | <i>Directrice de thèse</i> |
| Antoine CHATEAUMINOIS Directeur de recherche, SIMM - ESPCI Paris | <i>Co-directeur de thèse</i> |

Acknowledgement

I extend my most sincere gratitude to my three academic supervisors: Antoine Chateauminois, Emilie Verneuil and Yvette Tran. In these three years the guidance given by them was amazing. Thanks a lot for all the advises given to me. As this Ph.D. had different subjects, you were very patient and taught me everything throughout the journey. You were very good teachers and tried to listen to me. I am very grateful for that.

I also take this opportunity to thank my funding, UPToParis, which is a MSCA cofund, cofunded by Saint-Gobain Research Paris. Thanks to Alexandra Marynets, Lucie Ebran, Virginie Cardoso from UPToParis who helped from the beginning of my Ph.D. to the end. Thanks to Jessica Delavoipière, Jérémie Teisseire, and Bertrand Heurtefeu from Saint-Gobain Research Paris, whom I always had a very efficient discussion.

I am thankful to the collaborations during my Ph.D., Marc Veillerot, Nicolas Gauthier at LETI, CEA Grenoble and Chung Yuen Hui and Bangguo Zhu at Cornell University. It was really great working with them.

I would like to express my gratitude to the members of the jury who took the time to read and comment on my manuscript as well as for the very rich scientific discussion that we had during the defense.

I am so grateful to Bruno Bresson who helped me to do AFM. Mohamed Hanafi who taught me to do TGA and GPC. Ludovic Olanier helped me in these three years with different needs from workshop. Fabienne Decuq and Mayu Hirano-Courcot did all the administration things for me. Armand Hakopian was always there to help every time when I needed.

During these three years, I have to specially thank Ekkachai Martwong who helped me to synthesize polymers. Guillaume Votte, Claire Schune, Zuxiang Xu and Lola Ciapo whom I had different fruitful discussion during my Ph.D.

I would like to thank Etienne Barthel, the director of the SIMM laboratory. Artem with whom I always had nice discussions. Hélen for all the croissants and positive vibes you gave me.

SIMM always supported me mentally and academically a lot. The office H 204 has been my family in last three years. Victroria Waltz, Aude Belguise, Noushin Hasanabadi, Gaétan

Grimaldi D'esdra, and Léa Milenkovic were my second family. Victroria Waltz, Aude Belguise and Léa Milenkovic without their mental support it was impossible to finish my Ph.D. They also introduced me to French culture, food etc. French classes in the office was always the best. I will be always grateful for them.

I like to specially thank Pascal Schlozen, Flora-Maud Le Menn, Lucile barbier and Julie Brun who became my great friends, whom I could ask help every time. They welcomed me with their whole heart. All the food, Opera and cooking, we did together are my souvenir for my life. I also like to thank all the people from my year of Ph.D.

All the others in SIMM were great to me. It is difficult to tell each names, but I like to specially thank Gabriel, Yuanyuan, Raquel, Ombeline, Maxime, Hao, Mathieu, Hao, Mohammad, Akash, Alex, Atul, Krupal, Lilly and Lazar who helped me in this journey being good friends.

I have to specially thank Kondareddy, Aruna, Kiran, Drupitha and Mahima. Their support and care was priceless.

Last but not least I would like to thank my family, my Appa, Amma and Achu without them it was impossible to reach here. I also like to thank Hanuman who helped me every day for the last three years.

വഴിയിലെ

കൊച്ചു കാട്ടുപൂവിനും

മുകളിലെ കിളിപ്പാട്ടിനും നന്ദി

മിഴിയിൽ വറ്റാത്ത

കണ്ണുനീരിനും

ഉയിരുണങ്ങാത്തലിവിനും

നന്ദി.....

സുഗതകുമാരി (നന്ദി)

Chapter 2. Surface-attached hydrogel films with controlled interfacial strength

| | |
|--|----|
| and defects | 41 |
| 1. Introduction..... | 44 |
| 2. Experimental Methods..... | 47 |
| 2.1. Synthesis of thin films..... | 47 |
| 2.1.1. Materials..... | 47 |
| 2.1.2. Synthesis of ene-functionalized PDMA..... | 47 |
| 2.1.3. Variation of the grafting density by mixing silanes..... | 48 |
| 2.1.4. Preparation of mask for lithography..... | 48 |
| 2.1.5. Passivation of thiol..... | 49 |
| 2.1.6. Preparation of surface-attached PDMA hydrogels..... | 49 |
| 2.2. Characterization techniques..... | 49 |
| 2.2.1. Contact angle measurements..... | 49 |
| 2.2.2. Spectroscopic Ellipsometry..... | 50 |
| 2.2.3. Microscopic Ellipsometry..... | 51 |
| 2.2.4. X-ray Photoelectron Spectroscopy..... | 51 |
| 2.2.5. ToF-SIMS..... | 51 |
| 2.2.6. Debonding experimental set-up..... | 52 |
| 3. Results and Discussion..... | 53 |
| 3.1. Preparation of surface-attached hydrogel films using CLAG strategy..... | 53 |
| 3.2. Control of the interfacial strength by varying the grafting density..... | 55 |
| 3.3. Control of local defects by passivation of thiol..... | 58 |
| 3.4. Swelling-induced wrinkles and delamination of surface-attached hydrogel films.... | 61 |
| 4. Conclusion..... | 64 |
| 5. References..... | 66 |
| 6. Supporting Information..... | 71 |

| | |
|--|------------|
| Chapter 3. Swelling induced debonding of hydrogel / substrate interface | 79 |
| 1.Introduction | 81 |
| 2.Swelling equilibrium of hydrogel networks..... | 81 |
| 2.1. Deformation free energy..... | 82 |
| 2.2. Swelling equilibrium | 84 |
| 2.2.1. Isotropic swelling | 84 |
| 2.2.2. Swelling of hydrogel film attached to a rigid substrate | 85 |
| 2.2.3. Plane strain swelling of a thin film..... | 85 |
| 2.3. Swelling stresses..... | 86 |
| 2.4. Discussion..... | 87 |
| 3.Experimental setup..... | 88 |
| 4.Overview of debonding mechanisms | 90 |
| 4.1. Phone cord debonding mechanisms | 90 |
| 4.2. Dendritic delamination patterns..... | 94 |
| 4.3. Phase diagram for debonding mechanisms | 95 |
| 5.Debonding in the phone cord regime | 96 |
| 5.1. Measurement of the debonding velocity | 96 |
| 5.2. Relevance of buckling stresses to delamination mechanisms | 97 |
| 5.3. Dependence of transverse velocity on time..... | 99 |
| 5.4. Threshold thickness for the occurrence of debonding..... | 104 |
| 6.Theoretical crack model..... | 106 |
| 7.Discussion | 108 |
| 8.Conclusion..... | 110 |
| 9.References | 110 |
| General conclusion and perspectives..... | 113 |
| APPENDIX A: Ellipsometry | 117 |
| APPENDIX B: Theoretical interface crack model..... | 125 |

Introduction

Hydrogels are transparent and hydrophilic polymer networks that absorb a lot of water. As such, these systems are used either for their remarkable lubricating properties, for their ability to absorb water or to release it in response to a physico-chemical stimulus. More precisely, the lubricating properties of polymer hydrogels in aqueous environments are of paramount importance in many biological systems (articular cartilages, or mucin layers on the surface of the cornea,...) and in biomedical engineering (contact lenses,...), where they can provide very low friction. Besides, water sorption by gel films is found to delay mist formation, which makes them suitable candidates for anti-mist coatings. Finally, the swelling and deswelling ability of responsive hydrogels has been advantageously used in the development of soft robotics or switchable traps in microfluidics. Hence, both the lubricating properties, the ability to swell and deswell with water, together with their transparency and biocompatibility, make hydrogels promising candidates for the development of coatings on substrates with the aim of tuning the surface functionality. However, the long-term durability of hydrogel coatings is conditioned by their resistance to delamination from the substrate. More precisely, coatings inherently bear large geometrical aspect ratios where their thickness is far thinner than their lateral size. As a result, swelling only occurs by increasing the coating thickness as long as the coating is attached to the substrate. This constrained swelling results in the onset of internal lateral stresses within the coating which may cause the debonding of the film from the substrate. Therefore, the debonding of hydrogel coatings is expected to depend on the swelling ratio, their thickness, and the strength of the interface between gel film and substrate.

In the literature, these swelling stresses were evidenced from the resulting elastic instabilities that develop at the free surface of swollen gel films: when the gel is attached or constrained laterally, its surface is observed to buckle into wrinkles, creasing, etc... while the film remains attached. On the other hand, other works report on the buckling of locally non-grafted gel films, with a focus on the morphology of the blisters formed.

In the present work, we offer to experimentally study the onset of propagation of debonding at the gel/substrate interface of a hydrogel coating when it swells. From the literature, we identify the following control parameters: the swelling ability of the gel, which controls the internal swelling stresses, interfacial strength, and coating thickness. To do so, we first developed a model system with well-defined properties, namely hydrogel films of controlled thickness and homogeneous swelling ratio that are grafted on a substrate with covalent bonds of well-controlled and varied surface density in order to set the interfacial strength with the substrate. Care was taken to precisely characterize these films in all these aspects. In addition, the nucleation of delamination was also controlled using localized defects in the grafting of the gel films. A homemade set-up was then developed to measure the debonding dynamics of these films in an atmosphere of set humidity. The onset of delamination was then modeled within a theoretical description we developed that allows us to rationalize the conditions for which delamination propagates depending on the interfacial strength.

This manuscript is composed of three chapters.

Chapter 1 includes the state of the art and details the objectives of this work. I will review the literature on the swelling stresses within constrained hydrogels and on morphologies of the free surface of the swollen gel, whether they are grafted on a substrate or not. This chapter is also devoted to a review of the different strategies available in the literature to make polymer films, to create an interfacial defect, and also to control the grafting density of the film on the substrate. The objective of this dissertation is then exposed.

Chapter 2 is devoted to our synthesis of the hydrogel films and characterization of their properties. Surface-attached poly(*N*, *N*-dimethylacrylamide) (PDMA) hydrogel thin films are prepared on silicon wafers. Then a new strategy is developed to create a well-controlled defect at the interface of the hydrogel and the substrate. Well-controlled line defects with low adhesion (width between 2 and 100 μm) are created on the substrate from the passivation of the reactive thiol groups on the surface of the silicon wafer by allyl butyl ether using microlithography techniques. And also, a new strategy is developed to vary the grafting density on the surface of the substrate. For that purpose, the silicon wafer is grafted with mixtures of mercaptosilane and propylsilane in various proportions prior to thin film deposition.

Chapter 3 is dedicated to the investigation of the debonding processes of a swollen hydrogel film from its substrate in relation to the grafting density at the film/substrate interface. For that purpose, we have developed a methodology consisting in monitoring the initiation and the propagation of swelling-induced delamination from well-controlled preexisting interfacial defects. We measured the velocity at which the hydrogel debonds. Our results are then discussed in light of a theoretical fracture mechanics model which allows to extract quantitative values of the interface strength as a function of the grafting density.

1. State of the art

RÉSUMÉ

Les revêtements d'hydrogel sont des réseaux de polymères transparents et hydrophiles capables d'absorber plusieurs fois leur épaisseur en eau. Cependant, les contraintes induites par le gonflement du film peuvent entraîner un décollement préjudiciable de l'hydrogel ce qui peut limiter l'utilisation pratique de ces revêtements. Dans cette étude, nous proposons de décrire les mécanismes de décollement de films minces d'hydrogel en fonction de leur densité de greffage à l'interface film/substrat. Le but est de pouvoir contrôler et prédire la dégradation des revêtements hydrogel pendant le gonflement ou sous des contraintes de contact. Ce chapitre présente l'état de l'art et détaille les objectifs de ce travail. Il comprend la revue de la littérature sur les contraintes de gonflement au sein d'hydrogels contraints et sur les morphologies induites par les instabilités de la surface libre du gel gonflé, qu'ils soient greffés sur un substrat ou non. Ce chapitre est également consacré à une revue des différentes stratégies disponibles dans la littérature pour réaliser des films de polymères, pour créer un défaut interfacial, mais aussi pour contrôler la densité de greffage du film sur le substrat. L'objectif et le plan de cette thèse sont ensuite exposés.

Introduction

Hydrogels are hydrophilic materials that can absorb and retain up to 95% percent of water. They can be present in nature as in muscles, cartilages, and tissues or as xylenes and phloems in plants.¹⁻³ The first usage of synthetic hydrogel was reported in 1960.⁴ It was a copolymer of 2-hydroxyethyl methacrylate (HEMA) and ethylene dimethacrylate (EDMA) for use as contact lenses.

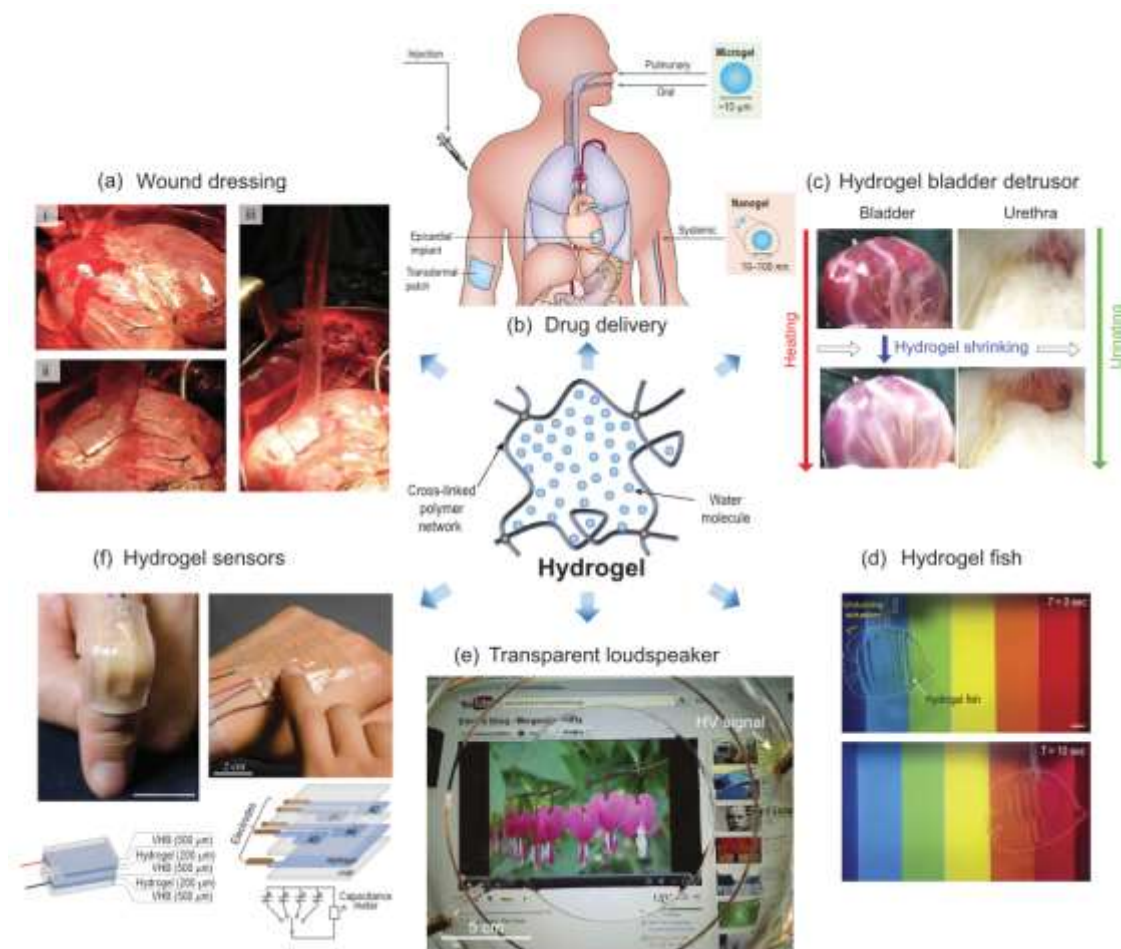


Figure 1: Application of hydrogel in different fields.^{9,13-17} (a) A cut on a pig heart is sealed with a hydrogel by strong adhesion. Adapted from [9]. (b) Hydrogels are used to control drug delivery applications. Redrawn from [13]. (c) A hydrogel bladder detrusor, which can help to shrink an animal bladder. The figure is adapted from [22]. (d) A hydrogel fish which can be camouflaged optically and sonically in water. Adapted from [21]. (e) A new transparent loudspeaker built with dielectric elastomer and ionically conductive hydrogel. Adapted from [20]. (f) Hydrogel sensors for testing under stretch and compression. Adapted from [19].

Hydrogels generally consist of highly swollen cross-linked polymer networks which can be tuned to have different topologies and chemical compositions, thus making them adaptable to various applications.⁵ The hydrogel can dissolve and transport different ions and molecules, which makes them suitable, as an example, for drug delivery applications.^{6,7} Due to their outstanding mechanical properties and biocompatibility, they are also widely used in other biomedical applications such as tissue engineering, wound dressing, and contact lenses⁸⁻¹³ as shown in Figure 1 a), b), c).

Hydrogel coatings are also suitable candidates for many applications in engineering fields where properties such as lubrication, hydrophilicity, and transparency are desired as illustrated in figure 1.d), e), f). Indeed, these hydrophilic polymer networks may absorb water by swelling to several times their dry thickness. As such, hydrogel coatings are possibly good candidates for anti-fog applications, as proposed by several teams¹⁸⁻²¹ who discussed their efficiency in terms of light transmission while submitted to warm humid air. Indeed, the coating should act as a reservoir for humidity, and observation is made²⁰⁻²² that the thicker the film, the more water is absorbed, and the later mist appears. However, the viability of such anti-fog coatings is limited by their ability to sustain stresses without damage.

In the present work, we offer to focus on the damaging of thin films due to the debonding from the substrates, in the particular case where debonding is promoted by the swelling of the film by a solvent.

In the following, we first review the literature on the physical properties of thin swellable films. Indeed, past studies have evidenced the interplay between the development of elastic instabilities, the occurrence of delamination, and the constrained swelling of polymers by a solvent. Here, we focus on cases where the swelling is restricted to only one direction because either it is confined sideways or it is a thin film attached to a substrate. We describe the morphologies that were observed in these cases at the surface of swollen polymers and the physical mechanisms underlying their growth. We also report observations showing that patterning the anchoring of thin films onto a substrate can be used to tune these 3D morphologies. This review leads us to show that a quantitative study of the link between grafting, swelling, and the occurrence of delamination of thin swellable films is needed in order to better control the development of polymer coatings.

Hence, we next discuss the literature on the challenges in the synthesis of swellable thin polymer films and the control of their anchoring strength onto substrates. This will allow us to

define the synthesis strategy of our model systems in order to address the question of their ability to resist spontaneous delamination upon swelling.

1 Elastic instabilities induced by the swelling of thin films

Unattached, bulk cross-linked hydrogels can swell isotropically in a stress-free state. Conversely, hydrogel coatings attached to rigid substrates experience compressive stresses during swelling as the film is allowed to swell only in the direction normal to the surface as a result of the lateral constraints induced by the bonding of the film to the substrate.²³ This unidirectional swelling thus gives rise to equi-biaxial compressive stresses, which can be quite large, even exceeding the elastic modulus of the gel.

1.1 Surface-attached hydrogel films

For hydrogel films strongly anchored to the substrate, these swelling stresses are observed to induce a variety of mechanical instabilities on the free surface, such as cusp-like creases or rounded wrinkles, which locally relieve compressive stress^{23–25} with a characteristic spacing between folds proportional (and nearly equal) to the thickness of the gel layer. This instability has important implications for the design of biomaterials, smart surfaces, and sensors since it places a fundamental limit on the amount of swelling that a surface-attached polymer layer may undergo without forming topographical features.

A theoretical understanding of this creasing instability was provided in the 1960s by Biot, who made the simple prediction that a semi-infinite incompressible rubber-like elastic solid will become linearly unstable to a surface-buckling mode at a critical value of the compressive strain, which does not depend on the modulus of the material or the characteristic length-scale of the instability.²⁶ Specifically, he found that the instability should first occur under equi-biaxial compression when the extension ratio reaches a critical value which does not depend on the modulus of the material or the characteristic length-scale of the instability.

Using a model system of poly(acrylamide-*co*-sodium acrylate) hydrogels attached to rigid substrates (shown in Figure 2), Trujillo and co-workers observed that the onset of creasing corresponds to an effective linear compressive strain of ~ 0.33 or a change in thickness by a factor of ~ 2 . Remarkably, this value varies only slightly with modulus over a range of ~ 0.6 – 24 kPa and is independent of gel thickness from $3 \mu\text{m}$ – mm , in excellent agreement with the theoretical predictions of Biot.^{23,24,27–29}

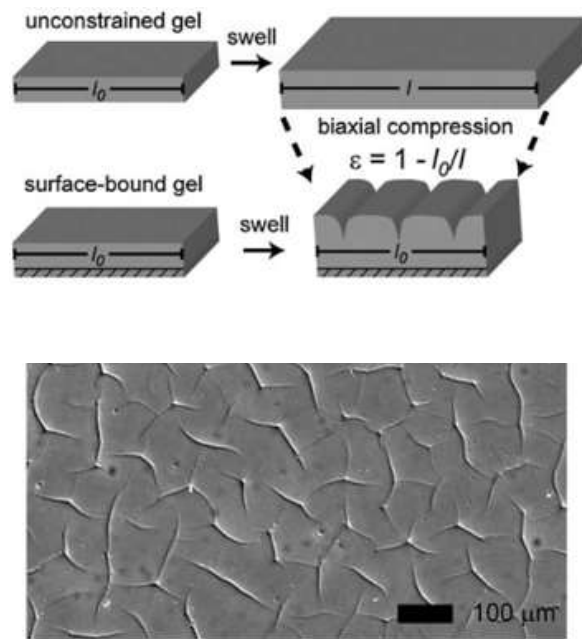


Figure 2 adapted from [23]: Swelling of surface-attached poly(acrylamide-co-sodium acrylate) hydrogels attached to rigid substrates, which gives rise to the compressive stresses which can be partially relieved by localized creasing of the gel.²³

For thicker gel samples, the kinetics of the formation of these patterns has been investigated by Tanaka et al. in the case of ionized polymer acrylamide gels formed in Petri dishes.²⁴ Here, the Petri dish constrains the swelling sideways, as shown in Figure 3.

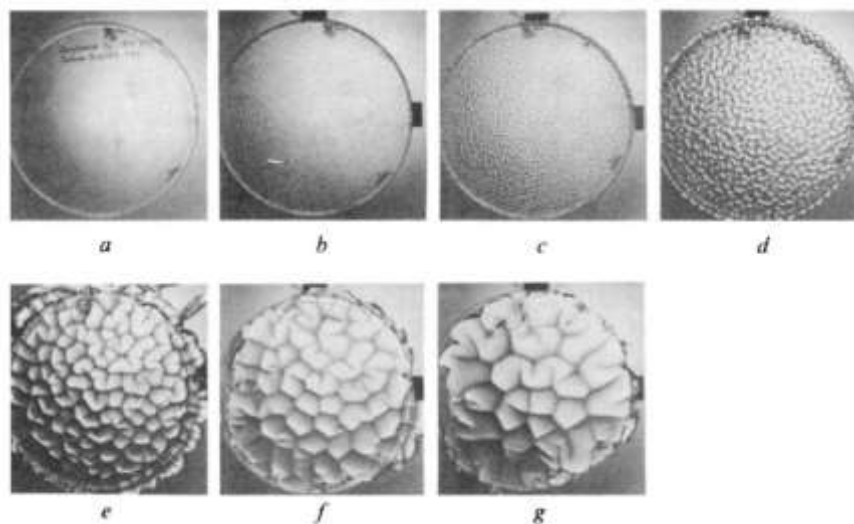


Figure 3 adapted from [24]: Images of an acrylamide gel taken during the course of its swelling within a Petri dish. Patterns form on the gel and exhibit a typical length scale which increases as the swollen thickness increases upon swelling.²⁴

According to the authors, the differential swelling strain that results from the gel's heterogeneous swelling along the vertical direction is what causes this pattern to appear. A very thin surface layer initially swells. This layer is constrained mechanically in that its inner surface is locked to the gel's core while its outer surface is free to expand. As a result, the layer is under conflicting pressure from the above and lower surfaces, with one pressuring it to swell and the other to stay firm. The gel stretches (or expands) unidirectionally perpendicular to the surface in order to balance these conflicting forces when the osmotic pressure is low. When the osmotic pressure is large, the outer surface is forced to buckle. Here, the characteristic wavelength of the pattern is proportional to the thickness of the superficial swollen layer. They increase concomitantly over time.

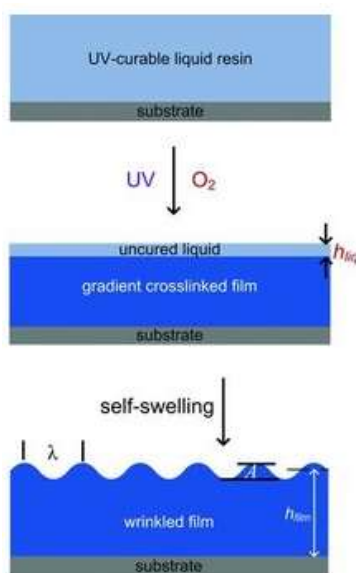


Figure 4 adapted from [30]: Self-wrinkling mechanism for UV-cured polyacrylate in the open air.³⁰

The study conducted by Chandra et al.³⁰ (shown in Figure 4) found that wrinkles can form at the surface of a swelling film when a gradient of cross-linking along its thickness is obtained from the synthesis of the gel. To do so, the polymerization of the chemical reaction was inhibited by oxygen diffusing from the free surface of the sample into the film. Due to oxygen inhibition, a top layer of non-polymerized monomers that is present during UV curing causes the bottom cross-linked film to bulge and wrinkle. By adjusting the resin film thickness, oxygen partial pressure, and photoinitiator concentration, wrinkle wavelength and amplitude can be adjusted. By spatially arranging the oxygen surrounding the curing film, patterned wrinkles are created. Then Lacombe et al.³¹ have qualitatively demonstrated that the film depth-dependent cross-linking gradient caused by oxygen inhibition during irradiation exists. They saw long-range, highly organized surface morphologies like hexagons, peanuts, or lamellae can be

produced through the self-wrinkling of different monomers of acrylates, as shown in Figure 5. The film thickness, which affects both the type of morphology and its characteristic wavelength, and the cross-linker concentration, which controls solely the type of morphology, are the two parameters that can be utilized to easily tune the pattern.

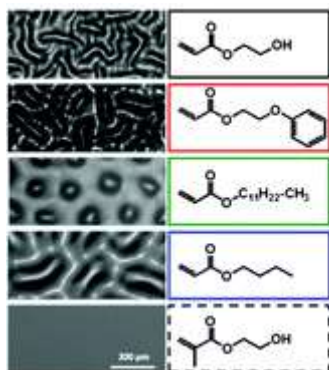


Figure 5 adapted from [31]: Different morphologies present on the surface of the gel for different UV cured meth(acrylate) monomers.³¹

1.2 Swelling instabilities and delamination

1.2.1 Swelling-induced debonding in weakly adhering hydrogel films

In situations where the film is not strongly bound to the substrate, swelling stresses can alternately result in interface delamination followed by large-scale folding and blistering of the hydrogel films. Such mechanisms have been observed by Velankar *et al.*²⁸ for poly(dimethylsiloxane) films swollen with toluene, causing the growth of sharp folds of high aspect ratio. This situation is illustrated in Figure 6.

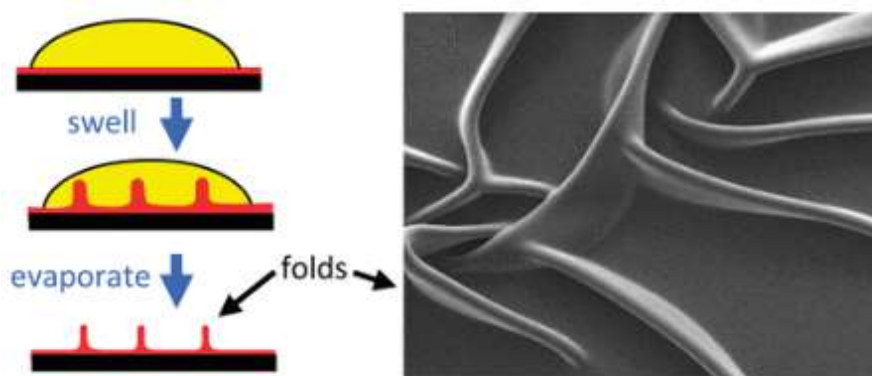


Figure 6 adapted from [28]: The SEM image of folded dried PDMS gel after exposure to toluene.²⁸ Buckle delamination of the film from the surface resulted in the growth of sharp folds, which persist even after the solvent evaporates.

Other morphologies in the form of craters were also reported by Sharp *et al.*³² for water-immersed ultrathin films of poly(d,l-lactide) as a result of a blistering process which occurs when the films delaminate from the silicon substrate. The blisters proceed to grow until they reach a maximum size. At any point during the growth process, the blisters can be made to collapse by removing the films from the water.

1.2.2 Morphogenesis from controlled buckling instabilities using substrate patterning

From a different perspective, controlled debonding and blistering of swollen hydrogel films on patterned substrates was also investigated as a tool to generate switchable actuators for soft robotics or micro/nanofluidic devices.^{34–36} By controlling stimuli-responsive elastic instabilities on selected substrate areas, switchable actuators can be designed. As an example, Xu and coworkers³³ elaborated poly(N-isopropylacrylamide)-co-sodium acrylate) (PNIPAM) gel layer on micro-patterned electrode surfaces, which allowed to trigger electrochemically the reversible delamination and blistering of the hydrogel films as shown in Figure 7.

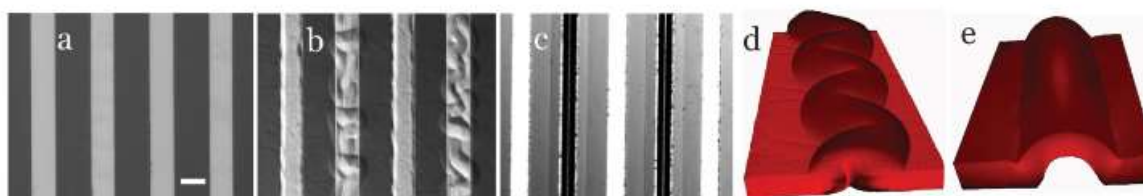


Figure 7 adapted from [36]: Delamination buckling induced by a reversible electrochemical reaction within an anionic PNIPAM copolymer gel supported on silicon substrates micropatterned with gold interdigitated electrodes. a) While the surface is initially flat, increasing the applied potential results in b) delamination and buckling, followed by c) formation of a straight-sided ‘Euler column.’ The scale bar is 50 μm . 3D reconstructed images show d) the first stage in delamination exhibiting a regular ‘telephone cord’ morphology, and e) Euler column.³³

Similarly, Takahashi *et al.* explored in a systematic way the 3D architectures which are generated from the swelling-induced buckling instabilities within acrylamide hydrogel films on patterned silanized substrates.³⁷ Utilizing the chemical modification of the rigid substrate and a conventional photolithography technique, the delamination location is controlled by non-adhesive stripes, resulting in high aspect folding architectures at selected positions. As shown in Figure 8, at an early stage of swelling, rapid buckling, which has a straight-sided blister-like shape, is observed. As the swelling time increased, a telephone-cord-like buckling and architecture growth was observed as a result of combined buckling along the x and y directions.

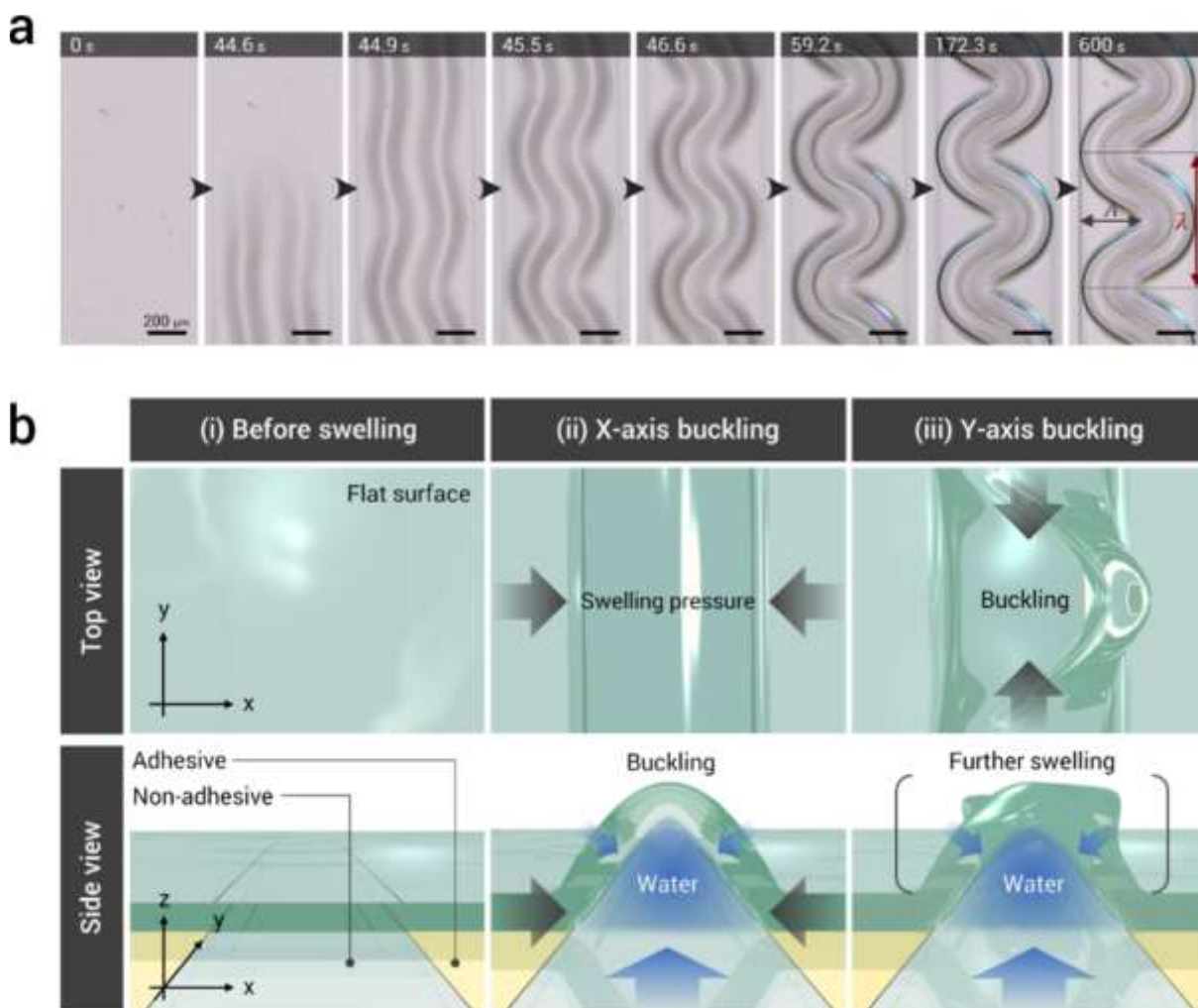


Figure 8 adapted from [37]: Observation of 3D architecture formation within a polyacrylamide gel film on a silicone substrate patterned with areas of low adhesion. (a) Phase-contrast image shots of the 3D architecture during swelling in deionized water. After the appearance of rapid buckling (~ 45 s), telephone-cord buckling and architecture growth are observed (~ 170 s). Finally, the architecture reached an equilibrium state (~ 600 s). (b) Schematic illustration of the mechanism of 3D hydrogel architecture formation. (i) Partially surface-attached flat hydrogel film was fabricated and immersed in deionized water. The telephone-cord buckling architecture was induced by two coupled bucklings: (ii) X-axis buckling and (iii) Y-axis buckling. Water is diffusing through the gel and flowing from open edges.³⁷

Using this approach, Takahashi and co-workers explored in a systematic way the relationship between the morphology of the debonded film and the thickness of the film, the cross-link density, and the associated swelling ratio and geometry of the silanization pattern (Figure 9). From a theoretical point of view, the formation of swelling-induced telephone cord blisters in hydrogel films was addressed by Yuan *et al.*³⁸ within the framework of a large strain theory. Predictions for the morphology parameters of the developed theory were found to agree with

experimental results from Takahashi *et al.*³⁷ and the critical mechanical conditions associated with the material-specific parameters, such as the cross-linking density and swelling ratio are also revealed.

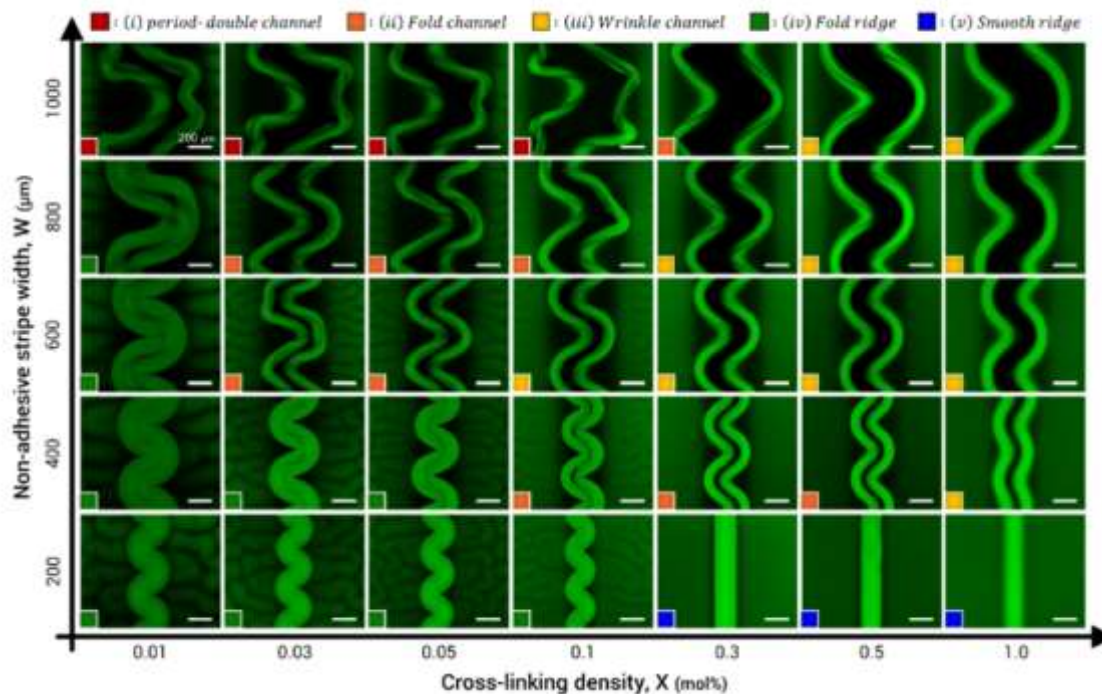


Figure 9 adapted from [37]: 3D Phase diagram of the buckling morphologies achieved within a polyacrylamide hydrogel film on silicon wafer patterned with areas with low adhesion as a function of the cross-link density (i.e., the swelling ratio) and the width of the non-adhesive stripe.³⁷

All the above-mentioned studies evidence the onset of swelling induced internal stresses within gel films, which depend on the swelling of the gel, its thickness, and the degree of constrained swelling. They are focusing on the morphogenesis of 3D patterns within thin hydrogel films from buckling instabilities induced over selectively controlled areas with low adhesion. The propagation of delamination from these buckling instabilities is not considered, the interfacial adhesion outside the non-adhesive pattern being high enough to prevent debonding under the action of swelling stresses.

In the present study, the objective is to investigate the relationship between delamination and interfacial physical chemistry between hydrogel films and a rigid silicon substrate. For this purpose, we propose a methodology where (i) debonding is initiated from well-controlled defects with low adhesion and (ii) the strength of the film/substrate interface outside the patterned areas is tuned by playing with the grafting density. To do this, first, we need to synthesize hydrogel thin films with high swelling ability, which can be grafted on silicon

substrates with varied strength. For this purpose, it is required to (i) find a new strategy to control the grafting between the hydrogel and the substrate and (ii) create well-controlled defects between the hydrogel and substrate interface in order to control the nucleation of the delamination mechanism.

2 Hydrogel coatings

An ideal hydrogel coating should achieve two features. First, good adhesion between the substrate and the hydrogel coating has to be kept in any condition, possibly with environmental change, in air or underwater, which induces the swelling of the hydrogel. Second, the topographical aspect should be as little disturbed as possible by the environmental change. There is then a need to propose a facile and versatile method to develop a platform of hydrogel coatings attached to the substrates with controlled physico-chemical properties such as thickness, swelling, and interface strength.

In the following, we describe the challenges in the synthesis of thin polymer films onto rigid substrates. In a second part, we briefly report on the bibliography available on how to tune the interfacial properties between a polymer film and its substrate. Finally, we discuss the methods from the literature allowing to pattern the substrate.

2.1 Challenges in the synthesis of highly swellable thin polymer films

Thin polymer films can be roughly classified into two categories. On the one hand, there are thin polymer films in which chemistry is well-controlled. In this category, Layer-by-Layer (LbL assemblies) and polymer brushes have been extensively investigated in the last two decades. However, in LbL assemblies, their thickness range is limited since each layer is nanometer-thick, so that micrometric assemblies are only obtained for thousands of cycles. For polymer brushes, the thickness is determined by the chain length. Polymer brushes are then submicrometer-thick. On the other hand, polymer coatings on rigid substrates can be obtained by coating methods such as spin-coating, dip-coating, or spray-coating. There is no limitation on thickness for these polymer coatings. But the control of the chemistry and the macromolecular architecture cannot be achieved. Recently, in our group, we have developed surface-attached hydrogel films which combine both features. Surface-attached hydrogel films have controlled architecture and can be varied over a wide range of thicknesses. In the following, we report briefly the main features of these thin polymer films.

2.1.1 Layer-by-Layer assembly and Polymer brushes

A process of preparing thin films is layer-by-layer (LbL) assembly (Figure 10). The films are created by alternately depositing layers of oppositely charged materials, followed by wash stages. R. K. Iler was the first to use this method, and he was successful in creating multilayers of colloidal nanoparticles in the 1960s.³⁹ After that, Gero Decher revived it in the 1990s by expanding its applicability from particles to a variety of polyelectrolytes (PEs).^{40–43} Nowadays, the layer-by-layer assembly has become a universal approach for the facile fabrication of multicomponent films on solid supports. It is important to note that during the preparation of LbL assemblies, apart from electrostatic attraction, some other interactions are involved in this process, including hydrophobic attraction.⁴⁴ Additionally, for some polyelectrolytes and water-soluble non-ionic polymers, hydrogen bonding can be used to create multilayer films based on LbL assembly^{45–47}. In reality, a wide range of materials, including nanoparticles,^{48,49} colloids,⁵⁰ and biological molecules,⁵¹ can be deposited by LbL in addition to polyelectrolytes to create functionalized conformal nanostructured interfaces.

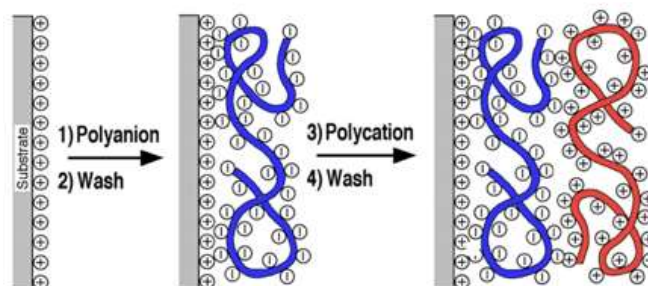


Figure 10 adapted from [40]: Schematics of Layer by Layer process assembling polyanion and polycation couple.⁴⁰

A monolayer of polymer chains that are grafted by one end onto a surface or an interface is referred to as a polymer brush (Figure 11).⁵² The polymer chains must extend away from the surface or interface to avoid overlapping since the grafting density is so great, resulting in a stretched conformation.⁵³ In reality, a combination of strong entropic repulsion between polymer chains, entropic stretching costs, and frozen constraints as a result of irreversible grafting dominates the behavior of polymer brushes.⁵⁴ Generally, there are two ways to prepare polymer brushes: physisorption and covalent attachment, while the covalent attachment can be achieved by either “grafting to” or “grafting from” approaches. The “grafting from” method is preferable because it allows high grafting density and control over the length of polymer chains

and thus the brush thickness, thanks to *in situ* surface-initiated polymerizations, usually surface radical polymerization such as RAFT or ATRP.^{55–57} It was demonstrated, however, that the "grafting to" method enables the production of brushes using different kinds of polymers and on a variety of grafting densities. The "grafting to" technique also benefits from simplicity as it does not involve complex chemistry.⁵⁸

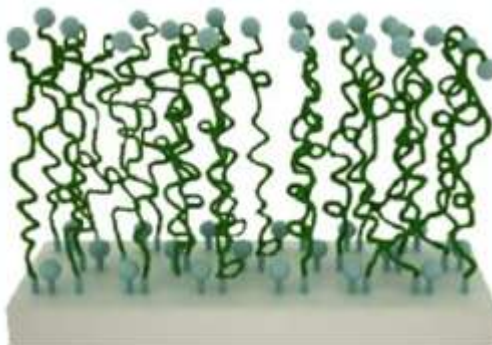


Figure 11 adapted from [59]: Schematics of polymer brushes attached to the substrate.⁵⁹

2.1.2 Hydrogel thin films

Despite their enormous promise, hydrogel thin films are, as far as we know, still hardly studied. We summarize the few studies on the production of hydrogel thin films in the sections that follow. Usually, one of the two techniques listed below is used to create thin films of chemically cross-linked hydrogels:

- i. cross-linking copolymerization by mixing monomers and multifunctional comonomers;
- ii. cross-linking functionalized (co)polymers with reactive groups or with high-energy irradiation.

In the first approach, copolymerization and cross-linking take place simultaneously. Solvent-based free radical polymerization techniques are widely employed. After being contained between two planar substrates (one functionalized to attach the hydrogel film and the other non-sticky to detach the film) and spacers, the reaction mixture consisting of monomers, the cross-linker, and the initiator is then polymerized and cross-linked *in situ*.⁶⁰ The UV-initiated polymerization technique has received the most interest among all free radical polymerization methods because it allows hydrogel sheets to be micropatterned using a projection mask.^{60–63} However, because of the UV beam's volumetric absorption, this method might not be suitable for thick hydrogel films. Due to its beneficial characteristics, such as one-step, solvent-free, and vapor-phase, plasma polymerization is another alluring deposition method utilized to

manufacture strongly cross-linked hydrogel thin films (normal thickness ranging from tens to hundreds of nanometers). In this case, cross-linking occurs naturally as a result of the ion or electron irradiation of the material during deposition; therefore, cross-linkers are not required.⁶⁴⁻⁶⁷ And the polymerization time and plasma power can easily be varied to adjust the dry hydrogel film thickness.

In the second method, functionalized (co)polymers are coated in a thin layer to create hydrogel before polymer chains are cross-linked in the dry state. There have been several coating processes established to date, including spin coating, dip coating, spray coating, etc. these coating techniques allow to vary the film thickness from 0.01 μm to several micrometers. Various cross-linking methods are available depending on the chemical make-up of the polymer. For instance, pH-responsive hydrogel thin films are created by spin-coating thin layers of mixed PVA/PAA chains, drying them, and then thermally cross-linking them at 130°C via an esterification reaction.^{68,69}

While the cross-linking of copolymers with photo-reactive pendant groups or monomers can be accomplished either by the addition of photoinitiators⁷⁰ or by exposure to UV radiation.⁷¹⁻⁷⁶ Because it is compatible with photolithography and enables the creation of hydrogel films with a wide range of dry thicknesses, the cross-linking method based on UV irradiation is widely employed (from nanometres to tens of microns).^{77,78} Actually, random chain scission caused by high-energy radiation, such as an electron beam, γ -rays, or UV light, leads to free radicals that are then recombined to create a cross-linked polymer network.⁶ The ratio of cross-linkers and/or the radiation exposure is said to determine the cross-linking density.

2.1.3 CLAG approach using click chemistry

Recently, our group proposed a facile and versatile approach that enables the development of a platform of surface-attached hydrogel films with well-controlled chemistry. We called this approach CLAG which is the acronym of Cross-link And Grafting. The surface-attached hydrogel thin films are prepared by simultaneously cross-linking and grafting preformed and functionalized polymer chains by click chemistry, as shown in figure 1.^{22,80-83}

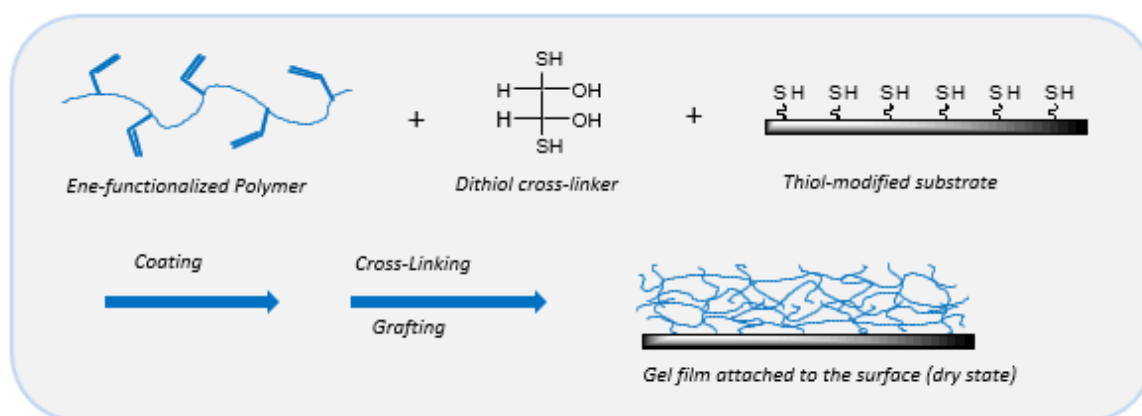


Figure 12 adapted from [79]: Schematic of ene-functionalized polymer is mixed with dithiol cross-linker and spin-coated on a thiol modified substrate to form a well-controlled film.⁷⁹

The click chemistry we chose is the thiol-ene reaction⁸⁴ as it can be activated by heating (at temperatures below the temperature of polymer degradation) or by UV irradiation (at 250 nm without the need of a photoinitiator). Moreover, numerous thiol chemicals are easily available for grafting onto substrates and for the chemical cross-linking between functionalized chains. For example, mercaptosilanes are used for grafting onto oxide layers (silicon and glass substrates, silica, titanium oxide...). Dithiol cross-linkers with specific spacers are chosen to adapt to the polymers. Dithiol cross-linkers can also react with each other to form stable disulfide bridges of flexible lengths, which promote the connection between polymer chains for the formation of the chemical network.

The key aspect of the CLAG approach is that it starts with preformed polymer chains. As radical polymerization is highly sensitive to oxygen, it is very difficult to well control the synthesis of polymer networks on the surface if the process starts with coated monomers. Ene-functionalized polymer chains are first synthesized by the free radical polymerization method. This is also one of the great advantages of the CLAG approach, as free radical polymerization is a straightforward method which allows low and high polymer molecular weight in contrary to controlled radical polymerization. And here, there is no need for narrow distribution of polymer chains as they are dedicated to being cross-linked. This enables us to generalize the CLAG approach to various hydrogels made with acrylate- and acrylamide- polymers.

Various ene-functionalized polymers have been synthesized by free radical polymerization. Among them, a few examples are shown in

Figure 13. Poly(dimethylacrylamide) PDMA hydrogel films have been investigated for anti-mist properties.²² Poly(acrylic acid) PAA hydrogels were shown to be a good platform for aptamers grafting in the design of biosensors.⁸⁵ The temperature-responsive properties of poly(*N*-isopropylacrylamide) PNIPAM hydrogels, which show Lower Critical Solution Temperature (LCST) behavior, were investigated^{79,82,86}. Poly[poly(ethylene glycol) methyl ether methacrylate] poly(PEGMA) can also have LCST properties with adjustable temperature transition depending on the length of the PEG side chains.⁸⁷ The ene-functionalized polymers synthesized can be then purified and recovered (by freeze-drying or precipitation) to be characterized. In particular, the ratio of ene-functionalization, which can be determined by NMR spectroscopy, will rule the cross-linking ratio and then the swelling of the hydrogel layer.

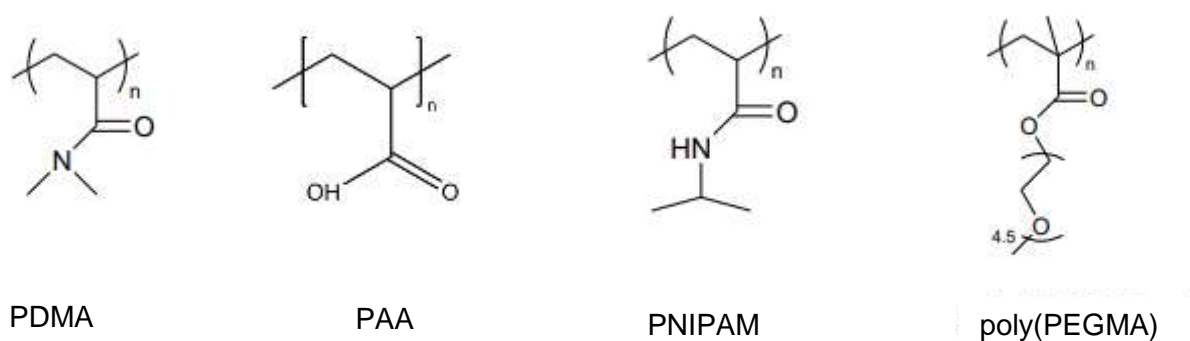


Figure 13: Generalization of CLAG strategy to various polymers such as poly(dimethylacrylamide) PDMA, poly(acrylic acid) PAA, poly(*N*-isopropylacrylamide) PNIPAM, poly[poly(ethylene glycol) methyl ether methacrylate] poly(PEGMA).

The ene-functionalized polymers are then solubilized in a proper solvent with suitable dithiol cross-linkers before being coated on the thiol-modified substrates. Different coating methods can be used, such as spray-coating, spin-coating, and dip-coating, depending on the thickness range desired. Spin-coating is often used because it requires little polymer, and it allows the formation of polymer films widely ranging from a few nanometers to several micrometers, which is well suited to our studies. After the spin-coating of polymer films on the treated substrates, the cross-linking and surface-grafting of polymer chains are achieved by activating the thiol-ene click reaction either by heating to obtain hydrogel films or by UV irradiation to obtain hydrogel patterns. It means that the synthesis of surface-attached hydrogels is performed in a dry state without solvent (melting polymer condition).

When swelling in water, the surface-attached hydrogel film can undergo mechanical stresses, resulting in the formation of instabilities such as wrinkles at the surface of the hydrogel layer. This depends strongly on the thickness and the swelling ratio of the hydrogel. In situations where the film is not strongly bound to the substrate, swelling stresses can result in interface delamination followed by large-scale folding and blistering of the hydrogel films. This depends on the interface strength between the hydrogel and the substrate. This interface strength ruled by the grafting density of the hydrogel to the surface can be controlled by the reaction of the ene-functions to thiol monolayer, which is the subject of the next part.

2.2 Tuning the interfacial strength at the polymer/substrate interface

The control of the interface strength is a key point of our studies. As explained in the previous part, the interface strength is ruled by the grafting density of the hydrogel to the surface. It can be controlled by the silanization of reactive species on the substrate. In the following, we report briefly the main silanization techniques described in the literature. We also review some photolithography techniques used to fabricate controlled micro-patterns. We describe in detail only two processes that are the closest to the strategy we will adapt to create line defects by micro-patterning using a photolithography-like technique.

2.2.1 Silanization

The high adhesion between the hydrogel coating and the oxide layer of substrates is achieved by using a common bridge molecule silanization.⁸⁸ Alkoxysilanes help to improve adhesion and modify the substrate.⁸⁹ These silanes should be selected, which can minimize hydrolysis and other by-products during silanization. To avoid this, silanization is done in a nitrogen-plugged reactor. This can avoid any reaction to oxygen with silanes. As schematically depicted in Figure 14, the alkoxy group at the end of the silane can hydrolyze to form a silanol group in the aqueous environment and condense with the hydroxyl group on the target surface to form siloxane bonds, enabling strong bonds between the substrate and the hydrogel group.^{7,89,90} The other end of the silane should have the active group which can react with the polymer.

A mixed layer of silane can be obtained by codeposition^{100,103} or by stepwise deposition.^{101,102} In co-deposition, both the silanes are deposited together in a defined concentration^{91,104}, as shown in Figure 15. a. The stepwise technique is suitable for silanes which react to each other. First is preferred when silanes may react to each other. Then this partially functionalized substrate is exposed to the second silane to have the desired mixture of silanes.⁹⁹ This is illustrated in Figure 15(b) and Figure 16.

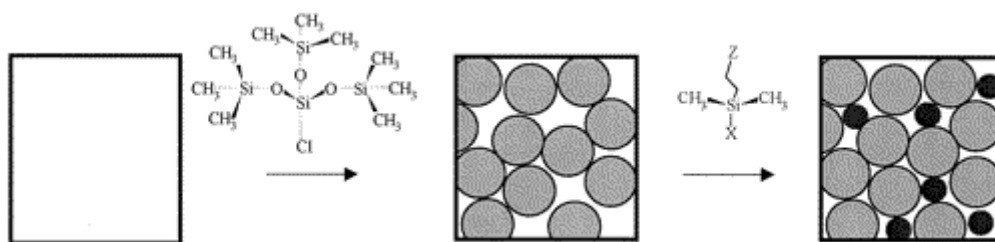


Figure 16 adapted from [101]: The two-step silanization procedure.¹⁰¹

In the literature, surface modifications by mixed monolayers of silanes have been used to control the wetting properties of liquid droplets on modified substrates.¹⁰⁴ It has also been used to develop a DNA microarray on a substrate whose grafting density is varied by mixing silanes.⁹⁷ Until now, there has been no study done to vary the grafting density by mixing different silanes on a substrate that is used for grafting thin hydrogel film on the substrate with varied interfacial strength.

2.3 Patterning of the substrate to control the nucleation of delamination

In the present work, we offer to nucleate delamination of thin swellable film from a well-defined spot. To do this, we need to create a pattern with low interfacial strength. In the following, we review the techniques used in the past to pattern substrate. Indeed, the interest in patterning at micro and sub-micrometer scales has been increasing in recent years with the advancement in tissue engineering and microfluidics.¹⁰⁵

2.3.1 Photoresist

Over the last two decades, patterned thin films and structured polymeric systems have been identified for optics, medicine, biotechnology, and energy harvesting.¹⁰⁷ Photolithography is a facile process to pattern a substrate. This process only requires high-intensity light and a photomask to produce different patterns on a silicon wafer.^{108,109} Each substrate is coated with a photoresist which may or may not dissolve when exposed to UV light. This patterned

photoresist can act as a guide to chemically etch the actual substrate. Then the remaining photoresist is removed to get the well-patterned substrate.¹¹⁰ There are two types of photoresists: positive and negative photoresists. A positive photoresist is made with polymers which are insoluble, but when exposed to UV light, it degrades into a soluble polymer. A negative photoresist is composed of either monomers or polymers, which can polymerize or cross-link when exposed to UV light to form insoluble polymers, as shown in Figure 17.

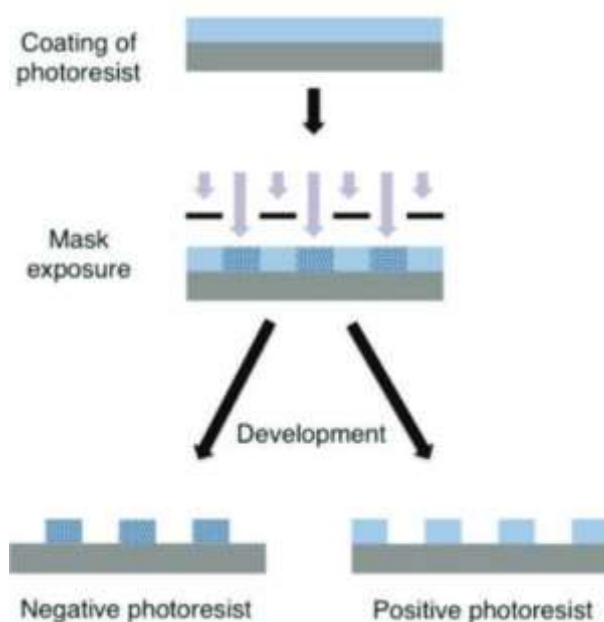


Figure 17 is adapted from [106]: Schematic illustration of mask lithography process.¹⁰⁶

2.3.2 Examples of patterned substrates were used together with hydrogel coatings.

Xu et al.³³ have made a patterned substrate, as shown in Figure 18, by fabricating an electrode on the cleaned silicon wafer by standard photolithographic patterning, e-beam evaporation, and lift-off in acetone. The silicon substrate is micropatterned with gold interdigitated electrodes (IDE) with a width w is $60\ \mu\text{m}$, spaced by an edge-to-edge distance which varied from $90\ \mu\text{m}$ to $120\ \mu\text{m}$, and the initial thickness of the gel is $25\ \mu\text{m}$. The polymer used in this experiment is anionic PNIPAM copolymer gel. The adhesion of gel to the substrate not covered by electrodes is achieved by the silane coating. This thiol monolayer creates an electrochemically switchable link between the gel and the gold microelectrodes. Thermo-responsive PNIPAM deswell with the increment in temperature, which is wisely used to modulate the compressive mismatch in the surface attached gel. This compressive stress creates delamination.

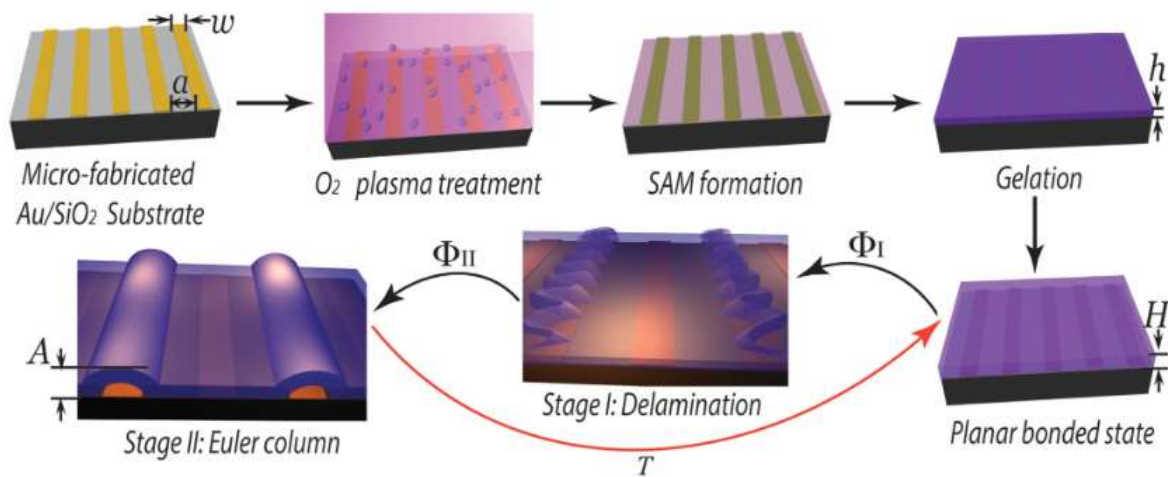


Figure 18 adapted from [33]: Fabrication of gel-based film on an interdigitated electrode array.³³

The patterned substrate in Figure 19 is the study done by Takahashi et al., where the patterned substrate is created by plasma etching of a selected part of the silane monolayer. The substrate is first immersed in a 3-(trimethoxysilyl)propyl methacrylate (TMSPMA) solution for 2 hours for silanization. The substrate is then cleaned in ethanol and dried using nitrogen. In order to create a pattern on the surface of the substrate, a photoresist was spin-coated on a substrate. And it is exposed to a patterned UV and developed. A 30 s plasma etching was done by introducing the sample to a plasma etcher, during which the TMSPMA that was not protected by the photoresist layer was removed. The rest of the photoresist was removed by soaking the substrate for 1 minute in acetone and then dried using nitrogen.

As we are studying the interface between the substrate and hydrogel, we cannot compromise in dealing with any new coating like photoresist and etching on the surface of the substrate, which could create grafting heterogeneities and defects that could compromise the polymer deposit by spin coating. So it is required to make a new photolithographic method that can be suitable for thiol substrate, which has minimum exposure to other materials.

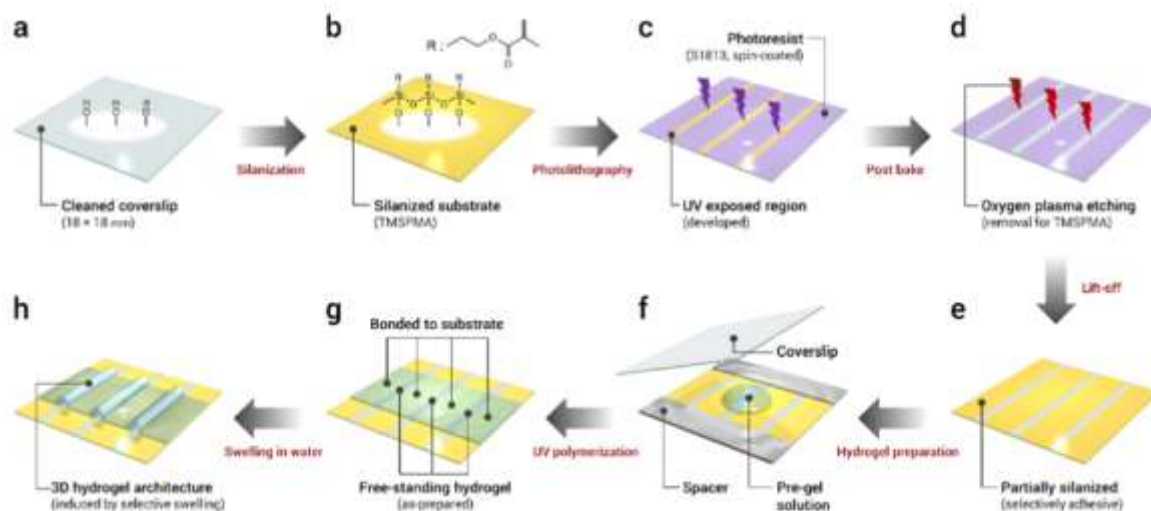


Figure 19 adapted from [37]: A schematic image showing the steps involved to create a 3D hydrogel architecture.³⁷

3 Objectives of the dissertation

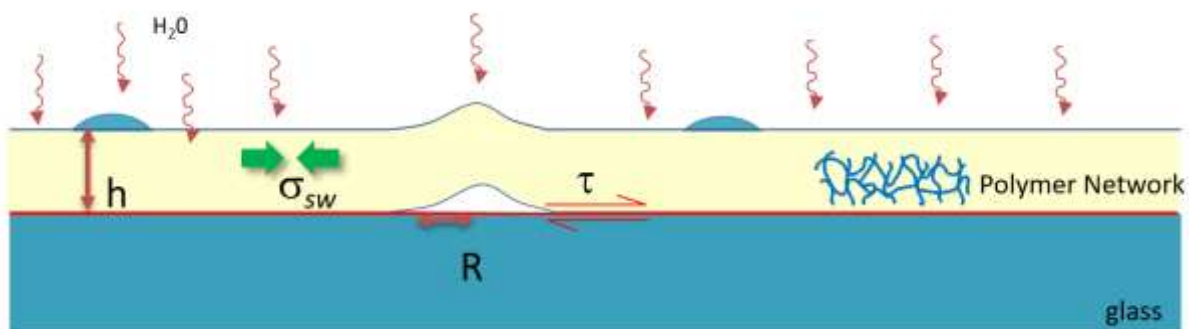


Figure 20: Schematic description of a hydrogel film attached to the substrate, which is delaminating from the interface due to the compressive swelling stresses and forms a blister.

The development of hydrogel films as the coating is conditioned by better control of their durability. To do so, we need to understand the factors affecting the delamination of the coating from the substrate.

When a hydrogel is grafted to the substrate, it undergoes constrained compressive stresses, which sometimes are observed to result in the buckling of its free surface. Different studies have shown that this compressive stress is also enough to delaminate thin films from the substrate. However, those studies focused on the delaminated areas from a morphogenic point of view. In this study, instead of focusing on morphogenesis, we offer to link the grafting

density of hydrogel thin films to the interfacial strength involved in the debonding of these films when it is induced by swelling stresses and to address the following open questions:

- What are the mechanisms driving the debonding? What are the length scales involved?
- Do the 3D morphologies due to the elastic buckling of the swollen films play a role in these debonding mechanisms?
- How can we quantitatively evaluate the resistance to debonding of a grafted film in relation to both the grafting density and the parameters controlling the swelling stresses (solvent, network properties, film thickness)?

To do so, we use well-controlled delamination experiments performed on hydrogel thin films of varied thickness and interfacial strength, with controlled defects on which delamination starts. To this end, we will use the CLAG method with thiol-ene click chemistry to prepare the samples. In the following of the manuscript, we will first describe the hydrogel film synthesis with a focus on three objectives: (i) homogeneity of the hydrogel film across the whole sample (both in thickness and cross-link density), (ii) the control of the chemical grafting density out of the defects, (iii) the patterning of controlled grafting defects on the substrate. The strategy, protocol, and results are described in Chapter 2.

We will then perform debonding experiments from these films on a homemade set-up. The results are described in Chapter 3. These results will be used to determine the relationship between the onset of delamination and the chemistry at the interface between the hydrogel and the substrate. As controlled parameters, we will change the thickness of the film, the width of the defect, and the grafting density. The results will be used to develop a model to understand the mechanisms controlling the onset of delamination.

4 References

- (1) Bai, R.; Chen, B.; Yang, J.; Suo, Z. Tearing a Hydrogel of Complex Rheology. *Journal of the Mechanics and Physics of Solids* **2019**, 125, 749–761. <https://doi.org/10.1016/j.jmps.2019.01.017>.
- (2) Mow, V. C.; Kuei, S. C.; Lai, W. M.; Armstrong, C. G. Biphasic Creep and Stress Relaxation of Articular Cartilage in Compression: Theory and Experiments. *Journal of Biomechanical Engineering* **1980**, 102 (1), 73–84. <https://doi.org/10.1115/1.3138202>.

- (3) Zwieniecki, M. A.; Melcher, P. J.; Michele Holbrook, N. M. Hydrogel Control of Xylem Hydraulic Resistance in Plants. *Science* **2001**, 291 (5506), 1059–1062. <https://doi.org/10.1126/science.1057175>.
- (4) Wichterle, O.; Lím, D. Hydrophilic Gels for Biological Use. *Nature* **1960**, 185 (4706), 117–118. <https://doi.org/10.1038/185117a0>.
- (5) Caló, E.; Khutoryanskiy, V. V. Biomedical Applications of Hydrogels: A Review of Patents and Commercial Products. *European Polymer Journal* **2015**, 65, 252–267. <https://doi.org/10.1016/j.eurpolymj.2014.11.024>.
- (6) Tokarev, I.; Minko, S. Stimuli-Responsive Hydrogel Thin Films. *Soft Matter* **2009**, 5 (3), 511–524. <https://doi.org/10.1039/B813827C>.
- (7) Liu, J.; Qu, S.; Suo, Z.; Yang, W. Functional Hydrogel Coatings. *National Science Review* **2021**, 8 (2), nwaa254. <https://doi.org/10.1093/nsr/nwaa254>.
- (8) Lee, K. Y.; Mooney, D. J. Hydrogels for Tissue Engineering. *Chem. Rev.* **2001**, 101 (7), 1869–1880. <https://doi.org/10.1021/cr000108x>.
- (9) Li, J.; Celiz, A. D.; Yang, J.; Yang, Q.; Wamala, I.; Whyte, W.; Seo, B. R.; Vasilyev, N. V.; Vlassak, J. J.; Suo, Z.; Mooney, D. J. Tough Adhesives for Diverse Wet Surfaces. *Science* **2017**, 357 (6349), 378–381. <https://doi.org/10.1126/science.aah6362>.
- (10) Boateng, J. S.; Matthews, K. H.; Stevens, H. N. E.; Eccleston, G. M. Wound Healing Dressings and Drug Delivery Systems: A Review. *Journal of Pharmaceutical Sciences* **2008**, 97 (8), 2892–2923. <https://doi.org/10.1002/jps.21210>.
- (11) Fram, D. B.; Aretz, T.; Azrin, M. A.; Mitchel, J. F.; Samady, H.; Gillam, L. D.; Sahatjian, R.; Waters, D.; McKay, R. G. Localized Intramural Drug Delivery during Balloon Angioplasty Using Hydrogel-Coated Balloons and Pressure-Augmented Diffusion. *Journal of the American College of Cardiology* **1994**, 23 (7), 1570–1577. [https://doi.org/10.1016/0735-1097\(94\)90658-0](https://doi.org/10.1016/0735-1097(94)90658-0).
- (12) Kopecek, J. Hydrogels: From Soft Contact Lenses and Implants to Self-Assembled Nanomaterials. *Journal of Polymer Science Part A: Polymer Chemistry* **2009**, 47 (22), 5929–5946. <https://doi.org/10.1002/pola.23607>.
- (13) Li, J.; Mooney, D. J. Designing Hydrogels for Controlled Drug Delivery. *Nat Rev Mater* **2016**, 1 (12), 1–17. <https://doi.org/10.1038/natrevmats.2016.71>.

- (14) Sun, J.-Y.; Keplinger, C.; Whitesides, G. M.; Suo, Z. Ionic Skin. *Advanced Materials* **2014**, 26 (45), 7608–7614. <https://doi.org/10.1002/adma.201403441>.
- (15) Keplinger, C.; Sun, J.-Y.; Foo, C. C.; Rothmund, P.; Whitesides, G. M.; Suo, Z. Stretchable, Transparent, Ionic Conductors. *Science* **2013**, 341 (6149), 984–987. <https://doi.org/10.1126/science.1240228>.
- (16) Yuk, H.; Lin, S.; Ma, C.; Takaffoli, M.; Fang, N. X.; Zhao, X. Hydraulic Hydrogel Actuators and Robots Optically and Sonically Camouflaged in Water. *Nat Commun* **2017**, 8 (1), 14230. <https://doi.org/10.1038/ncomms14230>.
- (17) Yang, X.; An, C.; Liu, S.; Cheng, T.; Bunpetch, V.; Liu, Y.; Dong, S.; Li, S.; Zou, X.; Li, T.; Ouyang, H.; Wu, Z.; Yang, W. Soft Artificial Bladder Detrusor. *Advanced Healthcare Materials* **2018**, 7 (6), 1701014. <https://doi.org/10.1002/adhm.201701014>.
- (18) Grube, S.; Siegmann, K.; Hirayama, M. A Moisture-Absorbing and Abrasion-Resistant Transparent Coating on Polystyrene. *J Coat Technol Res* **2015**, 12 (4), 669–680. <https://doi.org/10.1007/s11998-015-9678-z>.
- (19) Chevallier, P.; Turgeon, S.; Sarra-Bournet, C.; Turcotte, R.; Laroche, G. Characterization of Multilayer Anti-Fog Coatings. *ACS Appl. Mater. Interfaces* **2011**, 3 (3), 750–758. <https://doi.org/10.1021/am1010964>.
- (20) Shibraen, M. H. M. A.; Yagoub, H.; Zhang, X.; Xu, J.; Yang, S. Anti-Fogging and Anti-Frosting Behaviors of Layer-by-Layer Assembled Cellulose Derivative Thin Film. *Applied Surface Science* **2016**, C (370), 1–5. <https://doi.org/10.1016/j.apsusc.2016.02.060>.
- (21) Park, S.; Park, S.; Jang, D. H.; Lee, H. S.; Park, C. H. Anti-Fogging Behavior of Water-Absorbing Polymer Films Derived from Isosorbide-Based Epoxy Resin. *Materials Letters* **2016**, C (180), 81–84. <https://doi.org/10.1016/j.matlet.2016.05.114>.
- (22) Delavoipière, J.; Heurtefeu, B.; Teisseire, J.; Chateauminois, A.; Tran, Y.; Fermigier, M.; Verneuil, E. Swelling Dynamics of Surface-Attached Hydrogel Thin Films in Vapor Flows. *Langmuir* **2018**, 34 (50), 15238–15244. <https://doi.org/10.1021/acs.langmuir.8b03206>.
- (23) Trujillo, V.; Kim, J.; Hayward, R. C. Creasing Instability of Surface-Attached Hydrogels. *Soft Matter* **2008**, 4 (3), 564–569. <https://doi.org/10.1039/B713263H>.

- (24) Tanaka, T.; Sun, S.-T.; Hirokawa, Y.; Katayama, S.; Kucera, J.; Hirose, Y.; Amiya, T. Mechanical Instability of Gels at the Phase Transition. *Nature* **1987**, 325 (6107), 796–798. <https://doi.org/10.1038/325796a0>.
- (25) Mora, T.; Boudaoud, A. Buckling of Swelling Gels. *European Physical Journal E: Soft matter and biological physics* **2006**, 20, 119. <https://doi.org/10.1140/epje/i2005-10124-5>.
- (26) BIOT, M. A. Surface Instability of Rubber in Compression. *Appl. sci. Res.* **1963**, 12 (2), 168–182. <https://doi.org/10.1007/BF03184638>.
- (27) Dervaux, J.; Amar, M. B. Mechanical Instabilities of Gels. *Annual Review of Condensed Matter Physics* **2012**, 3 (1), 311–332. <https://doi.org/10.1146/annurev-conmatphys-062910-140436>.
- (28) Velankar, S. S.; Lai, V.; Vaia, R. A. Swelling-Induced Delamination Causes Folding of Surface-Tethered Polymer Gels. *ACS Appl. Mater. Interfaces* **2012**, 4 (1), 24–29. <https://doi.org/10.1021/am201428m>.
- (29) Southern, E.; Thomas, A. G. Effect of Constraints on the Equilibrium Swelling of Rubber Vulcanizates. *Journal of Polymer Science Part A: General Papers* **1965**, 3 (2), 641–646. <https://doi.org/10.1002/pol.1965.100030220>.
- (30) Chandra, D.; Crosby, A. J. Self-Wrinkling of UV-Cured Polymer Films. *Advanced Materials* **2011**, 23 (30), 3441–3445. <https://doi.org/10.1002/adma.201101366>.
- (31) Lacombe, J.; Soulié-Ziakovic, C. Controlling Self-Patterning of Acrylate Films by Photopolymerization. *Polym. Chem.* **2017**, 8 (7), 1129–1137. <https://doi.org/10.1039/C6PY02072K>.
- (32) Sharp, J. S.; Jones, R. A. L. Swelling-Induced Morphology in Ultrathin Supported Films of Poly(d,L-lactide). *Phys. Rev. E* **2002**, 66 (1), 011801. <https://doi.org/10.1103/PhysRevE.66.011801>.
- (33) Xu, B. B.; Liu, Q.; Suo, Z.; Hayward, R. C. Reversible Electrochemically Triggered Delamination Blistering of Hydrogel Films on Micropatterned Electrodes. *Adv. Funct. Mater.* **2016**, 26 (19), 3218–3225. <https://doi.org/10.1002/adfm.201504769>.

- (34) Slaughter, B. V.; Khurshid, S. S.; Fisher, O. Z.; Khademhosseini, A.; Peppas, N. A. Hydrogels in Regenerative Medicine. *Adv Mater* **2009**, 21 (0), 3307–3329. <https://doi.org/10.1002/adma.200802106>.
- (35) Lee, K. Y.; Mooney, D. J. Alginate: Properties and Biomedical Applications. *Progress in Polymer Science* **2012**, 37 (1), 106–126. <https://doi.org/10.1016/j.progpolymsci.2011.06.003>.
- (36) Ilami, M.; Bagheri, H.; Ahmed, R.; Skowronek, E. O.; Marvi, H. Materials, Actuators, and Sensors for Soft Bioinspired Robots. *Advanced Materials* **2021**, 33 (19), 2003139. <https://doi.org/10.1002/adma.202003139>.
- (37) Takahashi, R.; Miyazako, H.; Tanaka, A.; Ueno, Y. Dynamic Creation of 3D Hydrogel Architectures via Selective Swelling Programmed by Interfacial Bonding. *ACS Appl. Mater. Interfaces* **2019**, 11 (31), 28267–28277. <https://doi.org/10.1021/acsami.9b05552>.
- (38) Yuan, B.; Harvey, C. M.; Shen, K.; Thomson, R.; Critchlow, G.; Rickerby, D.; Yu, S.; Wang, S. Swelling-Induced Telephone Cord Blisters in Hydrogel Films. *Composite Structures* **2022**, 280, 114909. <https://doi.org/10.1016/j.compstruct.2021.114909>.
- (39) Iler, R. K. Multilayers of Colloidal Particles. *Journal of Colloid and Interface Science* **1966**, 21 (6), 569–594. [https://doi.org/10.1016/0095-8522\(66\)90018-3](https://doi.org/10.1016/0095-8522(66)90018-3).
- (40) Decher, G. Fuzzy Nanoassemblies: Toward Layered Polymeric Multicomposites. *Science* **1997**, 277 (5330), 1232–1237. <https://doi.org/10.1126/science.277.5330.1232>.
- (41) Decher, G.; Hong, J.-D. Buildup of Ultrathin Multilayer Films by a Self-Assembly Process, I Consecutive Adsorption of Anionic and Cationic Bipolar Amphiphiles on Charged Surfaces. *Makromolekulare Chemie. Macromolecular Symposia* **1991**, 46 (1), 321–327. <https://doi.org/10.1002/masy.19910460145>.
- (42) Decher, G.; Hong, J. D. Buildup of Ultrathin Multilayer Films by a Self-Assembly Process: II. Consecutive Adsorption of Anionic and Cationic Bipolar Amphiphiles and Polyelectrolytes on Charged Surfaces. *Berichte der Bunsengesellschaft für physikalische Chemie* **1991**, 95 (11), 1430–1434. <https://doi.org/10.1002/bbpc.19910951122>.
- (43) Decher, G.; Hong, J. D.; Schmitt, J. Buildup of Ultrathin Multilayer Films by a Self-Assembly Process: III. Consecutively Alternating Adsorption of Anionic and Cationic Polyelectrolytes on Charged Surfaces, 1992.

- (44) Kotov, N. A. Layer-by-Layer Self-Assembly: The Contribution of Hydrophobic Interactions. *Nanostructured Materials* **1999**, 12 (5), 789–796. [https://doi.org/10.1016/S0965-9773\(99\)00237-8](https://doi.org/10.1016/S0965-9773(99)00237-8).
- (45) Kharlampieva, E.; Kozlovskaya, V.; Tyutina, J.; Sukhishvili, S. A. Hydrogen-Bonded Multilayers of Thermoresponsive Polymers. *Macromolecules* **2005**, 38 (25), 10523–10531. <https://doi.org/10.1021/ma0516891>.
- (46) Quinn, J. F.; Johnston, A. P. R.; Such, G. K.; Zelikin, A. N.; Caruso, F. Next Generation, Sequentially Assembled Ultrathin Films: Beyond Electrostatics. *Chem. Soc. Rev.* **2007**, 36 (5), 707–718. <https://doi.org/10.1039/B610778H>.
- (47) Quinn, J. F.; Caruso, F. Facile Tailoring of Film Morphology and Release Properties Using Layer-by-Layer Assembly of Thermoresponsive Materials. *Langmuir* **2004**, 20 (1), 20–22. <https://doi.org/10.1021/la0360310>.
- (48) Merindol, R.; Diabang, S.; Mujica, R.; Le Houerou, V.; Roland, T.; Gauthier, C.; Decher, G.; Felix, O. Assembly of Anisotropic Nanocellulose Films Stronger than the Original Tree. *ACS Nano* **2020**, 14 (12), 16525–16534. <https://doi.org/10.1021/acsnano.0c01372>.
- (49) Hu, H.; Pauly, M.; Felix, O.; Decher, G. Spray-Assisted Alignment of Layer-by-Layer Assembled Silver Nanowires: A General Approach for the Preparation of Highly Anisotropic Nano-Composite Films. *Nanoscale* **2017**, 9 (3), 1307–1314. <https://doi.org/10.1039/C6NR08045F>.
- (50) Sukhorukov, G. B.; Donath, E.; Lichtenfeld, H.; Knippel, E.; Knippel, M.; Budde, A.; Möhwald, H. Layer-by-Layer Self Assembly of Polyelectrolytes on Colloidal Particles. *Colloids and Surfaces A: Physicochemical and Engineering Aspects* **1998**, 137 (1), 253–266. [https://doi.org/10.1016/S0927-7757\(98\)00213-1](https://doi.org/10.1016/S0927-7757(98)00213-1).
- (51) Wilson, R.; Mehrabi, M.; Prior, I. A.; Beckett, A.; Hutchinson, A. A Reliable Method for Attaching Biological Molecules to Layer-by-Layer Self-Assemblies. *Chem. Commun.* **2009**, No. 18, 2487–2489. <https://doi.org/10.1039/B822688A>.
- (52) Advincula, R. C.; Brittain, W. J.; Caster, K. C.; R uhe, J. POLYMER BRUSHES; 2004.
- (53) Zhao, B.; Brittain, W. J. Polymer Brushes: Surface-Immobilized Macromolecules. *Progress in Polymer Science* **2000**, 25 (5), 677–710. [https://doi.org/10.1016/S0079-6700\(00\)00012-5](https://doi.org/10.1016/S0079-6700(00)00012-5).

- (54) Stuart, M. A. C.; Huck, W. T. S.; Genzer, J.; Müller, M.; Ober, C.; Stamm, M.; Sukhorukov, G. B.; Szleifer, I.; Tsukruk, V. V.; Urban, M.; Winnik, F.; Zauscher, S.; Luzinov, I.; Minko, S. Emerging Applications of Stimuli-Responsive Polymer Materials. *Nature Mater* **2010**, 9 (2), 101–113. <https://doi.org/10.1038/nmat2614>.
- (55) Sanjuan, S.; Tran, Y. Synthesis of Random Polyampholyte Brushes by Atom Transfer Radical Polymerization. *Journal of Polymer Science Part A: Polymer Chemistry* **2008**, 46 (13), 4305–4319. <https://doi.org/10.1002/pola.22726>.
- (56) Sanjuan, S.; Tran, Y. Stimuli-Responsive Interfaces Using Random Polyampholyte Brushes. *Macromolecules* **2008**, 41 (22), 8721–8728. <https://doi.org/10.1021/ma8018798>.
- (57) Sanjuan, S.; Perrin, P.; Pantoustier, N.; Tran, Y. Synthesis and Swelling Behavior of PH-Responsive Polybase Brushes. *Langmuir* **2007**, 23 (10), 5769–5778. <https://doi.org/10.1021/la063450z>.
- (58) Sudre, G.; Olanier, L.; Tran, Y.; Hourdet, D.; Creton, C. Reversible Adhesion between a Hydrogel and a Polymer Brush. *Soft Matter* **2012**, 8 (31), 8184–8193. <https://doi.org/10.1039/C2SM25868D>.
- (59) Kim, W.; Jung, J. Polymer Brush: A Promising Grafting Approach to Scaffolds for Tissue Engineering. *BMB Rep* **2016**, 49 (12), 655–661. <https://doi.org/10.5483/BMBRep.2016.49.12.166>.
- (60) Harmon, M. E.; Jakob, T. A. M.; Knoll, W.; Frank, C. W. A Surface Plasmon Resonance Study of Volume Phase Transitions in - PDF Free Download. datapdf.com. <https://datapdf.com/a-surface-plasmon-resonance-study-of-volume-phase-transition.html> (accessed 2022-06-30).
- (61) Bashir, R.; Hilt, J. Z.; Elibol, O.; Gupta, A.; Peppas, N. A. Micromechanical Cantilever as an Ultrasensitive PH Microsensor. *Appl. Phys. Lett.* **2002**, 81 (16), 3091–3093. <https://doi.org/10.1063/1.1514825>.
- (62) Bhatta, D.; Christie, G.; Madrigal-González, B.; Blyth, J.; Lowe, C. R. Holographic Sensors for the Detection of Bacterial Spores. *Biosensors and Bioelectronics* **2007**, 23 (4), 520–527. <https://doi.org/10.1016/j.bios.2007.06.006>.

- (63) Liang, L.; Feng, X.; Peurrung, L.; Viswanathan, V. Temperature-Sensitive Membranes Prepared by UV Photopolymerization of N-Isopropylacrylamide on a Surface of Porous Hydrophilic Polypropylene Membranes. *Journal of Membrane Science* **1999**, 162 (1), 235–246. [https://doi.org/10.1016/S0376-7388\(99\)00145-3](https://doi.org/10.1016/S0376-7388(99)00145-3).
- (64) Bullett, N. A.; Talib, R. A.; Short, R. D.; McArthur, S. L.; Shard, A. G. Chemical and Thermo-Responsive Characterisation of Surfaces Formed by Plasma Polymerisation of N-Isopropyl Acrylamide. *Surface and Interface Analysis* **2006**, 38 (7), 1109–1116. <https://doi.org/10.1002/sia.2318>.
- (65) Pan, Y. V.; Wesley, R. A.; Luginbuhl, R.; Denton, D. D.; Ratner, B. D. Plasma Polymerized N-Isopropylacrylamide: Synthesis and Characterization of a Smart Thermally Responsive Coating. *Biomacromolecules* **2001**, 2 (1), 32–36. <https://doi.org/10.1021/bm0000642>.
- (66) Tamirisa, P. A.; Hess, D. W. Water and Moisture Uptake by Plasma Polymerized Thermoresponsive Hydrogel Films. *Macromolecules* **2006**, 39 (20), 7092–7097. <https://doi.org/10.1021/ma060944u>.
- (67) Förch, R.; Chifen, A. N.; Bousquet, A.; Khor, H. L.; Jungblut, M.; Chu, L.-Q.; Zhang, Z.; Osey-Mensah, I.; Sinner, E.-K.; Knoll, W. Recent and Expected Roles of Plasma-Polymerized Films for Biomedical Applications. *Chemical Vapor Deposition* **2007**, 13 (6–7), 280–294. <https://doi.org/10.1002/cvde.200604035>.
- (68) Sorber, J.; Steiner, G.; Schulz, V.; Guenther, M.; Gerlach, G.; Salzer, R.; Arndt, K.-F. Hydrogel-Based Piezoresistive PH Sensors: Investigations Using FT-IR Attenuated Total Reflection Spectroscopic Imaging. *Anal Chem* **2008**, 80 (8), 2957–2962. <https://doi.org/10.1021/ac702598n>.
- (69) Richter, A.; Bund, A.; Keller, M.; Arndt, K.-F. Characterization of a Microgravimetric Sensor Based on PH Sensitive Hydrogels. *Sensors and Actuators B: Chemical* **2004**, 99 (2), 579–585. <https://doi.org/10.1016/j.snb.2004.01.011>.
- (70) Aussenegg, F. R.; Brunner, H.; Leitner, A.; Lobmaier, Ch.; Schalkhammer, Th.; Pittner, F. The Metal Island Coated Swelling Polymer over Mirror System (MICSPOMS): A New Principle for Measuring Ionic Strength. *Sensors and Actuators B: Chemical* **1995**, 29 (1), 204–209. [https://doi.org/10.1016/0925-4005\(95\)01684-8](https://doi.org/10.1016/0925-4005(95)01684-8).

- (71) Guenther, M.; Kuckling, D.; Corten, C.; Gerlach, G.; Sorber, J.; Suchaneck, G.; Arndt, K.-F. Chemical Sensors Based on Multiresponsive Block Copolymer Hydrogels. *Sensors and Actuators B: Chemical* **2007**, 126 (1), 97–106. <https://doi.org/10.1016/j.snb.2006.10.054>.
- (72) Gupta, S.; Kuckling, D.; Kretschmer, K.; Choudhary, V.; Adler, H.-J. Synthesis and Characterization of Stimuli-Sensitive Micro- and Nanohydrogels Based on Photocross-linkable Poly(Dimethylaminoethyl Methacrylate). *Journal of Polymer Science Part A: Polymer Chemistry* **2007**, 45 (4), 669–679. <https://doi.org/10.1002/pola.21846>.
- (73) Heijl, J.; Du Prez, F. Fast, Multi-Responsive Microgels Based on Photo-Cross-linkable Poly (2-(Dimethylamino)Ethyl Methacrylate). *POLYMER* **2004**, 45 (20), 6771–6778.
- (74) Matsukuma, D.; Yamamoto, K.; Aoyagi, T. Stimuli-Responsive Properties of N-Isopropylacrylamide-Based Ultrathin Hydrogel Films Prepared by Photo-Cross-Linking. *Langmuir* **2006**, 22 (13), 5911–5915. <https://doi.org/10.1021/la060438y>.
- (75) von Recum, H. A.; Kim, S. W.; Kikuchi, A.; Okuhara, M.; Sakurai, Y.; Okano, T. Novel Thermally Reversible Hydrogel as Detachable Cell Culture Substrate. *J Biomed Mater Res* **1998**, 40 (4), 631–639. [https://doi.org/10.1002/\(sici\)1097-4636\(19980615\)40:4<631::aid-jbm15>3.0.co;2-i](https://doi.org/10.1002/(sici)1097-4636(19980615)40:4<631::aid-jbm15>3.0.co;2-i).
- (76) Kuckling, D. Responsive Hydrogel Layers—from Synthesis to Applications. *Colloid and Polymer Science* **2009**, 8 (287), 881–891. <https://doi.org/10.1007/s00396-009-2060-x>.
- (77) Liu, H.; Ito, Y. Gradient Micropattern Immobilization of a Thermo-Responsive Polymer to Investigate Its Effect on Cell Behavior. *J Biomed Mater Res A* **2003**, 67 (4), 1424–1429. <https://doi.org/10.1002/jbm.a.20004>.
- (78) Hoffmann, J.; Plötner, M.; Kuckling, D.; Fischer, W.-J. Photopatterning of Thermally Sensitive Hydrogels Useful for Microactuators. *Sensors and Actuators A: Physical* **1999**, 77 (2), 139–144. [https://doi.org/10.1016/S0924-4247\(99\)00080-1](https://doi.org/10.1016/S0924-4247(99)00080-1).
- (79) Li, M.; Bresson, B.; Cousin, F.; Fretigny, C.; Tran, Y. Submicrometric Films of Surface-Attached Polymer Network with Temperature-Responsive Properties. *Langmuir* **2015**, 31 (42), 11516–11524. <https://doi.org/10.1021/acs.langmuir.5b02948>.

- (80) Delavoipière, J.; Tran, Y.; Verneuil, E.; Heurtefeu, B.; Hui, C. Y.; Chateauinois, A. Friction of Poroelastic Contacts with Thin Hydrogel Films. *Langmuir* **2018**, *34* (33), 9617–9626. <https://doi.org/10.1021/acs.langmuir.8b01466>.
- (81) Koc, J.; Schönemann, E.; Amuthalingam, A.; Clarke, J.; Finlay, J. A.; Clare, A. S.; Laschewsky, A.; Rosenhahn, A. Low-Fouling Thin Hydrogel Coatings Made of Photo-Cross-Linked Polyzwitterions. *Langmuir* **2019**, *35* (5), 1552–1562. <https://doi.org/10.1021/acs.langmuir.8b02799>.
- (82) Chollet, B.; Li, M.; Martwong, E.; Bresson, B.; Fretigny, C.; Tabeling, P.; Tran, Y. Multiscale Surface-Attached Hydrogel Thin Films with Tailored Architecture. *ACS Appl. Mater. Interfaces* **2016**, *8* (18), 11729–11738. <https://doi.org/10.1021/acsami.6b00446>.
- (83) Chollet, B.; D'Eramo, L.; Martwong, E.; Li, M.; Macron, J.; Mai, T. Q.; Tabeling, P.; Tran, Y. Tailoring Patterns of Surface-Attached Multiresponsive Polymer Networks. *ACS Appl. Mater. Interfaces* **2016**, *8* (37), 24870–24879. <https://doi.org/10.1021/acsami.6b07189>.
- (84) Posner, T. Beiträge Zur Kenntniss Der Ungesättigten Verbindungen. II. Ueber Die Addition von Mercaptanen an Ungesättigte Kohlenwasserstoffe. *Berichte der deutschen chemischen Gesellschaft* **1905**, *38* (1), 646–657. <https://doi.org/10.1002/cber.190503801106>.
- (85) Kassahun, G. S.; Griveau, S.; Juillard, S.; Champavert, J.; Ringuedé, A.; Bresson, B.; Tran, Y.; Bedioui, F.; Slim, C. Hydrogel Matrix-Grafted Impedimetric Aptasensors for the Detection of Diclofenac. *Langmuir* **2020**, *36* (4), 827–836. <https://doi.org/10.1021/acs.langmuir.9b02031>.
- (86) D'Eramo, L.; Chollet, B.; Leman, M.; Martwong, E.; Li, M.; Geisler, H.; Dupire, J.; Kerdraon, M.; Vergne, C.; Monti, F.; Tran, Y.; Tabeling, P. Microfluidic Actuators Based on Temperature-Responsive Hydrogels. *Microsyst Nanoeng* **2018**, *4* (1), 1–7. <https://doi.org/10.1038/micronano.2017.69>.
- (87) Martwong, E.; Tran, Y. Lower Critical Solution Temperature Phase Transition of Poly(PEGMA) Hydrogel Thin Films. *Langmuir* **2021**, *acs.langmuir.1c01165*. <https://doi.org/10.1021/acs.langmuir.1c01165>.

- (88) Daehler, A.; Boskovic, S.; Gee, M. L.; Separovic, F.; Stevens, G. W.; O'Connor, A. J. Postsynthesis Vapor-Phase Functionalization of MCM-48 with Hexamethyldisilazane and 3-Aminopropyldimethylethoxysilane for Bioseparation Applications. *J. Phys. Chem. B* **2005**, 109 (34), 16263–16271. <https://doi.org/10.1021/jp0511799>.
- (89) alkoxysilanesstability - Gelest, Inc. <https://www.gelest.com/themencode-pdf-viewer/?file=https://www.gelest.com/wp-content/uploads/alkoxysilanesstability.pdf> (accessed 2022-04-01).
- (90) Xie, Y.; Hill, C. A. S.; Xiao, Z.; Militz, H.; Mai, C. Silane Coupling Agents Used for Natural Fiber/Polymer Composites: A Review. *Composites Part A: Applied Science and Manufacturing* **2010**, 41 (7), 806–819. <https://doi.org/10.1016/j.compositesa.2010.03.005>.
- (91) Silberzan, P.; Leger, L.; Ausserre, D.; Benattar, J. J. Silanation of Silica Surfaces. A New Method of Constructing Pure or Mixed Monolayers. *Langmuir* **1991**, 7 (8), 1647–1651. <https://doi.org/10.1021/la00056a017>.
- (92) Hoff, J. D.; Cheng, L.-J.; Meyhöfer, E.; Guo, L. J.; Hunt, A. J. Nanoscale Protein Patterning by Imprint Lithography. *Nano Lett.* **2004**, 4 (5), 853–857. <https://doi.org/10.1021/nl049758x>.
- (93) Dejeu, J.; Gauthier, M.; Rougeot, P.; Boireau, W. Adhesion Forces Controlled by Chemical Self-Assembly and PH: Application to Robotic Microhandling. *ACS Appl. Mater. Interfaces* **2009**, 1 (9), 1966–1973. <https://doi.org/10.1021/am900343w>.
- (94) Wazawa, T.; Ishizuka-Katsura, Y.; Nishikawa, S.; Iwane, A. H.; Aoyama, S. Grafting of Poly(Ethylene Glycol) onto Poly(Acrylic Acid)-Coated Glass for a Protein-Resistant Surface. *Anal. Chem.* **2006**, 78 (8), 2549–2556. <https://doi.org/10.1021/ac052102j>.
- (95) Jones, K. Optimisation Procedure for the Silanisation of Silicas for Reversed-Phase High-Performance Liquid Chromatography: II. Detailed Examination of Significant Variables. *Journal of Chromatography A* **1987**, 392, 11–16. [https://doi.org/10.1016/S0021-9673\(01\)94250-5](https://doi.org/10.1016/S0021-9673(01)94250-5).
- (96) Jones, K. Optimisation Procedure for the Silanisation of Silicas for Reversed-Phase High-Performance Liquid Chromatography: I. Elimination of Non-Significant Variables. *Journal of Chromatography A* **1987**, 392, 1–10. [https://doi.org/10.1016/S0021-9673\(01\)94249-9](https://doi.org/10.1016/S0021-9673(01)94249-9).

- (97) Oh, S. J.; Cho, S. J.; Kim, C. O.; Park, J. W. Characteristics of DNA Microarrays Fabricated on Various Aminosilane Layers. *Langmuir* **2002**, 18 (5), 1764–1769. <https://doi.org/10.1021/la0113522>.
- (98) Sagiv, J. Organized Monolayers by Adsorption. 1. Formation and Structure of Oleophobic Mixed Monolayers on Solid Surfaces. *J. Am. Chem. Soc.* **1980**, 102 (1), 92–98. <https://doi.org/10.1021/ja00521a016>.
- (99) Shircliff, R. A.; Martin, I. T.; Pankow, J. W.; Fennell, J.; Stradins, P.; Ghirardi, M. L.; Cowley, S. W.; Branz, H. M. High-Resolution X-Ray Photoelectron Spectroscopy of Mixed Silane Monolayers for DNA Attachment. *ACS Appl. Mater. Interfaces* **2011**, 3 (9), 3285–3292. <https://doi.org/10.1021/am200604q>.
- (100) Lee, I.; Wool, R. P. Controlling Amine Receptor Group Density on Aluminum Oxide Surfaces by Mixed Silane Self Assembly. *Thin Solid Films* **2000**, 379 (1), 94–100. [https://doi.org/10.1016/S0040-6090\(00\)01557-1](https://doi.org/10.1016/S0040-6090(00)01557-1).
- (101) Fadeev, A. Y.; McCarthy, T. J. Binary Monolayer Mixtures: Modification of Nanopores in Silicon-Supported Tris(Trimethylsiloxy)Silyl Monolayers. *Langmuir* **1999**, 15 (21), 7238–7243. <https://doi.org/10.1021/la9903806>.
- (102) Choi, I.; Kim, Y.; Kang, S. K.; Lee, J.; Yi, J. Phase Separation of a Mixed Self-Assembled Monolayer Prepared via a Stepwise Method. *Langmuir* **2006**, 22 (11), 4885–4889. <https://doi.org/10.1021/la0519406>.
- (103) Wang, Y.; Cai, J.; Rauscher, H.; Behm, R. J.; Goedel, W. A. Maleimido-Terminated Self-Assembled Monolayers. *Chemistry – A European Journal* **2005**, 11 (13), 3968–3978. <https://doi.org/10.1002/chem.200400896>.
- (104) Silberzan, P.; Léger, L. Evidence for a New Spreading Regime between Partial and Total Wetting. *Phys. Rev. Lett.* **1991**, 66 (2), 185–188. <https://doi.org/10.1103/PhysRevLett.66.185>.
- (105) Wallraff, G. M.; Hinsberg, W. D. Lithographic Imaging Techniques for the Formation of Nanoscopic Features. *Chem. Rev.* **1999**, 99 (7), 1801–1822. <https://doi.org/10.1021/cr980003i>.

- (106) del Barrio, J.; Sánchez-Somolinos, C. Light to Shape the Future: From Photolithography to 4D Printing. *Advanced Optical Materials* **2019**, 7 (16), 1900598. <https://doi.org/10.1002/adom.201900598>.
- (107) Gates, B. D.; Xu, Q.; Stewart, M.; Ryan, D.; Willson, C. G.; Whitesides, G. M. New Approaches to Nanofabrication: Molding, Printing, and Other Techniques. *Chem Rev* **2005**, 105 (4), 1171–1196. <https://doi.org/10.1021/cr030076o>.
- (108) Noyce, R. Semiconductor Device-and-Lead Structure, Reprint of U.S. Patent 2,981,877 (Issued April 25, 1961. Filed July 30, 1959). *IEEE Solid-State Circuits Newsletter* **2007**. <https://doi.org/10.1109/N-SSC.2007.4785577>.
- (109) Kilby, J. S. Miniaturized Electronic Circuits (U. S. Patent No. 3,138, 743). *IEEE Solid-State Circuits Newsl.* **2007**, 12 (2), 44–54. <https://doi.org/10.1109/N-SSC.2007.4785580>.
- (110) Berkowski, K. L.; Plunkett, K. N.; Yu, Q.; Moore, J. S. Introduction to Photolithography: Preparation of Microscale Polymer Silhouettes. *J. Chem. Educ.* **2005**, 82 (9), 1365. <https://doi.org/10.1021/ed082p1365>.

2. Surface-attached hydrogel films with controlled interfacial strength and defects

RÉSUMÉ

Les films d'hydrogel sur des substrats solides combinent les avantages des hydrogels, lubrification et biocompatibilité, avec la rigidité des substrats. Un bon film d'hydrogel doit avoir une bonne adhérence avec le substrat alors que ses caractéristiques topographiques doivent être aussi peu perturbées que possible par le changement d'humidité ou l'immersion qui induisent le gonflement de l'hydrogel. Les propriétés physico-chimiques, telles la densité de réticulation entre les chaînes et la densité de greffage sur les substrats, doivent être alors contrôlées de manière très fine. Le défi est donc de proposer une méthode facile et flexible pour développer une plateforme de films d'hydrogels greffés aux substrats et dont l'épaisseur, le gonflement et la densité de greffage peuvent être finement ajustés. Nous rapportons ici la synthèse et le gonflement d'hydrogels de poly(*N*, *N*-diméthylacrylamide) dont la densité de greffage et les défauts locaux à l'interface avec le substrat sont bien contrôlés. Pour obtenir des films d'hydrogel sur une large gamme d'épaisseurs allant de quelques nanomètres à plusieurs micromètres tout en contrôlant finement l'architecture macromoléculaire, nous proposons une approche simple et facile appelée CLAG qui est l'acronyme de Cross-Link And Grafting. Les films minces d'hydrogel attachés à la surface sont préparés par réticulation et greffage simultanés de chaînes polymères préformées et fonctionnalisées par chimie click. Les chaînes polymères préformées et fonctionnalisées par des groupes alcène sont déposées sur un substrat modifié thiol pour être réticulées et greffées par réaction thiol-ène. Le gonflement du film d'hydrogel est piloté par le taux de réticulation qui est finement contrôlé par le taux de fonctionnalisation -ène. L'adhérence à l'interface est ajustée par la densité de greffage de la couche d'hydrogel qui est finement contrôlée par la quantité de thiol greffé sur le substrat. La quantité de thiol peut être modifiée en mélangeant le thiol réactif avec le propylsilane passif

dans le processus de silanisation. L'adhérence à l'interface peut également être ajustée localement en dessinant des zones passives où l'hydrogel n'est pas accroché sur le substrat. Ceci a été réalisé en passivant le thiol sur des lignes sélectionnées par irradiation UV à travers des masques pour activer la réaction thiol-ène.

ABSTRACT

Hydrogel coatings on rigid substrates combine the advantages of hydrogels, such as lubricity and biocompatibility, along with the benefits of stiffness and toughness of substrates. A good hydrogel coating should have good adhesion with the substrate, while their topographical features should be as little disturbed as possible by humidity change or underwater, which induces the swelling of hydrogel. To achieve this, the physico-chemical properties such as the cross-linking density between chains, and the grafting density to the substrates, must be finely controlled. The challenge is then to propose a facile and versatile method to develop a platform of hydrogel coatings attached to the substrates with controlled thickness, swelling, and interface strength. Here, we report the synthesis and swelling of surface-attached poly(*N*, *N*-dimethylacrylamide) hydrogels with controlled interface strength and local defects. To obtain hydrogel films over a wide range of thicknesses from a few nanometers to several micrometers while the macromolecular architecture is finely controlled, we propose a facile and versatile approach called CLAG which is the acronym of Cross-Link And Grafting. The surface-attached hydrogel thin films are prepared by simultaneous cross-linking and grafting preformed and functionalized polymer chains by click chemistry. Preformed ene-functionalized polymer chains are coated on a thiol-modified substrate to be cross-linked and grafted through a thiol-ene reaction. The swelling of the hydrogel film is ruled by the cross-linking ratio, which is finely controlled by the ratio of ene-functionalized polymer. The interface strength is adjusted with the grafting density of the hydrogel layer, which is finely controlled by the amount of thiol grafted on the substrate. The amount of thiol can be varied by mixing reactive thiol with passive propylsilane in the silanization process. The interface strength can also be adjusted locally by patterning passive zones where the hydrogel is not attached. This was achieved by passivating thiol on selected lines by UV irradiation through masks to activate the thiol-ene reaction.

Table of contents

| | |
|--|----|
| 1. Introduction..... | 44 |
| 2. Experimental Methods | 47 |
| 2.1. Synthesis of thin films | 47 |
| 2.1.1. Materials..... | 47 |
| 2.1.2. Synthesis of ene-functionalized PDMA..... | 47 |
| 2.1.3. Variation of the grafting density by mixing silanes | 48 |
| 2.1.4. Preparation of mask for lithography..... | 48 |
| 2.1.5. Passivation of thiol | 49 |
| 2.1.6. Preparation of surface-attached PDMA hydrogels..... | 49 |
| 2.2. Characterization techniques..... | 49 |
| 2.2.1. Contact angle measurements..... | 49 |
| 2.2.2. Spectroscopic Ellipsometry..... | 50 |
| 2.2.3. Microscopic Ellipsometry | 51 |
| 2.2.4. X-ray Photoelectron Spectroscopy..... | 51 |
| 2.2.5. ToF-SIMS..... | 51 |
| 2.2.6. Debonding experimental set-up | 52 |
| 3. Results and Discussion | 53 |
| 3.1. Preparation of surface-attached hydrogel films using CLAG strategy..... | 53 |
| 3.2. Control of the interfacial strength by varying the grafting density | 55 |
| 3.3. Control of local defects by passivation of thiol..... | 58 |
| 3.4. Swelling-induced wrinkles and delamination of surface-attached hydrogel films.... | 61 |
| 4. Conclusion | 64 |
| 5. References..... | 66 |
| 6. Supporting Information..... | 71 |

1. Introduction

Hydrogel coatings on rigid substrates have a keen study due to their high application in various fields. They can mimic *in vivo* mechanical environments for cell culture, responsive coatings, sensors, and active components for microfluidic coatings.¹⁻⁴ Hydrogel coatings substrates combine the advantages of hydrogels, such as lubricity and biocompatibility properties, along with the benefits of substrates, such as stiffness and toughness.⁵⁻¹⁰

An ideal hydrogel coating should achieve two features. First, good adhesion between the substrate and the hydrogel coating has to be kept in any condition, eventually with environmental change. When the hydrogel coating is exposed to air or humidity underwater, the adhesion on the substrate can change from good to bad, resulting in detachment of the coating. Second, the topographical aspect should be as little disturbed as possible by the environmental change. Hydrogel coatings actually can exhibit instabilities such as wrinkles on the surface due to the change of swelling. As the thickness of the hydrogel layer is much lower than the lateral dimension, the hydrogel can only swell in the direction perpendicular to the substrate and can undergo compressive stresses parallel to the substrate.¹¹⁻¹⁷ When these compressive stresses become greater than the buckling threshold of the elastic layer, they give rise to buckling instabilities that relax these stresses.¹⁸⁻²²

When the hydrogel coating is not sufficiently strongly bound to the substrate, swelling stresses can result in interface delamination. The delamination process can lead to large-scale folding and blistering of the hydrogel films. This is often promoted with minor defects in the interface between the hydrogel and the substrate. These defects can affect the durability of coatings. This buckle delamination is usually considered to be an undesirable and uncontrollable phenomenon. However, by finely controlling the adhesive region between the thin layer and substrate, it is possible to develop a sustainable hydrogel coating with longer durability.

Then a challenge would be to propose a facile and versatile method to develop a platform of hydrogel coatings attached to the substrates with controlled physico-chemical properties such as thickness, swelling, and interface strength. This would help to understand and prevent from the delamination of the coating from the substrate. The key point is then the fine control of the physical chemistry of the substrate/gel interface (nature of the chemical bonds, grafting density) and of the film properties (swelling ratio, thickness) so as to control and predict the failure of the coatings during swelling.

Recently, our group has developed surface-attached hydrogel films, which can be varied over a wide range of thicknesses from a few nanometers to several micrometers, while the macromolecular architecture is finely controlled. We proposed a facile and versatile approach which enables the development of a platform of surface-attached hydrogel films with well-controlled chemistry. We called this approach CLAG which is the acronym of Cross-Link And Grafting. The surface-attached hydrogel thin films are prepared by simultaneously cross-linking and grafting preformed and functionalized polymer chains by click chemistry, as shown in figure 1.^{23–27}

The click chemistry we chose is the thiol-ene reaction²⁸ as it can be activated by heating (at temperatures below the temperature of polymer degradation) or by UV irradiation (at 250 nm without the need of a photoinitiator). Moreover, numerous thiol chemicals are easily available for grafting onto substrates and for the chemical cross-linking between functionalized chains. For example, mercaptosilanes are used for grafting onto oxide layers (silicon and glass substrates, silica, titanium oxide...). Dithiol cross-linkers with specific spacers are chosen to adapt to the polymers. Dithiol cross-linkers can also react with each other to form stable disulfide bridges of flexible lengths, which promote the connection between polymer chains for the formation of the chemical network.

The key aspect of the CLAG approach is to start with preformed polymer chains. As radical polymerization is highly sensitive to oxygen (it is worth for coating due to the high surface to volume ratio), it is very difficult to well control the synthesis of the polymer network on the surface if the process starts with coated monomers. Ene-functionalized polymer chains are first synthesized by the free radical polymerization method. This is also one of the great advantages of the CLAG approach, as free radical polymerization is a straightforward method which allows low and high polymer molecular weight contrary to controlled radical polymerization. And here, there is no need of narrow distribution of polymer chains as they are dedicated to be cross-linked. This enables us to generalize the CLAG approach to various hydrogels made with acrylate- and acrylamide- polymers such as poly(*N, N*-dimethylacrylamide) (PDMA)²³, poly(acrylic acid) (PAA)²⁹, poly(*N*-isopropylacrylamide) (PNIPAM)^{26,30–32} and poly[poly(ethylene glycol) methyl ether methacrylate] poly(PEGMA).³³ The ene-functionalized polymers synthesized can be then purified and recovered (by freeze-drying or precipitation). The ratio of ene-functionalization, which can be finely characterized, will rule the cross-linking ratio and then the swelling of the hydrogel layer.

The ene-functionalized polymers are then solubilized in a proper solvent with suitable dithiol cross-linkers before being coated on the thiol-modified substrates. Different coating methods can be used, such as spray-coating, spin-coating, and dip-coating, depending on the thickness range desired. Spin-coating is often used because it requires little polymer, and it allows the formation of polymer films widely ranging from a few nanometers to several micrometers, which is well suited to our studies. After the spin-coating of polymer films on the treated substrates, the cross-linking and surface-grafting of polymer chains are achieved by activating the thiol-ene click reaction either by heating to obtain hydrogel films or by UV irradiation to obtain hydrogel patterns. It means that the synthesis of surface-attached hydrogels is performed in a dry state without solvent (in melting polymer condition).

The control of the interface strength is another key point. The interface strength is ruled by the grafting density of the hydrogel to the surface. It can be controlled by the silanization of reactive species on the substrate. Adapted to our CLAG approach, the grafting density can be varied by mixing reactive thiol with passive silane such as propyltrimethoxysilane on the silicon substrate. Moreover, a detailed investigation of the debonding mechanisms under the action of swelling stresses requires that delamination is induced from well controlled defects with low adhesion (see chapter 3). The formation of such localized defects from the inhibition of hydrogel/substrate adhesion can be achieved by locally passivated thiol-grafted groups with reactive small molecules before coating the ene-functionalized polymer on the substrate. This is realized using photolithography-like technique exploiting the versatility of the thiol-ene click reaction, which is activated by UV irradiation.

Here, we report the synthesis of surface-attached poly(*N*, *N*-dimethylacrylamide) hydrogels using the CLAG approach. We show that their thickness can be adjusted on a large range and the swelling can be well controlled. Ellipsometry is used to measure the thickness in air and water. Within the framework of a collaboration with Nicolas Gauthier and Marc Veillerot at laboratory LETI (CEA Grenoble), we also show that the interface strength can be finely controlled and characterized by XPS and ToF-SIMS techniques.

2. Experimental Methods

2.1. Synthesis of thin films

2.1.1. Materials

N,N-Dimethylacrylamide (DMA, 99%), and acrylic acid (AA, 99%) were purchased from Aldrich and purified prior to use by passing through the basic alumina column to remove inhibitors. *N*-Hydroxysuccinimide (NHS), and *N*-(3-dimethylaminopropyl)-*N*'-ethylcarbodiimide hydrochloride (EDC) and sodium disulfite ($\text{Na}_2\text{S}_2\text{O}_5$) were obtained from Aldrich. Allylamine (98%) and ammonium persulfate, $(\text{NH}_4)_2\text{S}_2\text{O}_8$, (98%) were purchased from Thermo Fischer.

N-Propyltrimethoxysilane (97%) was obtained from ABCR. Anhydrous toluene (anhydrous, 99.8%), (3-mercaptopropyl)trimethoxysilane (95%), and toluene (ACS Reagent grade) were purchased from Aldrich.

1,4-Dithioerythritol, allyl butyl ether (98%), and *N,N*-dimethylformamide (DMF, 99.8%) were obtained from Aldrich and used for the preparation of the polymer hydrogel film.

Silicon wafers with a diameter of 76.2 ± 0.5 mm and thickness of 380 ± 25 μm were obtained from Neyco. Quartz Chromium mask of 5" * 5" * 0.9" with a standard positive photoresist AZ1518 of 360 nm is purchased from MB Whitaker & Associates.

2.1.2. Synthesis of ene-functionalized PDMA

The ene-functionalized poly(*N,N*-dimethylacrylamide) (PDMA) was synthesized by a two-step process. The first step is the free radical copolymerization of dimethylacrylamide and acrylic acid in water using a $(\text{NH}_4)_2\text{S}_2\text{O}_8/\text{Na}_2\text{S}_2\text{O}_5$ redox initiator. 10 g (0.10 mol) of dimethylacrylamide and 0.382 g (5.3 mmol) of acrylic acid are added to 0.052 g (0.97 mmol) of NH_4Cl in 100 mL of water. After adjusting the pH to 3-4 with 1M NaOH, the solution is bubbled for an hour with nitrogen. 0.15 g (0.65 mmol) of $(\text{NH}_4)_2\text{S}_2\text{O}_8$ and 0.0375 g (0.19 mmol) of $\text{Na}_2\text{S}_2\text{O}_5$ are introduced after one hour under nitrogen. The solution is kept at ambient temperature for 24 hours. This solution is then dialyzed for four days and freeze-dried to get purified poly(DMA-*co*-AA) copolymer.

For the ene-functionalization of PDMA, poly(DMA-*co*-AA) copolymer is modified using allylamine. First, 1.47 g (7.66 mmol) of EDC and 1.77 g (15.37 mmol) of NHS are added into

the 10 g of copolymer solution (3-5% of polymer in water), then the pH of the solution is adjusted to 4.5 is left under stirring for two hours at ambient temperature. Then, the aqueous solution of 0.58 g (10.16 mmol) allylamine is added to the medium, associated with the adjustment of the pH to 10 with NaOH, for the formation of the targeted amide bond through the nucleophilic attack of allylamine onto the carboxylic acid. The amification reaction is allowed to proceed for 16 hours at room temperature. The final solution of ene-functionalized PDMA was dialyzed against 0.1 M NaCl for four days and then four days against MilliQ water to remove the excess of EDC, NHS, and allylamine. After the dialysis, it is subsequently recovered by using a freeze-dryer.

2.1.3. Variation of the grafting density by mixing silanes

The silicon wafer is silanized with (3-mercaptopropyl)trimethoxysilane. The silicon wafer is freshly cleaned inside the UV ozone chamber during 20 minutes before being transferred to a sealed reactor filled with nitrogen. A 3% volume of (3-mercaptopropyl) trimethoxysilane in anhydrous toluene is transferred into the reactor (using a cannula) and left for 3 hours. The silicon wafer is then rinsed by toluene and ultra-sonicated. The thickness of the silane self-assembled monolayer on the silicon substrate is measured using ellipsometry.

In order to tune the interface strength of the substrate, we varied the grafting density of the hydrogel film on the silicon wafer by varying the surface density of the active thiol-silane. This was achieved using a reactive mixture of *n*-propyltrimethoxysilane and (3-mercaptopropyl)trimethoxysilane in 3% v/v in anhydrous toluene. A range of 10 to 100% mercaptosilane is used in the silane mixture to get different grafting densities of the reactive thiol group on the surface.

2.1.4. Preparation of mask for lithography

The quartz masks are coated with around 90 nm thick chromium layer and 360 nm photoresist above the chromium layer. The pattern for the defects was then drawn using Clewin software. Then the laser is exposing only to the patterned area. After the patterning, the mask is washed using an AZ 351 B developer. During the bath in the developer, only the exposed resist is removed, which reveals the bare chromium layer underneath the photoresist. Then the exposed chromium layer is etched in an acid bath. The remaining photoresist from the rest of the area is removed by using acetone, as shown in the Supporting Information (Figure S4).

2.1.5. Passivation of thiol

For the local passivation of the active thiol groups, five different chemicals with allyl end-group exhibiting different vapor pressure, surface tension, and molecular weight were tested: allyl butyl ether, *N, N*-dimethylallylamine, allyl acetate, allyl acetoacetate, and allyl-terminated PEG. Passivation was achieved by chemical bonding of the allyl passivator with the mercaptosilane using the thiol-ene click reaction. This thiol-ene reaction is activated by deep UV exposure (at 254 nm) combined with photolithography techniques. We found that allyl butyl ether was the best candidate to passivate the thiol groups under UV radiation while being non-reactive with the PDMA hydrogel. Using this technique, we made patterns on silicon substrates with passivated areas in the form of lines for the investigation of swelling induced delamination. Using chromium-coated quartz lithography masks, we designed line patterns with different widths ranging between 2 and 100 μm .

2.1.6. Preparation of surface-attached PDMA hydrogels

The surface-attached PDMA hydrogels are obtained by using simultaneous cross-linking and grafting of the ene-functionalized polymers through a thiol-ene click reaction.^{23,24,26,27} The ene-functionalized PDMA is dissolved in dimethylformamide (DMF) overnight. 1,4-dithioerythritol as a cross-linker is added to the polymer solution just before the spin-coating. The ratio of dithiol to the ene-functionalized polymer is 15 times to have flexible length to form disulfide groups³³. This solution is spin-coated on the modified silicon wafer with an angular velocity of 3000 rpm for 30 seconds to achieve a thin and homogenous film. The thickness of the film is controlled by the concentration of the polymer in the solution. After spin-coating, the film is kept at 150°C under a vacuum for 24 hours. The films are then rinsed and sonicated in DMF and then in water to eliminate the excess of 1,4-dithioerythritol and free unreacted polymers.

2.2. Characterization techniques

2.2.1. Contact angle measurements

The results of contact angle experiments are provided in the Supporting Information. Water droplets onto both cleaned and silanized wafers were deposited, and their contact angle was measured. These experiments qualitatively show the change of contact angle with various silanization on the substrate. The contact angle observed is the lowest (about 20°) for freshly cleaned silicon wafers by UV-ozone. As expected, the silanized silicon wafers show higher

contact angles, depending on the hydrophobic properties of grafted silane species (propylsilane, mercaptosilane without and with added allyl butyl ether).

2.2.2. Spectroscopic Ellipsometry

The thickness of the oxide layer and the thickness of dry and swollen hydrogels are measured using a spectroscopic ellipsometer (UVISEL, Horiba). All the measurements are done with a fixed angle of 60° and by varying the wavelength from 400 nm to 800 nm. The underwater experiments were made using a liquid cell whose windows are perpendicular to the laser beam, the silicon wafers being stably kept at the bottom of the liquid cell. The complex refractive index (n) of the silicon substrate is 3.87, with an imaginary part equal to 0.02i. A model with two layers was used for oxide and silane layers on the silicon wafer. A three-layered model was utilized to determine the thickness of the surface-attached hydrogel layer. The first and second layers correspond to silica and SiO_2 ($n = 1.46$), the thickness of which was determined before spin-coating the polymer film. The third layer to be determined corresponds to the hydrogel layer. The swollen thickness is determined from the best fit of the experimental data (IS and IC ellipsometric intensities) using a three-layers model with water as the ambient atmosphere. The polymer and water refractive index are calculated using a Cauchy transparent model as in equation 1 and 2.

$$n_p(\lambda) = A_p + \frac{B_p \cdot 10^4}{\lambda^2} + \frac{C_p \cdot 10^9}{\lambda^4} \quad \text{Eq. 1}$$

$$n_w(\lambda) = A_w + \frac{B_w \cdot 10^4}{\lambda^2} + \frac{C_w \cdot 10^9}{\lambda^4} \quad \text{Eq. 2}$$

where $n(\lambda)$ is the refractive index of the material and λ is the wavelength A_p , B_p , C_p , and A_w , B_w , C_w are Cauchy's coefficients for polymer and water, respectively. Typically at $\lambda = 600$ nm, $n_p = 1.42$ and $n_w = 1.33$.

The swollen hydrogel refractive index $n(\lambda, \phi_p)$ is calculated assuming linear mixing law:

$$n(\lambda, \phi_p) = (1 - \phi_p) n_w(\lambda) + \phi_p n_p(\lambda) \quad \text{Eq. 3}$$

Where ϕ_p the volume fraction of polymer in the hydrogel layer. As the attachment of the polymer network is a covalent bond, the amount of polymer in air and water has to be the same. It results that, the volume fraction of polymer in the hydrogel layer has to be equal to the ratio of the dry thickness to the swollen thickness. Full details about ellipsometry are given in appendix A.

2.2.3. Microscopic Ellipsometry

The patterns corresponding to the passivation of thiol were characterized with a microscopic ellipsometer (Nanofilm EP3, Accurion). This ellipsometry has a Xenon lamp as a light source with a filter at a wavelength of 590.8 nm. The angle of incidence is fixed to 65° while measuring the samples. This ellipsometry consists of a camera and 5x objective, which can take millimeter-size images. The lateral resolution of this microscopic ellipsometry is 2 micrometers. Nulling ellipsometry is done for each pixel in the image, and Δ map is obtained from which the width of the passivated line will be measured.

2.2.4. X-ray Photoelectron Spectroscopy

Silane monolayers were characterized with XPS using a PHI 5000 Versa Probe II photoelectron spectrometer at the Nano Characterization Platform (PFNC). A 200 μm diameter monochromatic Al-K α ($h\nu = 1486.6$ eV) X-ray light source was used for analyses. The source analyzer angle is 45° and remains unchanged during the AR-XPS data acquisition, where the photoelectron take-off angle (sample-analyzer angle) varies. The overall energy resolution (taking into account both the spectrometer and X-ray bandwidths) is 0.6 eV for core level (CL) spectra, and we set the C 1s peak from the adventitious carbon to 284.8 eV for calibration of the binding energy scale. Data treatment and peak deconvolution were performed with the CasaXPS software. The sensitivity factors provided by the instrument were used to perform the relative quantification of the elements.

2.2.5. ToF-SIMS

ToF-SIMS measurements were performed using a ToF SIMS 5 Instrument from ION TOF GmbH equipped with a 30 kV Bismuth-LMIG. For secondary ions analysis, the LMIG gun was tuned to deliver primary analysis ions Bi 3^+ energized at 15 kV with a current of 0.51 pA.

The analysis area of $100 \times 100 \mu\text{m}^2$ is described in 128×128 pixels for negative polarity secondary ions. The final mass spectra are given by the accumulation of counts for a total primary ion dose which is equal to 1×10^{12} ions/cm².

For image acquisitions, we analyzed an area of $400 \times 400 \mu\text{m}^2$ described in 256×256 pixels.

2.2.6. Debonding experimental set-up

A steady-state swelling of the film was achieved under a constant vapor flow, ensuring the saturation of the hydrogel layer by using a homemade setup.²³ The vapor is advected above the sample in a laminar flow, and the vapor flow toward the film is set by the temperature difference between the film and the vapor flow. The substrate temperature is controlled by a Peltier module and set at 10°C below the temperature of the incoming water vapor. The relative humidity in the chamber is always kept constant at around 60%. The upper wall of the chamber is a glass window allowing observation of the film by means of a zoom lens (Apo Z16, Leica) and a CCD camera (1600×1200 , 8 bits). Full details regarding the setup are provided in the reference.²³

3. Results and Discussion

3.1. Preparation of surface-attached hydrogel films using CLAG strategy

Hydrogel thin films were prepared following the CLAG strategy, which consists of simultaneous Cross-Linking And Grafting of ene-functionalized polymer chains on thiol-modified substrates by thiol-ene click chemistry, as shown in Figure 1.^{23–27} This CLAG strategy allows very fine control of the physico-chemical properties of the hydrogel films such as the crosslinks density of the polymer networks, the grafting density onto the substrate, and the thickness of the film. This strategy requires a pre-formed ene-functionalized polymer which is synthesized by a two-step process. The copolymer containing dimethylacrylamide and acrylic acid was first synthesized by free radical polymerization in water, followed by the ene-functionalization using allylamine. The pre-synthesized ene-functionalized PDMA was then characterized by SEC chromatography and ¹H NMR spectroscopy. The polymer has a molecular weight of 231 kg/mol with a polydispersity index of 1.93. The molar ratio of ene-groups is 0.7%. The NMR spectrum of the ene-functionalized PDMA is given in the Supporting Information.

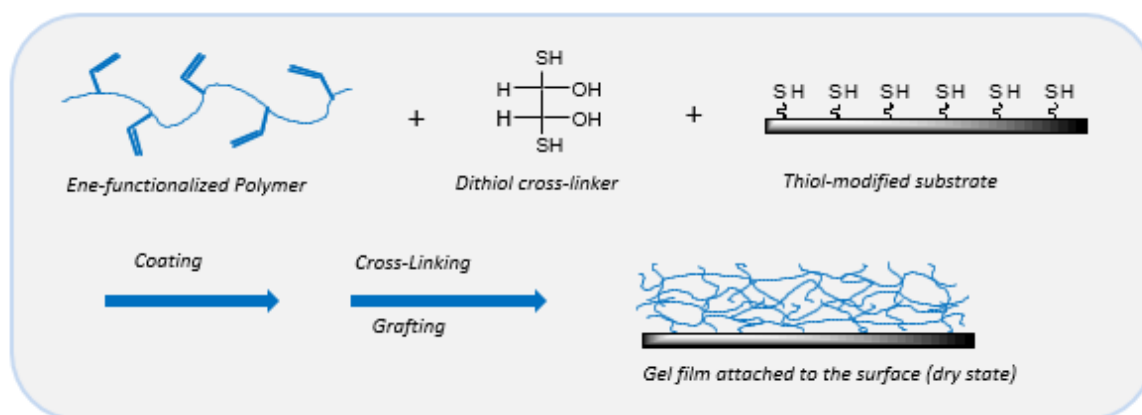


Figure 1: Schematics of the synthesis of hydrogel thin film on glass or silicon substrates using CLAG approach by Cross-Linking And Grafting of ene-functionalized polymer chains onto thiol-modified substrates through thiol-ene click chemistry.

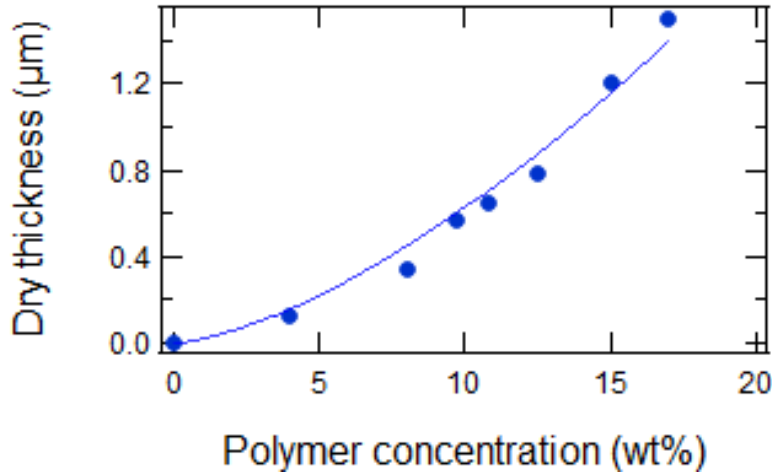


Figure 2. Dry thickness of PDMA hydrogel films as a function of polymer concentration (wt%) with $M_w = 231 \text{ kg/mol}$, $IP = 1.92$. The data are fitted using the hydrodynamic equation³⁴ with $h \propto \omega^{-1/2} M^{\alpha/2} C_p^{3/2}$ where $\omega = 300 \text{ rpm}$, $M = 232 \text{ kg/mol}$, and $\alpha = 0.8$.

The thickness of the film can be adjusted by varying the concentration of the polymer, the molecular weight of the polymer, or by changing the angular speed³⁵. In our studies, we control the film thickness by varying the concentration of the polymer concentration in the solution for spin-coating. Figure 2 shows that the thickness of the film increases with the concentration of the polymer in the solution. In the spin-coating process, the film thinning can be modeled by hydrodynamic equations describing radial out-flow and solvent evaporation.³⁴ The thickness of the polymer layer film can be expressed by the scaling: $h \propto \omega^{-1/2} \eta^{1/2} C_p$, where h is the final thickness of the polymer layer, ω is the angular velocity of the spin-coating, C_p is the concentration of the polymer, and η the initial solution viscosity. As the viscosity of polymer solution can be expressed as a function of the concentration and the molecular weight, the thickness is given by the expression^{26,36,37}: $h \propto \omega^{-1/2} M^{\alpha/2} C_p^{3/2}$ where α is the Mark–Houwink parameter which is between 0.5 and 0.8 (0.5 is for theta solvents and around 0.8 for good solvents).^{38–40} Here the angular velocity and the molecular weight of the polymer are kept constant (3000 rpm and 232 kg/mol). It is shown that experimental data are satisfactorily fitted on a large range of concentrations (from 1 to 20 wt%) and a large range of thicknesses from nanometer to micrometers using $\alpha = 0.8$.

3.2. Control of the interfacial strength by varying the grafting density

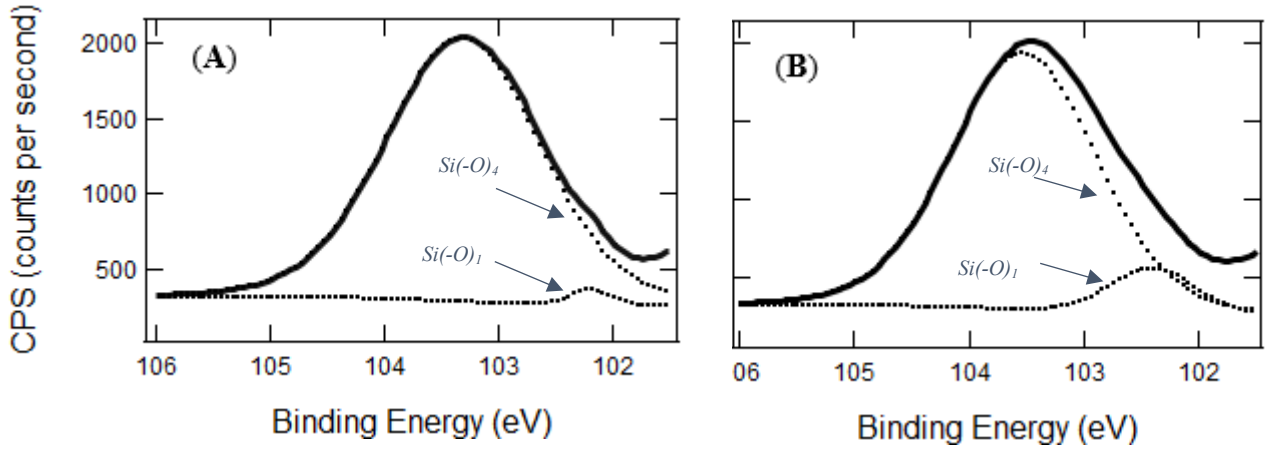


Figure 3. Si 2p XPS spectra of silanized silicon wafers were obtained using 10% of mercaptosilane (A) and 100% of mercapto silane in the mixed silane solutions (B). Dotted lines show fits corresponding to the $\text{Si}(-\text{O})_4$ component from the silica substrate and the $\text{Si}(-\text{O})_1$ from the mercaptosilane.

The interfacial strength of surface-attached hydrogel films was controlled by varying the grafting density of thiol groups on silicon substrates. This goal was achieved by varying the ratio of mercaptosilane and propylsilane in the silanization mixtures while keeping the whole concentration of silane (3%) in the toluene solution. The grafting of hydrogel films will be promoted by the thiol groups (from mercaptosilane) through thiol-ene reaction and not by the passive methyl groups (from propylsilane). The ratio of mercaptosilane in the silanization mixture was varied from 10% to 100%. The grafting density of thiol groups was quantified by combining XPS and ToF-SIMS experiments.

Figure 3 displays Si2p XPS spectra of silanized silicon wafers obtained with various ratios of mercaptosilane. This can be used to quantify the thiol monolayer on silicon substrates. The quantity of thiol group on the surface can be expressed by ^{41,42}

$$\Gamma_{\text{monolayer}} = \frac{t\rho a N_{AV}}{MW} \quad \text{Eq. 4}$$

where t is the thickness of the thiol monolayer measured by ellipsometry ($t = 0.7 \pm 0.2$ nm), ρ is the density of mercaptosilane (1.057 g/mL), a is the conversion factor ($10^{-21} \text{cm}^3/\text{nm}^3$), N_{AV} is the Avogadro's number and MW is the molecular weight of the mercaptosilane (196.34 g/mol). The surface density of the thiol group calculated here is about 2 nm^{-2} .

From XPS experiments, the density of mercaptosilane on the silicon substrate can be deduced using equation 5.

$$\Gamma_{monolayer} = \frac{A_{Si(-O)_1}}{A_{Si_{2p}}} n_{SiO_2} z \quad \text{Eq. 5}$$

z is the measured depth using ARXPS with three different angles, 15° , 45° , and 90° , and averaged to 1 nm. n is the molecular concentration of silica estimated to be 22 molecules/nm³. $A_{Si(-O)_1}$ which is the % Si for the $Si(-O)_1$ (the area under the curve) corresponds to the Si of mercaptosilane. $A_{Si_{2p}}$ is the area of percentage of $(Si(-O)_1 + Si(-O)_4)$, which gives the value of 0.6 molecule/nm². The surface density calculated from Equation 4 is lower than what was calculated using Equation 3.^{41,42} The value deduced from Equation 3 corresponds actually to a saturated surface density, whereas the value deduced from Equation 4 corresponds to a 3% volume of mercaptosilane grafted on 4 to 5 SiOH groups per nm² on the silicon wafer.⁴³

The mass spectra of bare and thiol-modified silicon wafers using ToF-SIMS are shown in Figure 4. They correspond to the negative secondary ion mass spectra (m/z) from 0-120 for an ozone-treated silicon wafer, and thiol-modified silicon wafers using 10% and 100% mercaptosilane in the silane mixtures. The peak associated with OH^- is identified at 17 u. Figure S7 shows a stronger signal for the ozone-treated silicon wafer than for the bare silicon wafer. The ozone treatment allows the formation of hydroxyl group on the surface. The intensity of OH^- peak is unsurprisingly weaker for thiol-modified silicon wafers compared to the clean silicon wafer as the silanol group has reacted with the silane group. In Figure 4, the peaks associated with the S^- and SH^- groups are shown for all the samples. As expected, the peaks corresponding to S^- and SH^- are very weak on ozone-treated silicon wafers. The intensity of S^- and SH^- peaks are quite high for the thiol-modified silicon wafers to be analyzed and quantified. As expected, the intensity of the peaks is lower for the thiol-modified substrates obtained with 10% mercaptosilane than that obtained with 100% mercaptosilane. The comparison of the intensities of S^- and SH^- peaks of both samples allows quantifying the (relative) ratio of thiol groups grafted on the substrates.

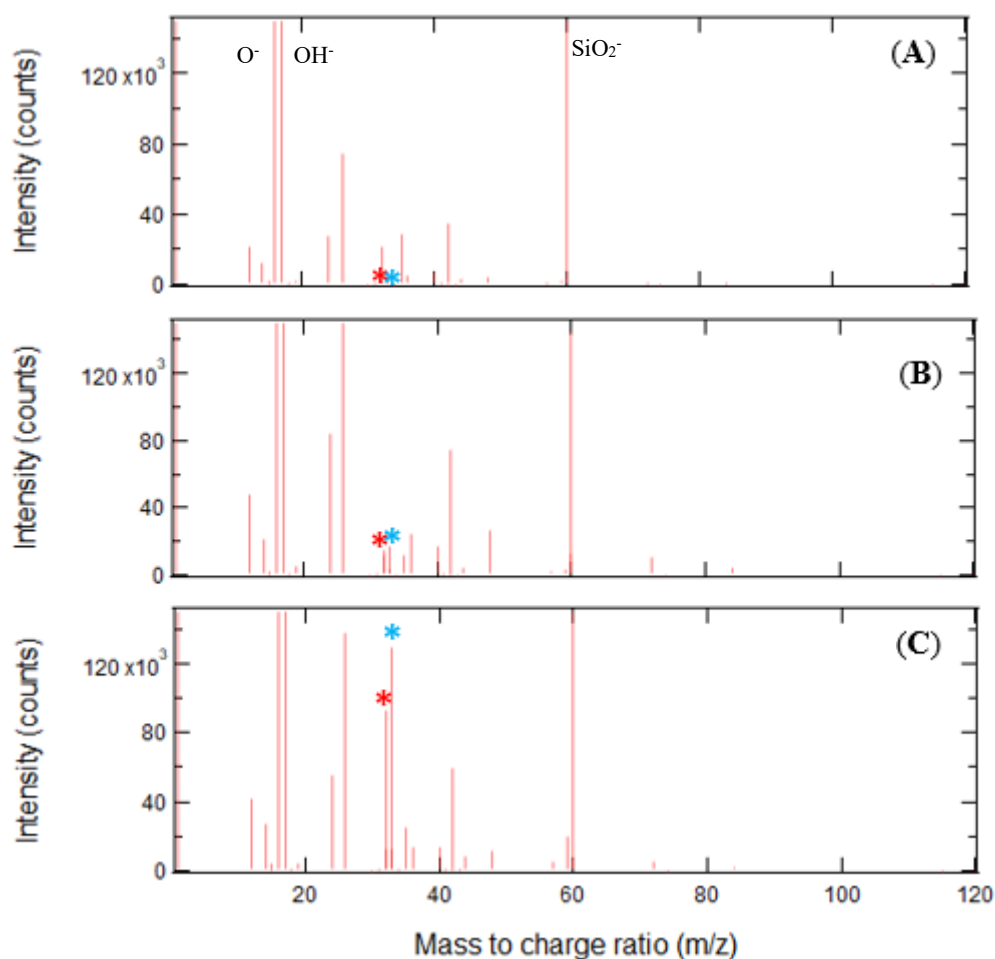


Figure 4. Negative secondary ion mass spectra for m/z from 0 to 120 for silicon wafer with (A) 0%, (B) 10%, and (C) 100% mercapto silane-modified. (*) represents the peak of S^- and (*) represents the peak of SH on the mass spectra.

Figure 5 gives the grafting density of thiol groups in the mixed self-assembled monolayer (containing thiol and methyl groups) as a function of the ratio of mercaptosilane in the silane mixture (containing both mercaptosilane and propylsilane) used for silanization. The grafting density of thiol-modified silicon wafers with 100% of mercaptosilane was determined using XPS. However, it cannot be determined for silanized substrates with silane mixtures due to the limit of detection of XPS. Nevertheless, a combination of XPS and ToF-SIMS experiments allowed us to quantify the grafting density of thiol groups in the mixed self-assembled monolayers. Using a reference density of thiol measured by XPS with the substrate grafted with 100% mercaptosilane, we were able to perform quantitative ToF-SIMS measurements of the amount thiol groups on substrates grafted with less than 100% mercaptosilane. As shown in Figure 5, the grafting density of thiol increases with the ratio of mercaptosilane in the silane

mixtures for silanization. The increase is not linear even if the whole concentration of the silanes in the solution is kept constant (3% in toluene). This is probably due to the difference in reactivity of mercaptosilane and propylsilane regarding silica surface, as mercaptosilane is more polar than propylsilane.

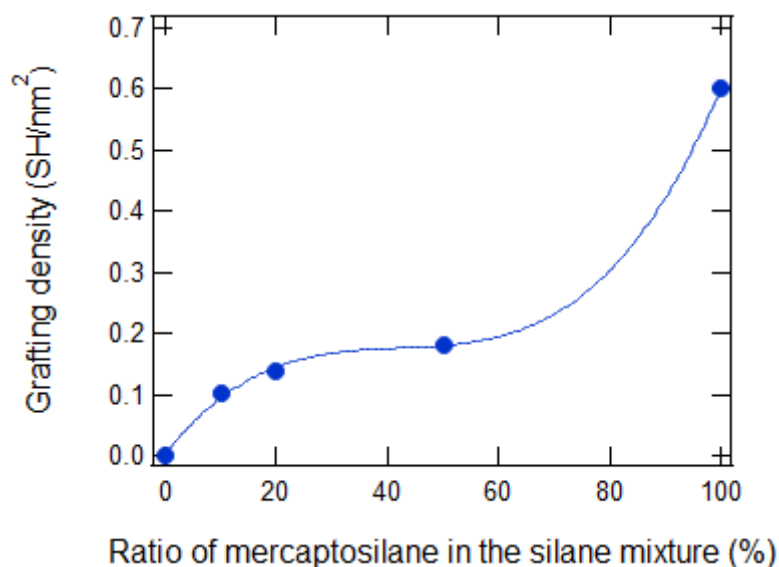


Figure 5. Grafting density of thiol groups in the mixed self-assembled monolayer as a function of the ratio of mercaptosilane in the silane mixtures. The amount of thiol (SH/nm²) grafted on the silicon wafer is calculated by combining XPS and ToF-SIMS measurements.

3.3. Control of local defects by passivation of thiol

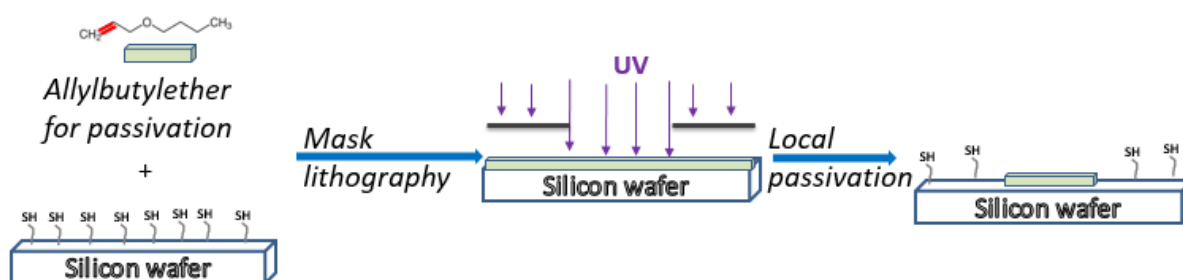


Figure 6. Schematic of the chemical passivation of selected regions of thiol-modified silicon wafer using microlithography and allyl butyl ether as a passivator.

As it will be detailed in the next chapter, debonding mechanisms can be promoted from well-controlled line defects on the substrate where the strength of the interface is reduced. This can be achieved by locally passivating the reactive thiol groups grafted on the silicon substrate. In

order to create such defects, we first needed to identify which chemical can be used to selectively passivate the thiol at the silanized surface. Such a molecule should react with the thiol groups but not with the PDMA hydrogel. The molecule needs to be small so that a thin layer of it should not change the homogeneity of the film and preparation of the film. Five different chemicals with allyl end-group were tested. Among allyl butyl ether, *N,N*-dimethylallylamine, allyl acetate, allyl acetoacetate, and allyl-terminated PEG, we found that allyl butyl ether was the best option. Actually, allyl butyl ether can react well with grafted thiol groups while keeping a good spreading of the PDMA polymer layer during spin-coating to form the grafted hydrogel film.

As depicted in Figure 6, passivated patterns in the form of lines were created on the silicon wafers by passivating the reactive thiol groups with allyl butyl ether. Using chromium-coated quartz lithography masks, we designed line patterns with different widths ranging between 2 and 100 μm . Ellipsometric microscopy enabled us to confirm the chemical bonding of allyl butyl ether on the thiol monolayer over well-defined strips on the silicon wafer. The width and thickness of the passivated lines can be deduced from ellipsometric angle mapping (Figure 7). From the measure of Δ angle, the thickness mapping can be deduced. The thickness profile is shown in Figure 7(C). The average width of the line of added allyl butyl ether to the thiol monolayer can be determined. Figure 7(D) shows the comparison of the values of the pattern width determined from ellipsometry measurements with the width of the mask used. For 100 μm -width, the size of the passivated thiol monolayer found is the same as the size of the mask used. For narrow lines (lower than 75 μm), the width of passivated thiol is larger than the width of the mask due to the light diffraction.

The average thickness of the allyl butyl ether added to the thiol monolayer ranges from 0.1 nm to 0.35 nm, which is consistent with the order of magnitude of the molecule size. This average thickness depends on the grafting density of thiol groups, i.e., the ratio of mercaptosilane to propylsilane grafted on the substrate. The effective thickness of allyl butyl ether is expected to be the highest when reacted on the densest thiol monolayer (obtained with 100% mercaptosilane). It is also expected to decrease with the grafting density of thiol groups. Actually, we found that the effective thickness of reacted allyl butyl ether is 0.23 nm for silanized substrates with 10% mercaptosilane and 0.35 nm for 100% mercaptosilane silanized substrates. This also qualitatively confirms that the grafting density of thiol groups increases with the ratio of mercaptosilane for silanization.

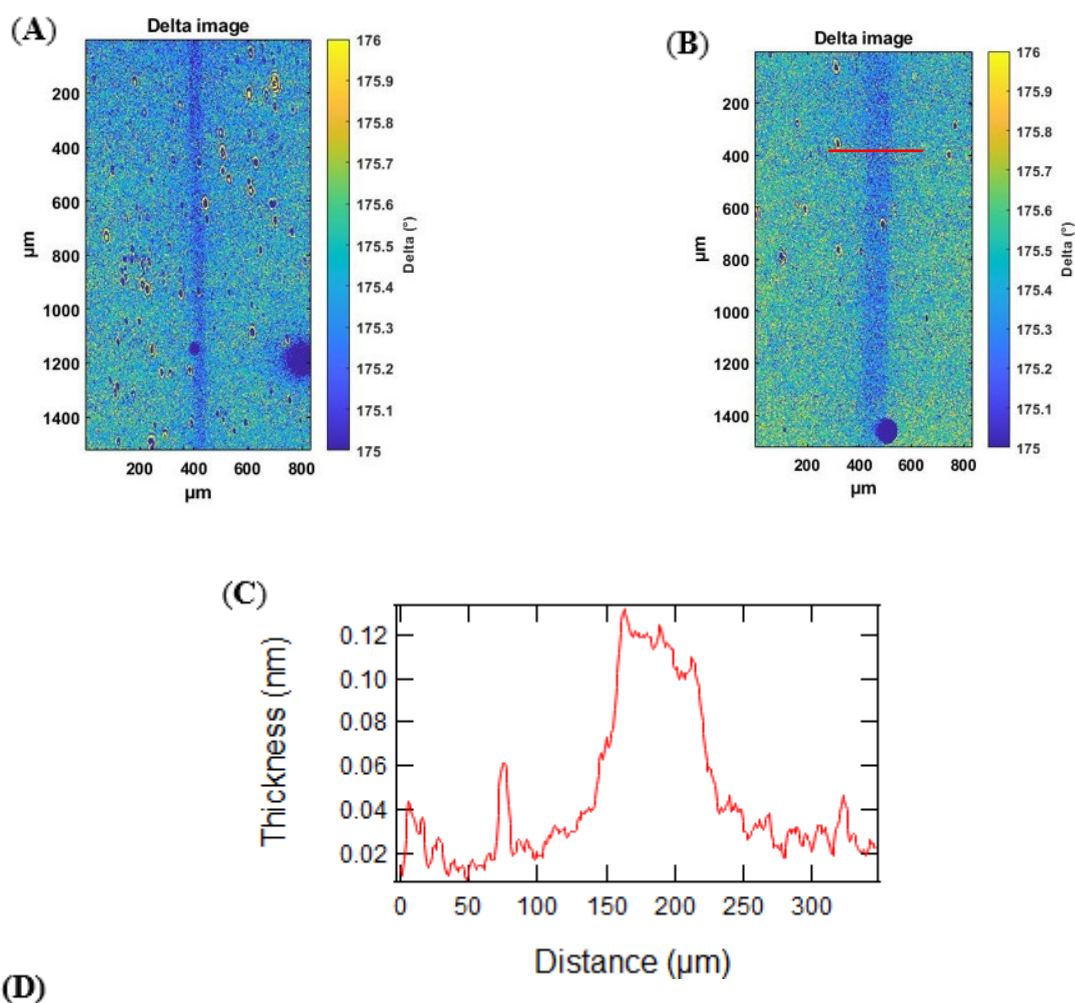


Figure 7. Mapping of Δ ellipsometric angle evidencing the selective passivation of thiol monolayer by allyl butyl ether using a line patterned mask of width (A) 5 μm and (B) 50 μm . (C) Thickness profile deduced from Δ ellipsometric angle mapping along a line perpendicular to the defect line from image (B). (D) Mask width and passivated line width as measured by ellipsometry. All the measurements are done on 100% mercapto silanized samples.

The distribution of passivated thiol by allyl butyl ether was also investigated by ToF-SIMS imaging. ToF-SIMS negative ion spectra are shown in Figure 8 for a patterned line width of 100 μm . The m/z of S^- and SH^- is used to check whether the distribution is uniform on the surface. The images clearly show a dark line of 100 μm -width. As darker zones correspond to

lesser intensity of S^- and SH^- the mapping allows to confirm that the grafted thiol group is passivated by allyl butyl ether in the area exposed to UV irradiation.

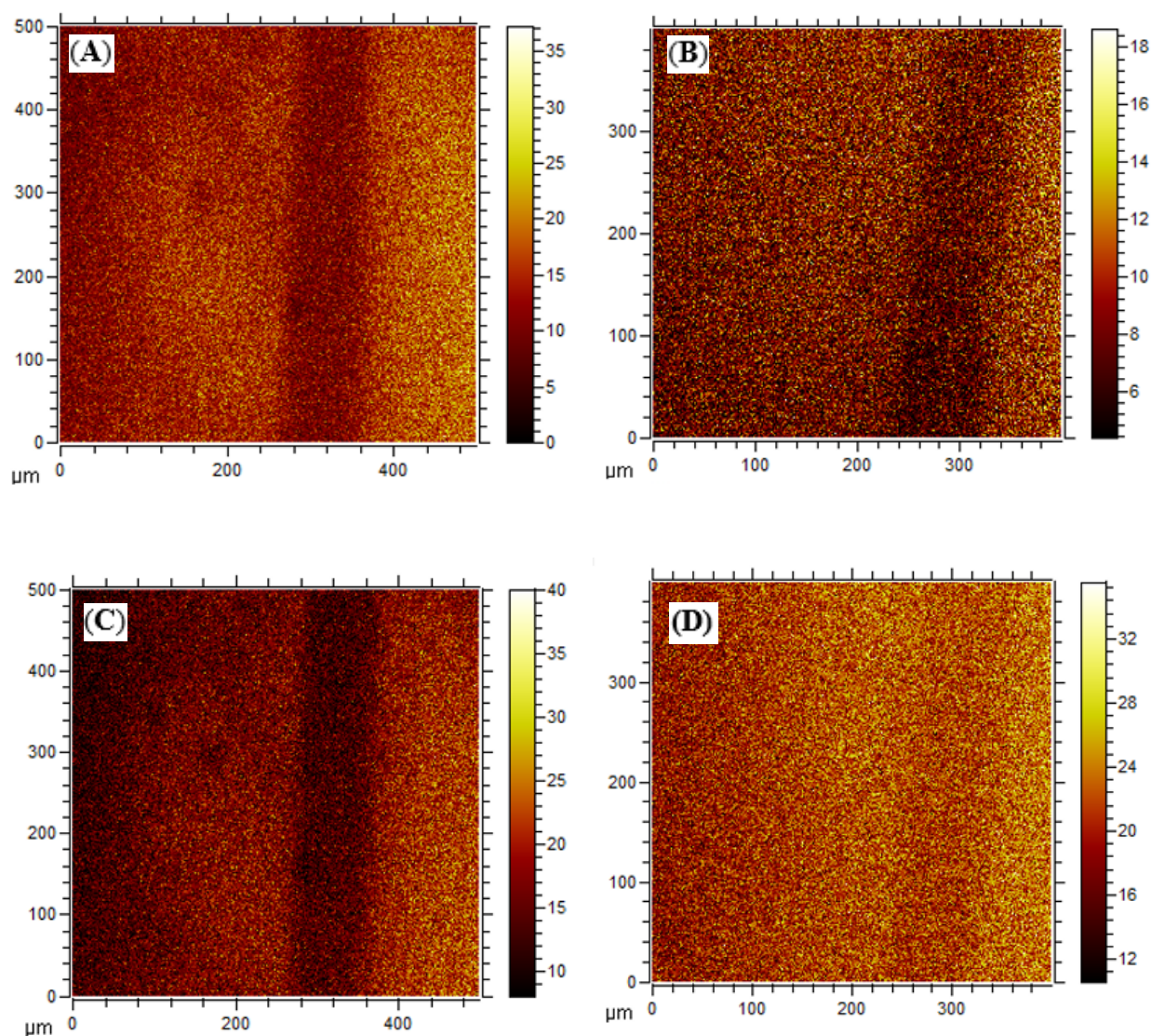


Figure 8. Representative negative ion TOF-SIMS mapping showing the distribution of SH^- (A, B) and S^- (C, D). The color bars correspond to the density of the atoms/molecules. Silicon wafers silanized with mercaptosilane 100% (A, C) and 50 % (B, D). The darker zones correspond to a lower density of SH^- And S^- ions, which is consistent with the lines for which thiol is passivated by allyl butyl ether. The pattern is obtained using a $100 \mu m$ -wide mask.

3.4. Swelling-induced wrinkles and delamination of surface-attached hydrogel films

The swollen thickness of hydrogel films underwater was measured using ellipsometry. In the Supporting Information S6, an example of IS and IC ellipsometric intensity spectra obtained with surface-attached PDMA hydrogel films in a dry state and swollen underwater is given.

The thickness is deduced from the three-layers model to fit experimental data. From the swollen and dry thickness, the volume fraction of polymer in the hydrogel layer can be deduced. It is equal to the ratio of the dry thickness to the swollen thickness.

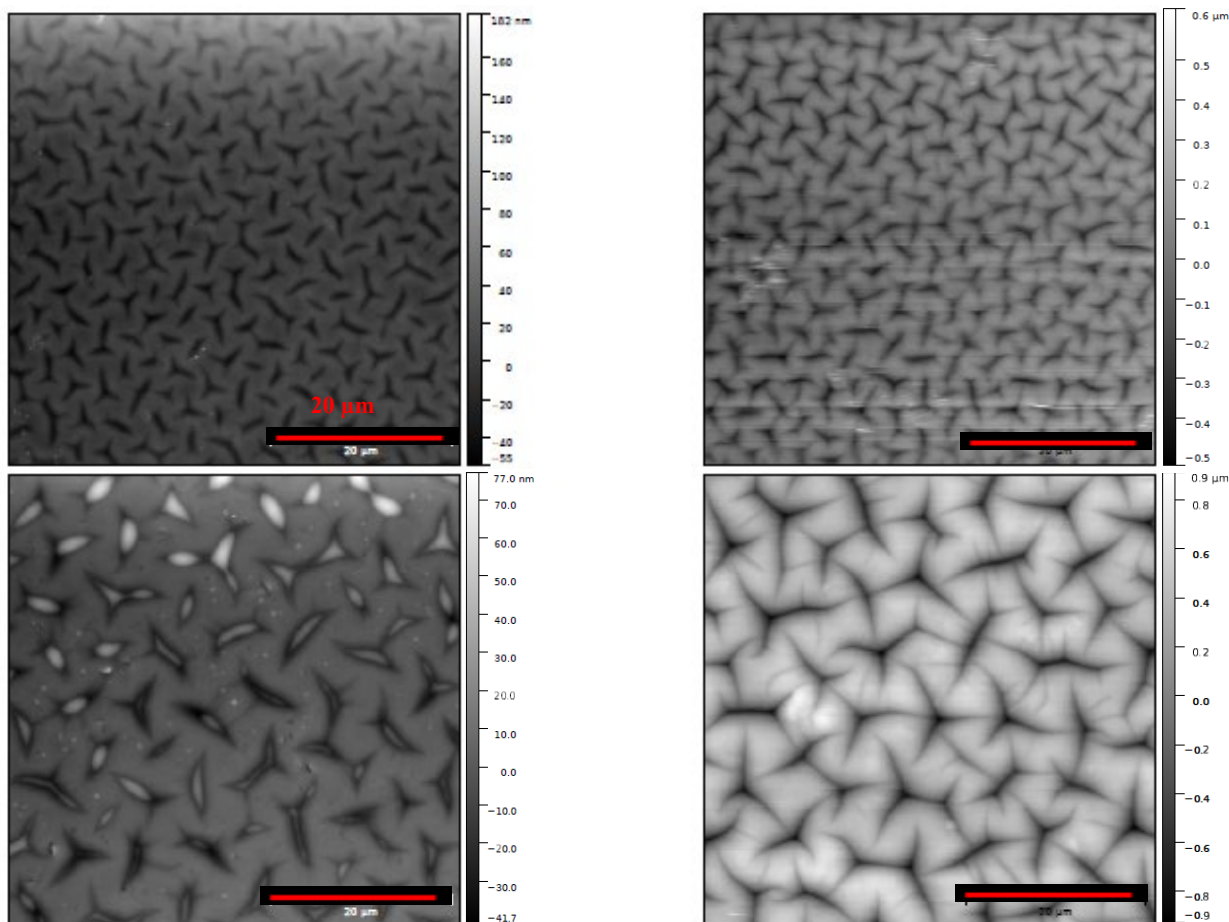


Figure 9. AFM images of the surface of substrate-attached PDMA hydrogel films in air and water. (Top) Hydrogel film in the air with a dry thickness of $1.2 \mu\text{m}$ (left image) and swollen thickness of $4.8 \mu\text{m}$ (right image). (Bottom) Hydrogel film in the air with a dry thickness of $2.6 \mu\text{m}$ (left image) and swollen thickness of $10.4 \mu\text{m}$ (right image).

All the investigated hydrogel films have dry thicknesses above 200 nm . The swelling ratio is always 2.7 ± 0.3 , whatever the dry thickness of the film. This is consistent with former results obtained with PNIPAM surface-attached hydrogel layers.²⁷ We found that the volume fraction of polymer or the swelling ratio is constant for hydrogel layers with dry thickness above around 100 nm . This can be explained by the gap between the grafting density and the cross-linking ratio. As the grafting on the surface is much denser than the cross-linking between chains, the effect of the surface grafting is more important for thin layers (below 100 nm) and is insignificant for thick layers (above 100 nm). The swelling of surface-attached hydrogel films

with various grafting densities was also investigated (Appendix A). We found that the swelling is similar for hydrogel films independently of the interface strength. As the hydrogel films are made by cross-linking and grafting ene-functionalized preformed chains with the same ratio of active alkene groups, they evidently have the same cross-linking density and swell the same.

Hydrogel films can exhibit instabilities or wrinkles on the surface, also called *sulci*, due to swelling. Indeed, being grafted on the surface of the substrate and having a very small thickness in front of the lateral dimension, the hydrogel films can only swell in the direction perpendicular to the substrate. However, the hydrogel film synthesis, which consists in cross-linking and grafting onto the surface, was performed in the dry state, so the swollen film is subject to compressive stresses in the direction parallel to the substrate. When these compressive stresses become greater than the buckling threshold of the elastic layer, they give rise to buckling instabilities that relax these stresses. First observed on gels by Tanaka et al.,¹⁶ the formation of these instabilities has since been described exhaustively in the literature. However, there is no unanimous opinion on the critical swelling at which these instabilities appear. It has indeed been noticed that highly cross-linked gel films may not wrinkle: the surface tension then focuses on the low compressive stresses obtained when the swelling is low.

The instabilities were characterized by AFM measurements in air and water. Hydrogel films with swelling less than or equal to two, did not exhibit instabilities. For films with swelling greater than 2, the wavelength of the instabilities present on their surface is proportional to the film thickness, which is also expected and has been observed in the literature. Figure 9 shows an example of instabilities observed by AFM on the surface of two PDMA films in air and water. At the same swelling ratio, a swollen hydrogel film with twice the dry thickness shows instabilities of the same morphology but of twice the wavelength.

In situations where the film is not strongly bound to the substrate, swelling stresses can alternately result in interface delamination followed by large-scale folding and blistering of the hydrogel films. Here, debonding mechanisms are promoted from the well-controlled line defects on the silicon substrate where the interface strength is reduced by the localized passivation of the reactive thiol groups grafted on the silicon substrate.

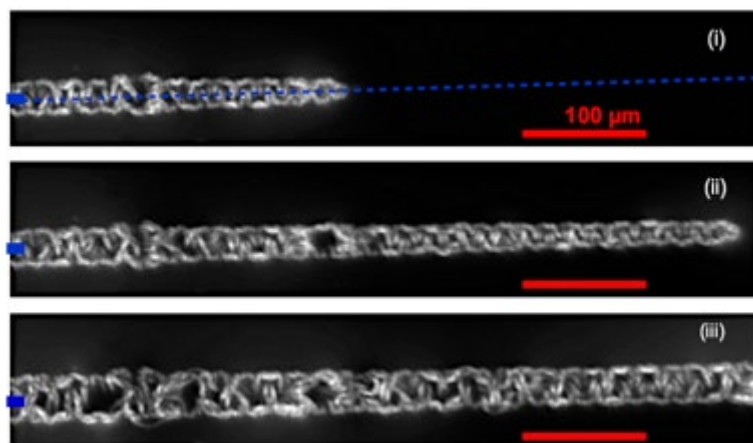


Figure 10: Magnified observation of the interface cracks at various stages shape of the debonding process of hydrogel film. The PDMA hydrogel film has the following characteristics: the dry thickness is 700 nm, and the width of the line defect is 9 μm . The images were taken at different times after exposure to humid air: 360 seconds (i), 420 seconds (ii), and 620 seconds (iii). The blue dotted lines indicate the orientation of the line defect, and the blue area on the left indicates the line defect width L_0 .

Figure 10 shows microscope observation of the interface cracks at various stages of the debonding process. The so-called “telephone-cord” debonding process is illustrated here for a hydrogel film of thickness h 700 nm and a line defect width of 9 μm , the images being taken at different times after exposure to humid air. Swelling-induced delamination propagates both along the passivated line defect and perpendicular to it, i.e. on areas where the hydrogel film is grafted on the substrate. The debonding and buckling mechanisms over the controlled line defects on the grafted hydrogel/substrate interface will be the subject of next chapter where the rate and the extent of debonding will be quantified as a function of film thickness, grafting density, and size of the defects.

4. Conclusion

We developed a platform of hydrogel coatings attached to the substrates with controlled thickness, swelling, and interface strength using a facile and versatile approach. Surface-attached poly(*N*, *N*-dimethylacrylamide) hydrogel films on silicon substrates were prepared using the CLAG approach. It consisted of simultaneous Cross-Linking And Grafting preformed and functionalized PDMA chains onto modified substrates by using thiol-ene click chemistry. Ene-functionalized PDMA linear chains were first synthesized with good control of the ene-functionalization ratio to rule the cross-linking density or the swelling of hydrogel in water. They were then coated onto thiol-modified substrates (with dithiol cross-linker) by a spin-

coating technique which allows the formation of hydrogel layers over a wide range of thickness from a few nanometers to several micrometers. The amount of thiol-monolayer grafted on the substrate could be finely adjusted to vary the interface strength between the substrate and the hydrogel film. This was achieved by mixing reactive mercaptosilane with passive propylsilane in the liquid phase silanization. Combining XPS and ToF-SIMS techniques, we were able to determine the grafting density of thiol varying from 0.1 to 0.6 nm⁻². The substrate/hydrogel interface strength was also tuned locally by patterning local defects. This was achieved by locally passivated thiol with ene-molecule (before the polymer coating) by activating thiol-ene reaction with UV-irradiation on selected places through micrometric resolution masks. The efficiency of the formation of line defects was evidenced by ellipsometry and ToF-SIMS images, their width ranging from 9 to 100 micrometers. When swelling in water, the surface of the adhering hydrogel film could exhibit instabilities or wrinkles due to compressive stresses in the lateral plane, which wavelength increases with the thickness and the swelling ratio of the hydrogel. We also showed that the patterned line defects with low adhesion were efficient in promoting film delamination from the substrate under the action of swelling stresses with large-scale folding and blistering of the hydrogel. The associated debonding mechanisms will be studied in detail in the next chapter in relation to the interface physical chemistry.

5. References

- (1) Grube, S.; Siegmann, K.; Hirayama, M. A Moisture-Absorbing and Abrasion-Resistant Transparent Coating on Polystyrene. *J Coat Technol Res* **2015**, 12 (4), 669–680. <https://doi.org/10.1007/s11998-015-9678-z>.
- (2) Chevallier, P.; Turgeon, S.; Sarra-Bournet, C.; Turcotte, R.; Laroche, G. Characterization of Multilayer Anti-Fog Coatings. *ACS Appl. Mater. Interfaces* **2011**, 3 (3), 750–758. <https://doi.org/10.1021/am1010964>.
- (3) Shibraen, M. H. M. A.; Yagoub, H.; Zhang, X.; Xu, J.; Yang, S. Anti-Fogging and Anti-Frosting Behaviors of Layer-by-Layer Assembled Cellulose Derivative Thin Film. *Applied Surface Science* **2016**, C (370), 1–5. <https://doi.org/10.1016/j.apsusc.2016.02.060>.
- (4) Park, S.; Park, S.; Jang, D. H.; Lee, H. S.; Park, C. H. Anti-Fogging Behavior of Water-Absorbing Polymer Films Derived from Isosorbide-Based Epoxy Resin. *Materials Letters* **2016**, C (180), 81–84. <https://doi.org/10.1016/j.matlet.2016.05.114>.
- (5) Lee, K. Y.; Mooney, D. J. Hydrogels for Tissue Engineering. *Chem. Rev.* **2001**, 101 (7), 1869–1880. <https://doi.org/10.1021/cr000108x>.
- (6) Li, J.; Celiz, A. D.; Yang, J.; Yang, Q.; Wamala, I.; Whyte, W.; Seo, B. R.; Vasilyev, N. V.; Vlassak, J. J.; Suo, Z.; Mooney, D. J. Tough Adhesives for Diverse Wet Surfaces. *Science* **2017**, 357 (6349), 378–381. <https://doi.org/10.1126/science.aah6362>.
- (7) Boateng, J. S.; Matthews, K. H.; Stevens, H. N. E.; Eccleston, G. M. Wound Healing Dressings and Drug Delivery Systems: A Review. *Journal of Pharmaceutical Sciences* **2008**, 97 (8), 2892–2923. <https://doi.org/10.1002/jps.21210>.
- (8) Fram, D. B.; Aretz, T.; Azrin, M. A.; Mitchel, J. F.; Samady, H.; Gillam, L. D.; Sahatjian, R.; Waters, D.; McKay, R. G. Localized Intramural Drug Delivery during Balloon Angioplasty Using Hydrogel-Coated Balloons and Pressure-Augmented Diffusion. *Journal of the American College of Cardiology* **1994**, 23 (7), 1570–1577. [https://doi.org/10.1016/0735-1097\(94\)90658-0](https://doi.org/10.1016/0735-1097(94)90658-0).

- (9) Kopecek, J. Hydrogels: From Soft Contact Lenses and Implants to Self-Assembled Nanomaterials. *Journal of Polymer Science Part A: Polymer Chemistry* **2009**, 47 (22), 5929–5946. <https://doi.org/10.1002/pola.23607>.
- (10) Li, J.; Mooney, D. J. Designing Hydrogels for Controlled Drug Delivery. *Nat Rev Mater* **2016**, 1 (12), 1–17. <https://doi.org/10.1038/natrevmats.2016.71>.
- (11) Chaudhury, M. K.; Chakrabarti, A.; Ghatak, A. Adhesion-Induced Instabilities and Pattern Formation in Thin Films of Elastomers and Gels. *Eur. Phys. J. E* **2015**, 38 (7), 82. <https://doi.org/10.1140/epje/i2015-15082-7>.
- (12) Gille, G.; Rau, B. Buckling Instability and Adhesion of Carbon Layers. *Thin Solid Films* **1984**, 120 (2), 109–121. [https://doi.org/10.1016/0040-6090\(84\)90365-1](https://doi.org/10.1016/0040-6090(84)90365-1).
- (13) Trujillo, V.; Kim, J.; Hayward, R. C. Creasing Instability of Surface-Attached Hydrogels. *Soft Matter* **2008**, 4 (3), 564–569. <https://doi.org/10.1039/B713263H>.
- (14) Wang, Z.; Tonderys, D.; Leggett, S. E.; Williams, E. K.; Kiani, M. T.; Steinberg, R. S.; Qiu, Y.; Wong, I. Y.; Hurt, R. H. Wrinkled, Wavelength-Tunable Graphene-Based Surface Topographies for Directing Cell Alignment and Morphology. *Carbon N Y* **2016**, 97, 14–24. <https://doi.org/10.1016/j.carbon.2015.03.040>.
- (15) Mora, T.; Boudaoud, A. Buckling of Swelling Gels. *European Physical Journal E: Soft matter and biological physics* **2006**, 20, 119. <https://doi.org/10.1140/epje/i2005-10124-5>.
- (16) Tanaka, T.; Sun, S.-T.; Hirokawa, Y.; Katayama, S.; Kucera, J.; Hirose, Y.; Amiya, T. Mechanical Instability of Gels at the Phase Transition. *Nature* **1987**, 325 (6107), 796–798. <https://doi.org/10.1038/325796a0>.
- (17) Delavoipière, J.; Tran, Y.; Verneuil, E.; Chateauinois, A. Poroelastic Indentation of Mechanically Confined Hydrogel Layers. *Soft Matter* **2016**, 12 (38), 8049–8058. <https://doi.org/10.1039/C6SM01448H>.
- (18) Takahashi, R.; Miyazako, H.; Tanaka, A.; Ueno, Y. Dynamic Creation of 3D Hydrogel Architectures via Selective Swelling Programmed by Interfacial Bonding. *ACS Appl. Mater. Interfaces* **2019**, 11 (31), 28267–28277. <https://doi.org/10.1021/acsami.9b05552>.

- (19) Xu, S.; Yan, Z.; Jang, K.-I.; Huang, W.; Fu, H.; Kim, J.; Wei, Z.; Flavin, M.; McCracken, J.; Wang, R.; Badea, A.; Liu, Y.; Xiao, D.; Zhou, G.; Lee, J.; Chung, H. U.; Cheng, H.; Ren, W.; Banks, A.; Li, X.; Paik, U.; Nuzzo, R. G.; Huang, Y.; Zhang, Y.; Rogers, J. A. Assembly of Micro/Nanomaterials into Complex, Three-Dimensional Architectures by Compressive Buckling. *Science* **2015**, 347 (6218), 154–159. <https://doi.org/10.1126/science.1260960>.
- (20) Genzer, J.; Groenewold, J. Soft Matter with Hard Skin: From Skin Wrinkles to Templating and Material Characterization. *Soft Matter* **2006**, 2 (4), 310–323. <https://doi.org/10.1039/B516741H>.
- (21) Auguste, A.; Yang, J.; Jin, L.; Chen, D.; Suo, Z.; Hayward, R. C. Formation of High Aspect Ratio Wrinkles and Ridges on Elastic Bilayers with Small Thickness Contrast. *Soft Matter* **2018**, 14 (42), 8545–8551. <https://doi.org/10.1039/C8SM01345D>.
- (22) Wang, Q.; Zhao, X. A Three-Dimensional Phase Diagram of Growth-Induced Surface Instabilities. *Sci Rep* **2015**, 5 (1), 8887. <https://doi.org/10.1038/srep08887>.
- (23) Delavoipière, J.; Heurtefeu, B.; Teisseire, J.; Chateauinois, A.; Tran, Y.; Fermigier, M.; Verneuil, E. Swelling Dynamics of Surface-Attached Hydrogel Thin Films in Vapor Flows. *Langmuir* **2018**, 34 (50), 15238–15244. <https://doi.org/10.1021/acs.langmuir.8b03206>.
- (24) Delavoipière, J.; Tran, Y.; Verneuil, E.; Heurtefeu, B.; Hui, C. Y.; Chateauinois, A. Friction of Poroelastic Contacts with Thin Hydrogel Films. *Langmuir* **2018**, 34 (33), 9617–9626. <https://doi.org/10.1021/acs.langmuir.8b01466>.
- (25) Koc, J.; Schönemann, E.; Amuthalingam, A.; Clarke, J.; Finlay, J. A.; Clare, A. S.; Laschewsky, A.; Rosenhahn, A. Low-Fouling Thin Hydrogel Coatings Made of Photo-Cross-Linked Polyzwitterions. *Langmuir* **2019**, 35 (5), 1552–1562. <https://doi.org/10.1021/acs.langmuir.8b02799>.
- (26) Chollet, B.; Li, M.; Martwong, E.; Bresson, B.; Fretigny, C.; Tabeling, P.; Tran, Y. Multiscale Surface-Attached Hydrogel Thin Films with Tailored Architecture. *ACS Appl. Mater. Interfaces* **2016**, 8 (18), 11729–11738. <https://doi.org/10.1021/acsami.6b00446>.

- (27) Chollet, B.; D'Eramo, L.; Martwong, E.; Li, M.; Macron, J.; Mai, T. Q.; Tabeling, P.; Tran, Y. Tailoring Patterns of Surface-Attached Multiresponsive Polymer Networks. *ACS Appl. Mater. Interfaces* **2016**, 8 (37), 24870–24879. <https://doi.org/10.1021/acsami.6b07189>.
- (28) Hoyle, C. E.; Lee, T. Y.; Roper, T. Thiol–Enes: Chemistry of the Past with Promise for the Future. *Journal of Polymer Science Part A: Polymer Chemistry* **2004**, 42 (21), 5301–5338. <https://doi.org/10.1002/pola.20366>.
- (29) Kassahun, G. S.; Griveau, S.; Juillard, S.; Champavert, J.; Ringuedé, A.; Bresson, B.; Tran, Y.; Bedioui, F.; Slim, C. Hydrogel Matrix-Grafted Impedimetric Aptasensors for the Detection of Diclofenac. *Langmuir* **2020**, 36 (4), 827–836. <https://doi.org/10.1021/acs.langmuir.9b02031>.
- (30) Li, M.; Bresson, B.; Cousin, F.; Fretigny, C.; Tran, Y. Submicrometric Films of Surface-Attached Polymer Network with Temperature-Responsive Properties. *Langmuir* **2015**, 31 (42), 11516–11524. <https://doi.org/10.1021/acs.langmuir.5b02948>.
- (31) Bullett, N. A.; Talib, R. A.; Short, R. D.; McArthur, S. L.; Shard, A. G. Chemical and Thermo-Responsive Characterisation of Surfaces Formed by Plasma Polymerisation of N-Isopropyl Acrylamide. *Surface and Interface Analysis* **2006**, 38 (7), 1109–1116. <https://doi.org/10.1002/sia.2318>.
- (32) D'Eramo, L.; Chollet, B.; Leman, M.; Martwong, E.; Li, M.; Geisler, H.; Dupire, J.; Kerdraon, M.; Vergne, C.; Monti, F.; Tran, Y.; Tabeling, P. Microfluidic Actuators Based on Temperature-Responsive Hydrogels. *Microsyst Nanoeng* **2018**, 4 (1), 1–7. <https://doi.org/10.1038/micronano.2017.69>.
- (33) Martwong, E.; Tran, Y. Lower Critical Solution Temperature Phase Transition of Poly(PEGMA) Hydrogel Thin Films. *Langmuir* **2021**, [acs.langmuir.1c01165](https://doi.org/10.1021/acs.langmuir.1c01165). <https://doi.org/10.1021/acs.langmuir.1c01165>.
- (34) Meyerhofer, D. Characteristics of Resist Films Produced by Spinning. *Journal of Applied Physics* **1978**, 49 (7), 3993–3997. <https://doi.org/10.1063/1.325357>.

- (35) Norrman, K.; Ghanbari-Siahkali, A.; B. Larsen, N. 6 Studies of Spin-Coated Polymer Films. Annual Reports Section “C” (Physical Chemistry) **2005**, 101 (0), 174–201. <https://doi.org/10.1039/B408857N>.
- (36) Hall, D. B.; Underhill, P.; Torkelson, J. M. Spin Coating of Thin and Ultrathin Polymer Films. Polymer Engineering and Science **1998**, 38 (12), 2039–2045. <https://doi.org/10.1002/pen.10373>.
- (37) Extrand, C. W. Spin Coating of Very Thin Polymer Films. Polymer Engineering & Science **1994**, 34 (5), 390–394. <https://doi.org/10.1002/pen.760340503>.
- (38) Handbook of Polymer Synthesis, Characterization, and Processing: Saldívar-Guerra/Handbook of Polymer Synthesis, Characterization, and Processing; Saldívar-Guerra, E., Vivaldo-Lima, E., Eds.; John Wiley & Sons, Inc.: Hoboken, NJ, USA, 2013. <https://doi.org/10.1002/9781118480793>.
- (39) Wagner, H. L. The Mark–Houwink–Sakurada Equation for the Viscosity of Atactic Polystyrene. Journal of Physical and Chemical Reference Data **1985**, 14 (4), 1101–1106. <https://doi.org/10.1063/1.555740>.
- (40) Flory, P. J. Principles of Polymer Chemistry; 1953.
- (41) Bramblett, A. L.; S. Boeckl, M.; Hauch, K. D.; Ratner, B. D.; Sasaki, T.; Rogers, J. W. Determination of Surface Coverage for Tetraphenylporphyrin Monolayers Using Ultraviolet Visible Absorption and X-Ray Photoelectron Spectroscopies. Surf. Interface Anal. **2002**, 33 (6), 506–515. <https://doi.org/10.1002/sia.1239>.
- (42) Shircliff, R. A.; Martin, I. T.; Pankow, J. W.; Fennell, J.; Stradins, P.; Ghirardi, M. L.; Cowley, S. W.; Branz, H. M. High-Resolution X-Ray Photoelectron Spectroscopy of Mixed Silane Monolayers for DNA Attachment. ACS Appl. Mater. Interfaces **2011**, 3 (9), 3285–3292. <https://doi.org/10.1021/am200604q>.
- (43) Zhuravlev, L. T. Concentration of Hydroxyl Groups on the Surface of Amorphous Silicas. Langmuir **1987**, 3 (3), 316–318. <https://doi.org/10.1021/la00075a004>.

6. Supporting Information

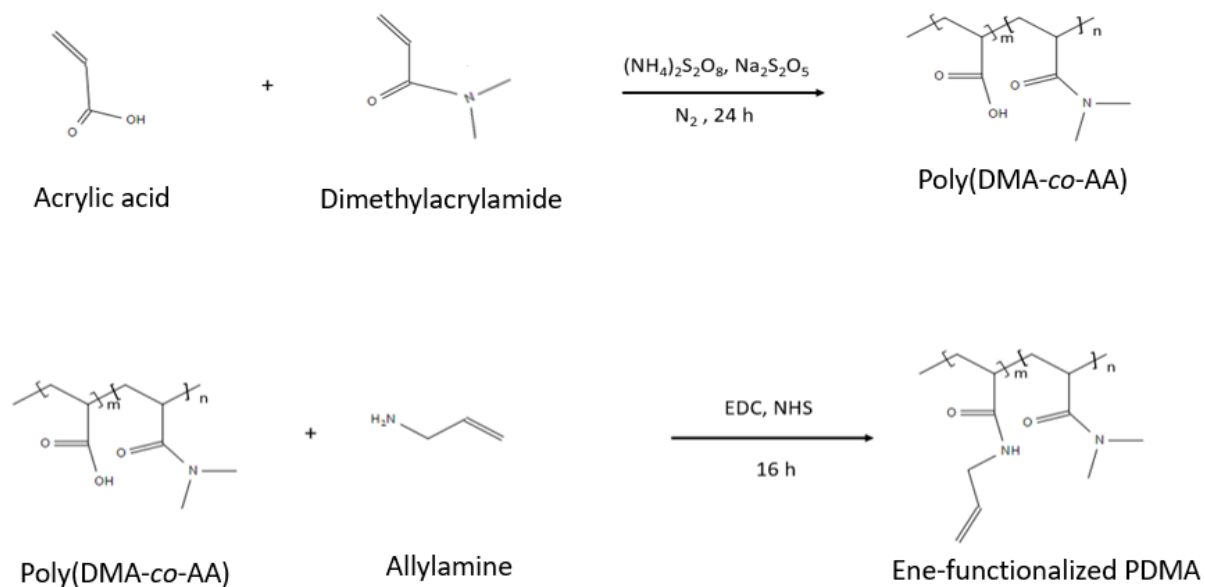


Figure S1: Synthesis of ene-functionalized PDMA polymers using two-step free radical polymerization. First, poly(DMA-co-AA) copolymer is synthesized by free radical polymerization in water using ammonium persulfate/sodium metabisulfite redox couple as initiator. Then poly(DMA-co-AA) is functionalized using allylamine with EDC/NHS coupling at room temperature for 16 h.

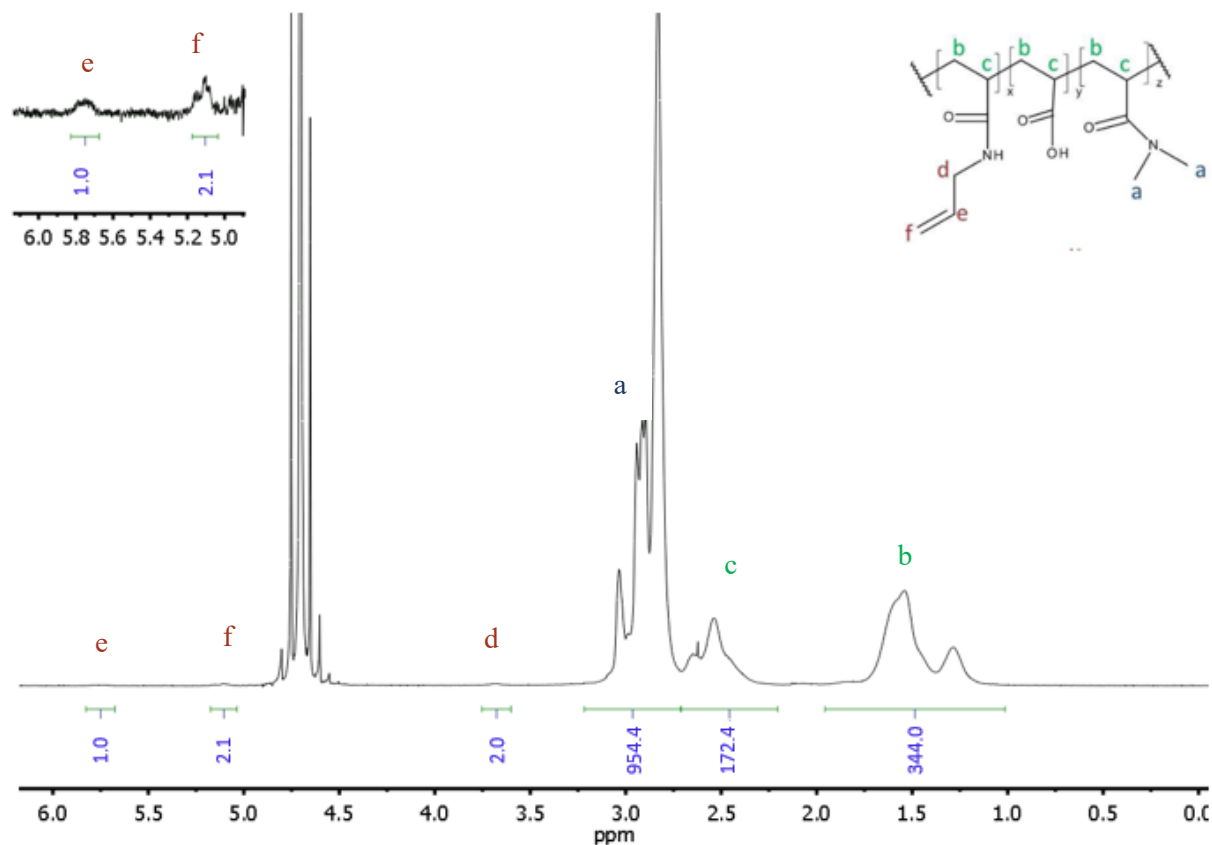


Figure S2. ^1H NMR spectrum of ene-functionalized poly(DMA-*co*-AA) polymer in D_2O .

The 1.0-1.8 ppm peak is the CH_2 group in the copolymer, which is mentioned as b in the figure S2. And the peak of 2.2 to 3.2 ppm corresponds to the methyl group, which is mentioned as a, and the CH group, which is represented as c. The peaks at 5.0 and 5.8 correspond to the ene-groups in the polymer, which are represented as e and f. The percentage of the ene group in the polymer can be calculated by comparing the integral of the peaks. For ene-functionalized poly(DMA-*co*-AA), the ratio of ene-reactive groups is deduced from the ratio between the average the integral of one proton (e) or two protons (f) group of allylamine and the integral of two proton (b) or seven protons (a and c) of poly(dimethylacrylamide). The percentage of the ene-group present in the ene-functionalized poly(DMA-*co*-AA) is $0.6 \pm 1\%$.

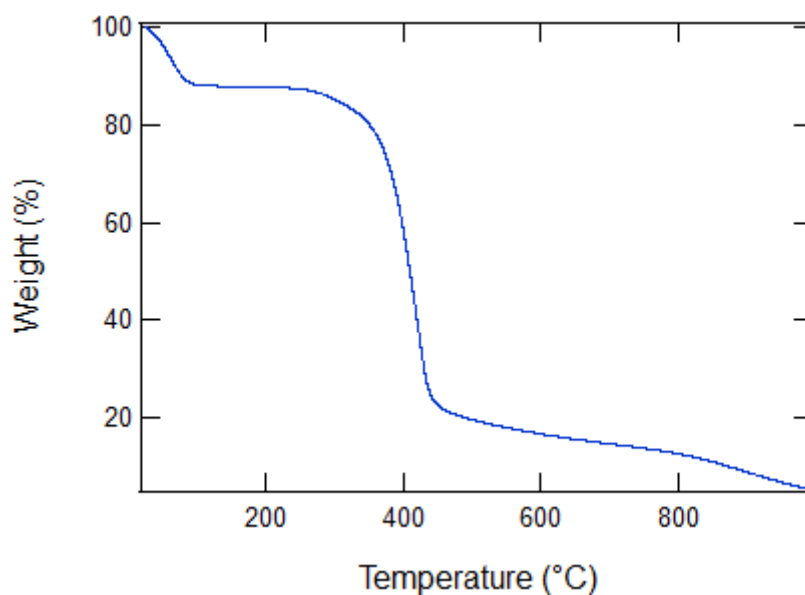


Figure S3. Thermal gravimetric analysis (TGA) curve for PDMA

Figure S3 shows the Thermal gravimetric analysis (TGA) of the PDMA. This gives the temperature at which the degradation of the polymer starts. There is 12.4% of water present in the polymer, which is the first decrease in the weight. It can be seen from figure S3 that the polymer starts degradation after 250 °C. This means that the polymer is stable below 250 °C. In our experiments, we heat at 150 °C to activate the thiol-ene reaction in order to crosslink and graft hydrogel to the substrate. The activation of the thiol-ene reaction is performed at a temperature well below the temperature of polymer degradation.

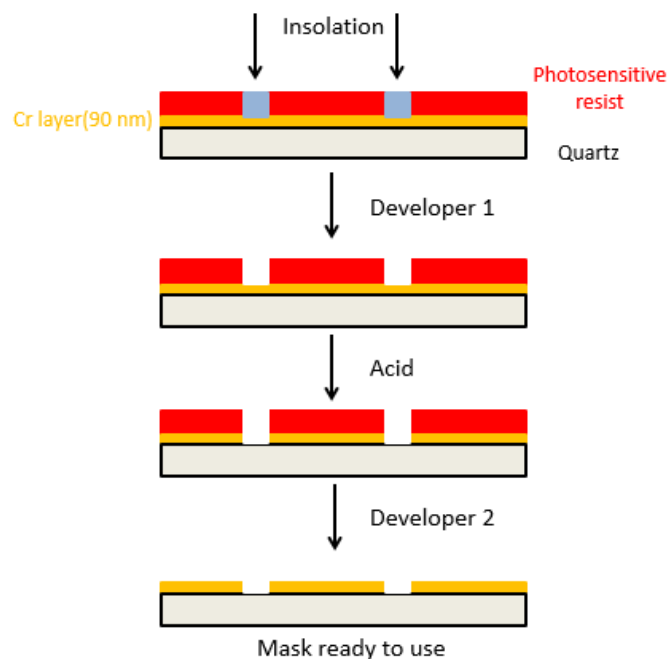


Figure S4. Preparation of the mask for the photolithography. A quartz mask with a 90 nm layer of chromium is coated with a photoresist. The pattern for the defects was then drawn using Clewin Software. Then the laser is exposing only to the patterned area. After the patterning, the mask is washed using an AZ 351 B developer. During the bath in the developer, only the exposed resin is removed, which reveals the bare chromium layer underneath the photoresist. Then the exposed chromium layer is etched in an acid bath. The remaining photoresist from the rest of the area is removed by using acetone.

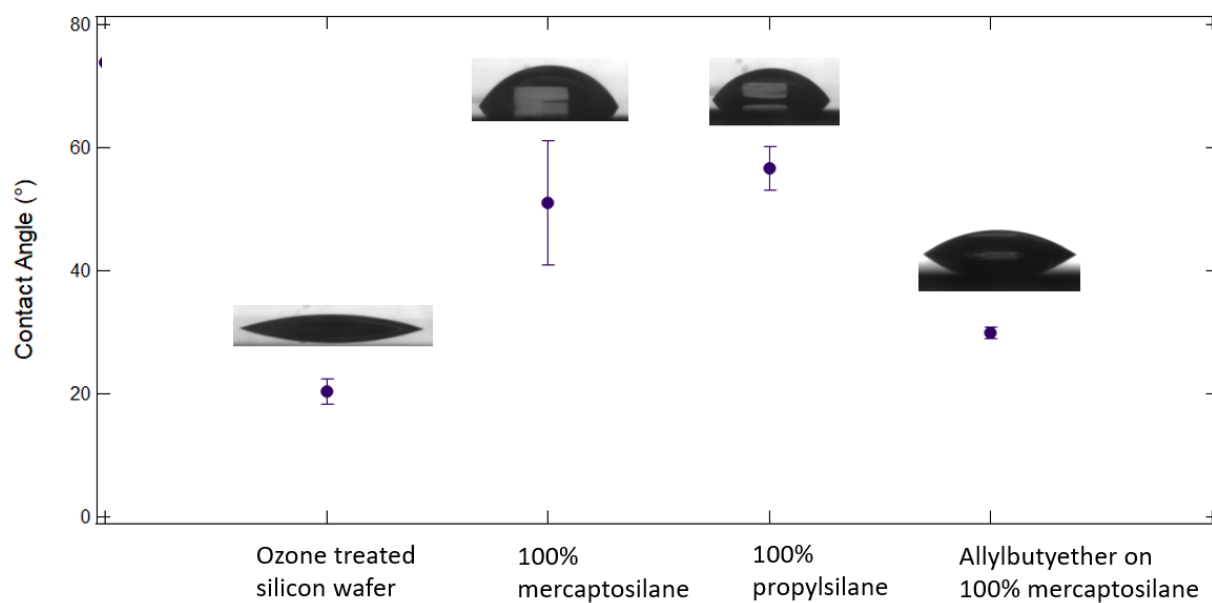


Figure S5. Contact angle measured for ozone-treated silicon wafer and silanized substrates using 100 % mercapto silane, 100 % propyl silane, and reacted allyl butyl ether.

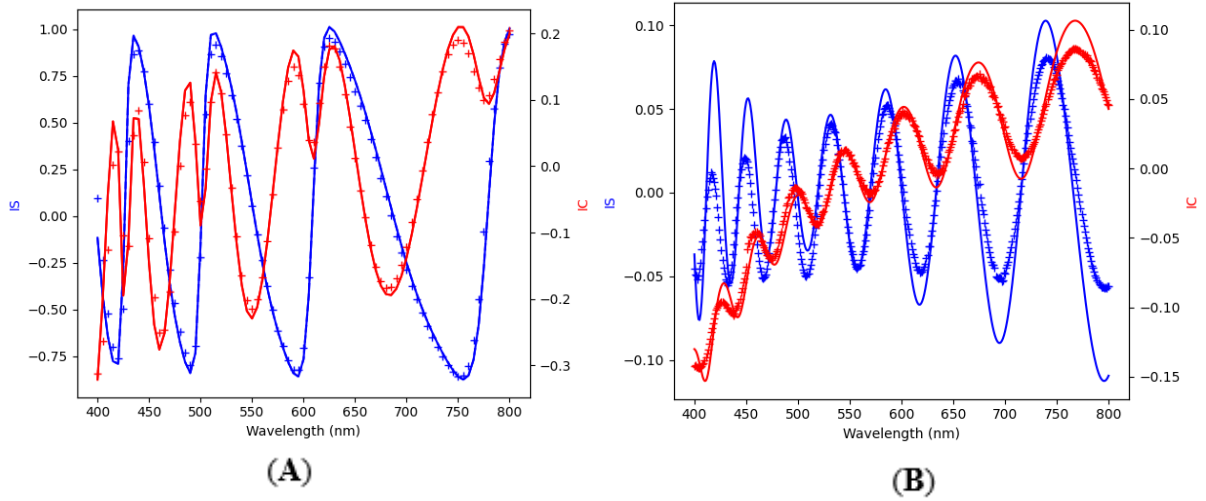


Figure S6. Spectra IS, and IC are the functions of ellipsometric angles delta (Δ) and psi (ψ), where

$$IS = \sin(2\psi) * \sin(\Delta) \quad \text{Eq. S1}$$

$$IC = \sin(2\psi) * \cos(\Delta) \quad \text{Eq. S2}$$

IS and IC of surface-attached PDMA hydrogel films as a function of wavelength for the dry state **(A)** and swollen underwater **(B)**. Data are fitted to a one-layer model (dry), and a two-layer model (details in appendix) for swollen hydrogel as shown with the best fit (solid line) of the experimental data is shown for IS (in blue) and IC (in red). The dry thickness of the hydrogel film is 1100 nm from **(A)**. The swollen thickness of the hydrogel layer is 3450 nm from **(B)**. The swelling ratio is 3.13. The upper layer thickness is 160 nm, and the upper layer swelling ratio is 6.66.

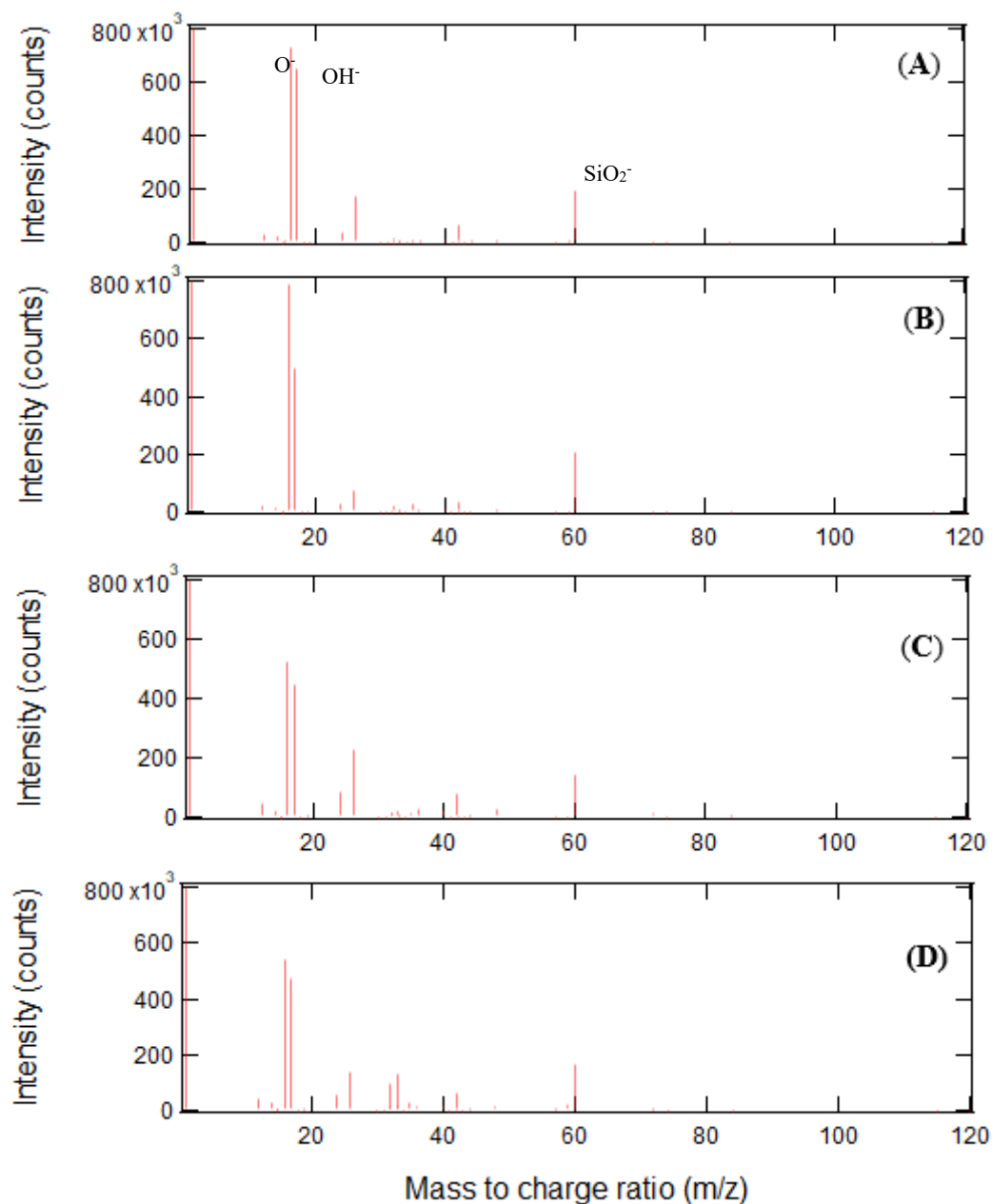


Figure S7. Negative secondary ion mass spectra for m/z from 0 to 120 for silicon wafer with bare (A), 0% (B), 10% (C), and 100% mercapto silane-modified (D). The intensity of O^- , OH^- , and SiO_2^- are depicted in (A), (B), (C), and (D).

3. Swelling-induced delamination of hydrogel/substrate interfaces

RÉSUMÉ

Le décollement du film induit par le gonflement est réalisé sous un flux de vapeur constant assurant la saturation du film en eau. En observant le décollement progressif du film à partir des défauts linéaires préexistants, nous retrouvons un motif d'instabilité classique dit de fil de téléphone et nous montrons que le décollement résulte de contraintes de gonflement localisées proche de la ligne de décollement. Nous mesurons la vitesse de propagation du décollement dans la zone où le film est greffé sur le substrat et nous observons qu'elle augmente de deux ordres de grandeur lorsque la quantité de propylsilane dans le mélange de silanes réactifs passe de 25 à 100 %, c'est-à-dire lorsque le taux de greffage du film décroît. Un seuil d'épaisseur pour le décollement est également observé, les films pouvant se décoller étant d'autant plus minces que le taux de greffage du film est faible. Les mesures de ce seuil sont discutées à partir d'un modèle non linéaire de mécanique de la rupture qui décrit le système à l'équilibre de gonflement. En l'absence de phénomènes de transport d'eau en front de fissure, les valeurs seuils d'énergie à rupture déduites de ce modèle sont compatibles avec une estimation de l'énergie requise pour rompre les liaisons covalentes à l'interface film/substrat.

Table of contents

| | |
|--|-----|
| 1. Introduction..... | 81 |
| 2. Swelling equilibrium of hydrogel networks | 81 |
| 2.1. Deformation free energy..... | 82 |
| 2.2. Swelling equilibrium | 84 |
| 2.2.1. Isotropic swelling | 84 |
| 2.2.2. Swelling of hydrogel film attached to a rigid substrate | 85 |
| 2.2.3. Plane strain swelling of a thin film..... | 85 |
| 2.3. Swelling stresses..... | 86 |
| 2.4. Discussion..... | 87 |
| 3. Experimental setup..... | 88 |
| 4. Overview of debonding mechanisms..... | 90 |
| 4.1. Phone cord debonding mechanisms | 90 |
| 4.2. Dendritic delamination patterns..... | 94 |
| 4.3. Phase diagram for debonding mechanisms | 95 |
| 5. Debonding in the phone cord regime..... | 96 |
| 5.1. Measurement of the debonding velocity | 96 |
| 5.2. Relevance of buckling stresses to delamination mechanisms | 97 |
| 5.3. Dependence of transverse velocity on time..... | 99 |
| 5.4. Threshold thickness for the occurrence of debonding..... | 104 |
| 6. Theoretical crack model..... | 106 |
| 7. Discussion..... | 108 |
| 8. Conclusion | 110 |
| 9. References..... | 110 |

1. Introduction

In this chapter, we investigate the interface debonding mechanisms of the grafted PDMA hydrogel films under investigation when they are fully swollen with water. Using the methodology developed in the previous chapter, delamination is induced from well-controlled interface defects with low adhesion. We will show that debonding results from localized differential stresses which arise from the release of some of the geometrical constraints applied to the film when it moves from a bounded to an unbounded state. The role of the grafting density on the initiation and growth of interface cracks is especially addressed in the light of a fracture mechanics description of swelling-induced delamination of the hydrogel films.

In the first section, we will briefly recall the main theoretical approaches to the swelling equilibrium of hydrogel networks with an emphasis on the role of geometrical constraints and on the swelling stresses which are induced within the films. Then, we will describe debonding mechanisms as a function of film thickness, swelling ratio, and grafting density. From systematic measurements of the debonding velocity, the existence of a thickness threshold for the occurrence of debonding is especially evidenced. Thanks to a theoretical fracture mechanics description of the interface cracks, this threshold provides an estimate of the fracture energy of the interface, which will be discussed as a function of the grafting density.

2. Swelling equilibrium of hydrogel networks

In what follows, we briefly recall the thermodynamics approach to the swelling equilibrium of hydrogel networks. This topic has a long history starting from the seminal work of Flory and Rehner in the 40's¹⁻⁶. The starting point is the Flory-Huggins theory of polymer solutions⁷ which applies only when the polymer is not crosslinked. In a crosslinked polymer, the presence of an interconnected network precludes the possibility of complete dissolution. For such a material, the Flory-Huggins equation is therefore not in itself sufficient to give the free energy of dilution; it is necessary to take into account also the configurational entropy of the network. Accordingly, the swelling equilibrium is then expressed from a balance between the free energy of dilution for the polymer in the state prior to crosslinking and the change of free energy due to the associated elastic expansion of the network. This forms the basis of the Flory-Rehner model¹⁻³, which is outlined below.

2.1. Deformation free energy

From a thermodynamics point of view, the free energy of a polymer network swollen by a solvent can be expressed as the sum of two contributions: one is the free energy of mixing, f_{mix} , and the second one is the free energy f_{ela} associated with the stretching of the polymer chains of the polymer network.⁴ Accordingly, the free energy density (the free energy per unit volume) of a swollen polymer network, *i.e.*, the energy needed to mix the polymer and the solvent, is expressed as

$$f(\lambda_i) = f_{ela}(\lambda_i) + f_{mix}(\lambda_i) \quad \text{Eq. 1}$$

Where λ_i are the stretch ratios in the principal directions.

The elastic energy term f_{ela} has the same origin as that of a stretched rubber, where this contribution is of an essentially entropic nature. Here, we take for the free elastic energy

$$f_{ela}(\lambda_i) = \frac{G_0}{2} (\lambda_1^2 + \lambda_2^2 + \lambda_3^2 - 3 - 2 \ln \lambda_1 \lambda_2 \lambda_3) \quad \text{Eq. 2}$$

Where G_0 is the shear modulus of the gel *in the reference (drained) state*. In the above expression, the logarithm term accounts for swelling.^{8,9} For an incompressible rubber, this term will be vanishing as $\lambda_1 = \lambda_2 = \lambda_3 = 1$.

The free energy of mixing f_{mix} can be derived from the thermodynamics of polymer solutions. When a dry gel network with a volume V_0 is immersed in a solvent (as shown in Figure 1), its polymer volume fraction changes from 1 in the reference state (taken here as the dry state) to its equilibrium value ϕ_p in the current, swollen, state with

$$\phi_p = \frac{1}{\lambda_1 \lambda_2 \lambda_3} \quad \text{Eq. 3}$$

The volume of solvent absorbed by the polymer network is $(\lambda_1 \lambda_2 \lambda_3 - 1)V_0$, and the volume of the swollen polymer is $(\lambda_1 \lambda_2 \lambda_3)V_0$. The change in the free energy density during this operation is thus given by

$$V_0 f_{mix}(\lambda_i) = \lambda_1 \lambda_2 \lambda_3 f_{sol}(\phi_p) - (\lambda_1 \lambda_2 \lambda_3 - 1) V_0 f_{sol}(0) \quad \text{Eq. 4}$$

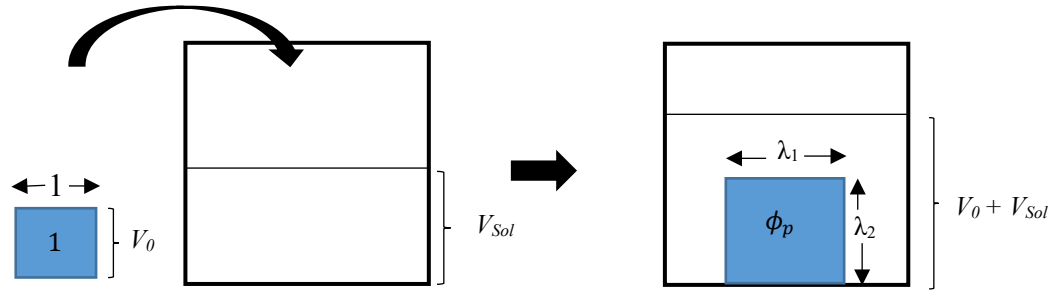


Figure 1: Definition of the deformation free energy density for a gel. (a) The state before deformation i.e., the reference state where 1 is the polymer volume fraction of gel with volume V_0 . (b) The state after the deformation. Here ϕ_p is the polymer volume fraction in the gel.

Where f_{sol} is the free energy density of the polymer solution of concentration ϕ_p . Taking into account Eq. 3, Eq. 4 can be rewritten as

$$f_{mix}(\lambda_i) = \frac{f_{sol}(\phi_p)}{\phi_p} \quad \text{Eq. 5}$$

The expression of f_{sol} is provided by the Flory-Huggins thermodynamic theory of polymer solutions⁴ as

$$f_{sol}(\phi_p) = \frac{kT}{v} [(1 - \phi_p) \ln(1 - \phi_p) + \chi(1 - \phi_p)] \quad \text{Eq. 6}$$

where k is Boltzmann's constant, T is the temperature, v is the volume of a solvent molecule, and χ is a dimensionless measure of the enthalpy of mixing known as the Flory parameter. The first term on the right-hand side corresponds to the configurational entropy of the swollen polymer and the second term corresponds to the mixing enthalpy.

The free energy density of the gel is thus given by

$$f(\lambda_i) = f_{ela}(\lambda_i) + \frac{f_{sol}(\phi_p)}{\phi_p} \quad \text{Eq. 7}$$

2.2. Swelling equilibrium

The equilibrium state of the polymer is obtained by minimizing Eq. 7 with respect to ϕ_p . The condition $\frac{\partial f}{\partial \phi_p} = 0$ gives :

$$f'_{ela} = \frac{f'_{sol}}{\phi_p} - \frac{f_{sol}}{\phi_p^2} \quad \text{Eq. 8}$$

Where the symbol ' stands for the derivative with respect to ϕ_p . In what follows, we derive the swelling equilibrium under various geometrical constraints relevant to the present study.

2.2.1. Isotropic swelling

When a sample is free-standing, it is in a stress-free state and swells isotropically, $\lambda_1 = \lambda_2 = \lambda_3 = \lambda$. The polymer volume fraction is thus $\phi_p = \frac{1}{\lambda^3}$ and the swelling ratio is $S = \lambda^3$. According to equation 7:

$$f(\phi_p) = \frac{G_0}{2} \left[3 \left(\frac{1}{\phi_p} \right)^{\frac{2}{3}} - 3 - 2 \ln \left(\frac{1}{\phi_p} \right) \right] + \frac{f_{sol}(\phi_p)}{\phi_p} \quad \text{Eq. 9}$$

The swelling equilibrium given by Eq.8 thus writes:

$$G_0 [\phi_p^{1/3} - \phi_p] = \phi_p f'_{sol} - f_{sol} \quad \text{Eq. 10}$$

Where the right hand side term corresponds the osmotic pressure $\Pi(\phi_p)$ of the polymer solution of concentration ϕ_p . Then, Eq. 6 yields:

$$\Pi = -\frac{kT}{v} \left[\ln(1 - \phi_p) + \phi_p + \chi \phi_p^2 \right] \quad \text{Eq. 11}$$

According to Eqs (10) and (11), the swelling equilibrium can be expressed as a function of the stretch ratio λ as

$$G_0 \left(\frac{1}{\lambda} - \frac{1}{\lambda^3} \right) = -\frac{kT}{v} \left[\ln \left(1 - \frac{1}{\lambda^3} \right) + \frac{1}{\lambda^3} + \frac{\chi}{\lambda^6} \right] \quad \text{Eq. 12}$$

2.2.2. Swelling of hydrogel film attached to a rigid substrate

When a film is attached to a rigid substrate, it is restricted to swell only in the normal direction to the substrate (Figure 2 (a)), *i.e.* $\lambda_1 = \lambda_3 = 1$ and $\lambda_2 = \lambda$. The swelling ratio is $S = \lambda$ and the polymer volume fraction is $\phi_p = \frac{1}{\lambda}$. From Eq. 2, we obtain:

$$f'_{ela} = G_0 \left(\frac{1}{\phi_p} - \phi_p^2 \right) \quad \text{Eq. 13}$$

While the osmotic pressure term is still given by Eq. (11). Accordingly, the swelling equilibrium λ obeys Eq.14, which differs from Eq. 12:

$$G_0 \left(\lambda - \frac{1}{\lambda^2} \right) = -\frac{kT}{v} \left[\ln \left(1 - \frac{1}{\lambda} \right) + \frac{1}{\lambda} + \frac{\chi}{\lambda^2} \right] \quad \text{Eq. 14}$$

2.2.3. Plane strain swelling of a thin film

As it will be detailed below, we make the assumption that, close to the debonding line (Figure 2), the film is free to expand in a plane perpendicular to the delamination front but not in a direction parallel to this front, as a result of geometrical constraints. In other words, the hypothesis is that the film is in a plane strain state.

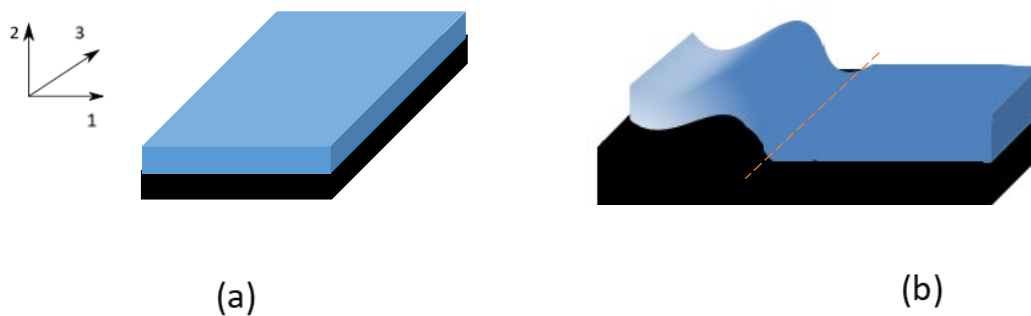


Figure 2:(a) The surface attached hydrogel swells only in one direction (direction 2), due to the geometrical constraints in directions 1 and 3. (b) A partially delaminated hydrogel film. Close to the debonded line, the delaminated film is assumed to be allowed to swell in directions 1 and 2 while it is restricted to swell in direction 3, $\lambda_3 = 1$ and $\lambda_1 = \lambda_2 = \lambda$.

Under such conditions $\lambda_1 = \lambda_2 = \lambda$ and $\lambda_3 = 1$. The swelling ratio is $S = \lambda^2$ and the polymer volume fraction $\phi_p = \frac{1}{\lambda^2}$. Accordingly, the derivative of the free elastic energy term is

$$f'_{ela} = G_0(1 - \phi_p) \quad \text{Eq. 15}$$

The swelling equilibrium thus reads:

$$G_0 \left(1 - \frac{1}{\lambda^2}\right) = -\frac{kT}{v} \left[\ln \left(1 - \frac{1}{\lambda^2}\right) + \frac{1}{\lambda^2} + \frac{\chi}{\lambda^4} \right] \quad \text{Eq. 16}$$

2.3. Swelling stresses

By definition, the swelling stresses are given by the derivative of the elastic free energy of swelling with respect to the stretch ratio, i.e.

$$\sigma_{ii} = \frac{\partial f_{ela}}{\partial \lambda_i} \quad \text{Eq. 17}$$

Where σ_{ii} denotes the *true* stress, i.e., the stress corresponding to a force applied to the current (swollen) material configuration. For one-dimensional swelling, $\sigma_{22} = 0$ and

$$\sigma_{11} = \sigma_{33} = -G_0 \left(\lambda - \frac{1}{\lambda} \right) \quad \text{Eq. 18}$$

The nominal stress, i.e., when the applied forces are expressed with respect to the reference (unswollen) configuration, is

$$P_{11} = P_{33} = -G_0 (\lambda^2 - 1) \quad \text{Eq. 19}$$

Similarly, for plain strain (2D), the compressive stresses write

$$\sigma_{11} = \sigma_{22} = 0 \quad \text{Eq. 20}$$

$$P_{11} = P_{22} = 0 \quad \text{Eq. 21}$$

$$\sigma_{33} = -G_0 \left(1 - \frac{1}{\lambda^2}\right) \quad \text{Eq. 22}$$

$$P_{33} = -G_0 (\lambda^2 - 1) \quad \text{Eq. 23}$$

2.4. Discussion

In Figure 3, the theoretical stretch ratio of the swollen network at equilibrium is plotted as a function of the shear modulus G_0 of the drained network. According to the above calculations, the stretch ratio and the corresponding water volume fraction $\phi_w = (1 - \phi_p)$ (inset in Figure 3) have been calculated for isotropic swelling, one-dimensional swelling, and plane strain swelling. For these calculations, we take for the Flory Huggins parameter $\chi = 0.57$, a value which was previously measured from water sorption isotherms using the same PDMA network.^{10,11}

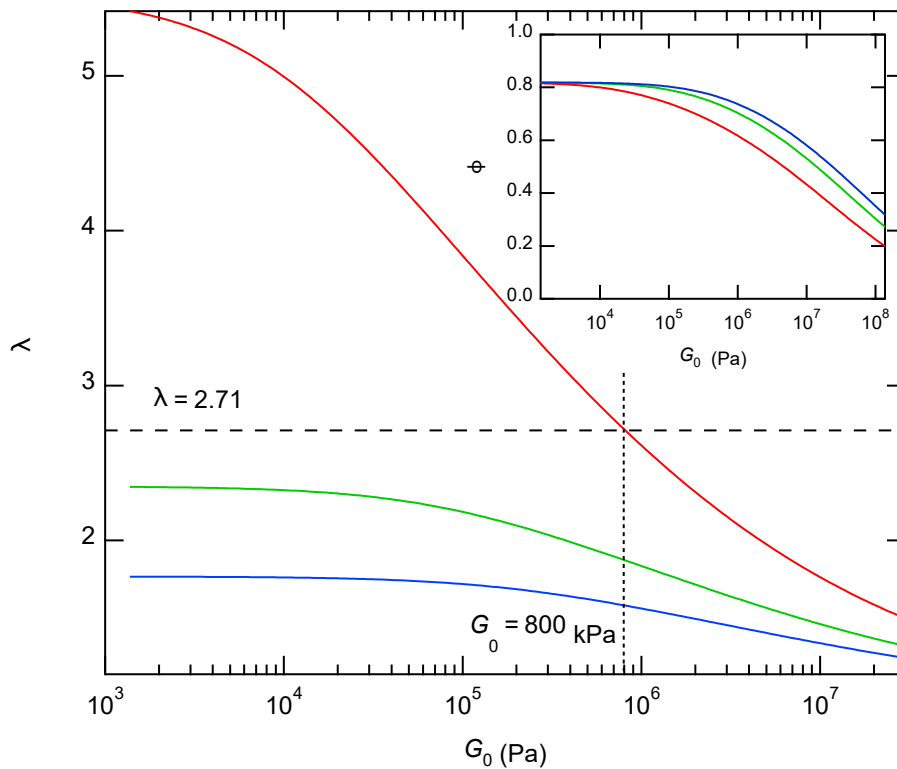


Figure 3 Theoretical stretch ratio λ at swelling equilibrium as a function of the shear modulus G_0 of the drained network. (blue) isotropic swelling, eq. (12); (green) plane strain swelling, Eqn. (16) and (red) one dimensional swelling ,eq (14) ($\chi = 0.57$, $v = 2.99 \times 10^{-29} \text{ m}^3$). Inset: water swelling ratio as a function of G_0 . The horizontal dotted line corresponds to the measured average swelling ratio of the PDMA films used in the debonding experiments.

Unless otherwise stated, the equilibrium swelling ratio of all the hydrogel films to be used in the debonding experiments detailed below is $S = \lambda = 2.71 \pm 0.27$, as measured by ellipsometry. The corresponding water volume fraction is $\phi = 1 - \frac{1}{\lambda} = 0.63$. From Figure 3, this value of the equilibrium swelling ratio provides an estimate of the shear modulus, $G_0 = 800$ kPa. Accordingly, the compressive stresses within the bonded films can be estimated from Eq.18 to be $\sigma_{11} = \sigma_{33} \approx -1.9 \text{ MPa} \approx -2.4 G_0$, *i.e.* larger than the shear modulus.

Taking into account the same values of G_0 and χ , the equilibrium stretch ratio in plane strain conditions is found from Eq. 16 to be $\lambda = 1.87$ along the *l* and *2* directions. In other words, the debonded film close to the tip of the interface crack is expanding by a factor of 1.87 along the *one* direction (see Figure 2) while it is shrinking by a factor of $2.71/1.87 = 1.45$ in the *two* directions. As a result of the release of the geometrical constraints of the bonded film, there is thus a decrease in the delaminated film thickness and an in-plane expansion of the film along a direction perpendicular to the debonding line. The resulting water volume fraction is calculated to be $\phi_w = 0.71$, which is slightly lower than the equilibrium water volume fraction obtained for isotropic swelling ($\phi_w = 0.74$ with $\lambda = 1.58$).

3. Experimental setup

A specific setup was developed in order to control the swelling state of the films, with the requirements that: (i) the delamination pattern should be easily imaged, (ii) the initial time for delamination be clearly defined, and (iii) hydrogel swelling is homogeneous and constant over the whole sample during the delamination process. To do so, we choose to use humid air as a source of water, which allows easy imaging and initial time control, and the vapor is brought to the film by a gently flowing vapor flux over the film surface while decreasing the sample temperature. This allows to condensate water in the hydrogel film and ensures full saturation of the hydrogel film, as previously described.⁴

The steady-state swelling of hydrogel is well-controlled by the homemade set-up¹⁰, which is schematically described in Figure 4.a. Humid nitrogen is blown through a Plexiglas chamber equipped with a diverging inlet and a converging outlet on opposite sides to obtain a laminar flow of humid gas with controlled rate and prescribed humidity. Both L and W are larger than H so that the vapor velocity is homogeneous across the sample width at the center of the chamber where the sample is set (see Figure 4 b). We choose: $L = 28$ cm, $W = 4$ cm and $H = 1$ cm.

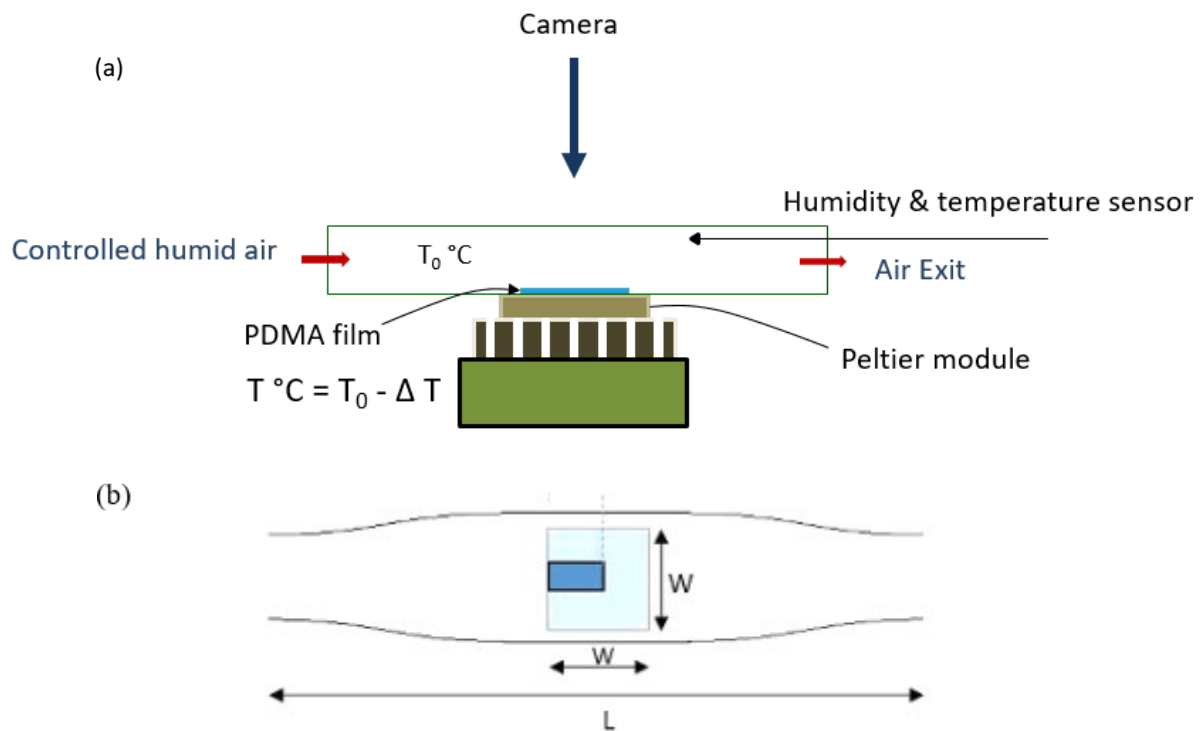


Figure 4 (a) Schematic side view of the experimental setup for delamination. The sample is placed in the Plexiglas chamber, which is designed to have laminar flow with controlled humidity. The temperature of the sample is controlled by the Peltier module below the sample, and the delamination is monitored by using a camera located above the chamber (b) Schematic top view of the Plexiglas chamber where the light blue square represents a $W \times W$ sized Peltier module, and the blue area the specimen. H is the height of the chamber.

Temperature and humidity are measured in real-time within the chamber using a humidity sensor (Rotronic HC2). The prescribed humidity level (65% in all the experiments to be reported) is achieved by bubbling nitrogen in deionized water and mixing it with dry nitrogen. The flow rate is set at 0.6 L min^{-1} and controlled by a flowmeter.

Water vapor flux at the film surface is controlled by the temperature difference between the substrate and vapor, as described in a previous work.⁴ In order to control the temperature of the sample, a Peltier module is placed at the bottom of the chamber. This Peltier module helps to achieve homogenous temperature throughout the sample surface and also to regulate the temperature below the ambient temperature. In all the experiments to be reported, the

temperature difference ΔT is kept constant at 10°C. All the samples are smaller than the size of the Peltier with 2*2 cm. The samples are placed on the Peltier module as depicted in Figure 4b.

Upon decrease of the sample temperature with respect to the flowing vapor temperature at the beginning of an experiment, the sample is fed with water molecules until a fully saturated, steady-state, swelling equilibrium is achieved. This occurs typically within less than 100 s, as indicated by the formation of condensation droplets at the film surface.¹⁰ The upper wall of the chamber is a glass window allowing observation of the film by means of a zoom lens (APO Z16, Leica) and a CCD camera (Sony XCD U100, 1600 x 1200, 8 bits).

4. Overview of debonding mechanisms

We report below typical observations when our samples, as prepared in Chapter 2, are set into the experimental chamber. Once equilibrium swelling is achieved, the hydrogel films start to debond from the substrate along the line defects at randomly distributed nucleation sites. Such a selective debonding of the gel film from the line defects validates our physico-chemical strategy of passivating the interface by using allyl butyl ether as a passivator of the grafting reaction of the polymer with the substrate. Depending on film thickness and swelling ratio, different debonding mechanisms are observed, which will be detailed below.

4.1. Phone cord debonding mechanisms

Figure 5 shows successive images taken during the initial stages of debonding of a film ~ 700 nm in thickness from a line defect (the swelling ratio is $S = 2.9$, and the amount of mercaptosilane is 100%M). The actual width of the line defect (9 μm) and its orientation are indicated in the figure by a blue box and dotted line, respectively. From Figure 5a, it turns out that delamination propagates both along the line defect and perpendicular to it, *i.e.*, on the grafted part of the film/substrate interface. As detailed below, the debonding rate along the line defect is typically of the order of 1 $\mu\text{m s}^{-1}$, while in the transverse direction, it is only in the 10⁻³ $\mu\text{m s}^{-1}$ range or less for the considered grafting density (100%M). Indeed, such a difference is consistent with the expectation of a reduced interface strength along the passivated line defect. The pictures also show extensive buckling and folding of the delaminated part of the films.

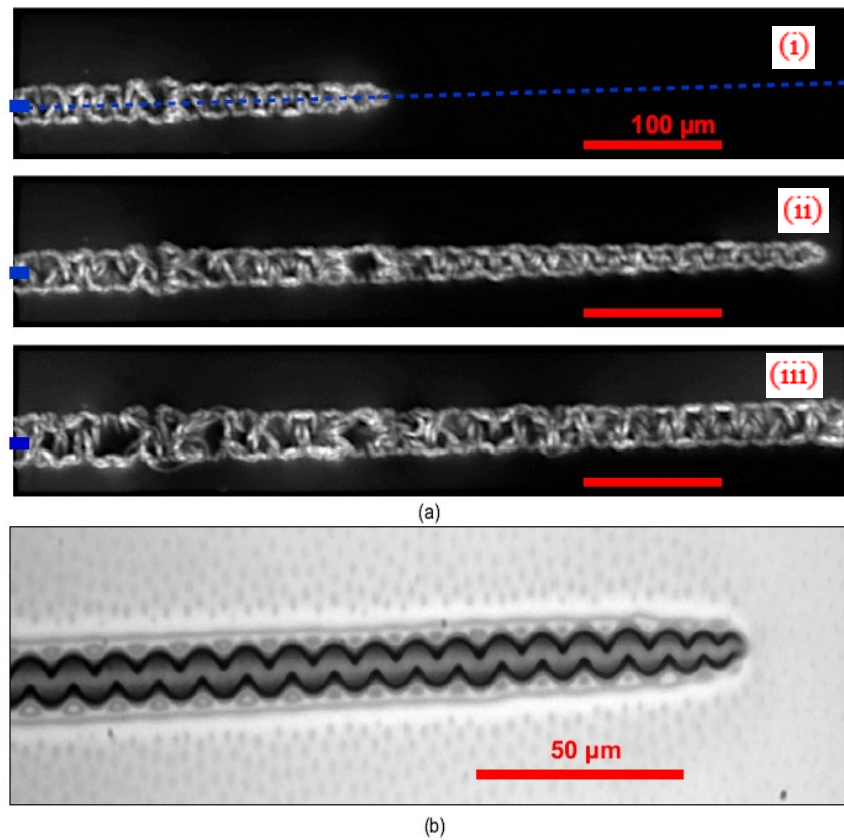


Figure 5: Phone cord debonding mechanism of a PDMA hydrogel film with thickness $h = 700 \text{ nm}$ (100 %M) and $S = 2.9$. The debonding starts from a line defect of width $L_0 = 9 \text{ }\mu\text{m}$. (a) Images of the top view of the swollen hydrogel film were taken (i) 360, (ii) 420, and (iii) 620 s after the exposure to the humid air. The blue dotted lines indicate the orientation of the line defect, and the blue area on the left indicates the line defect width L_0 . (b) microscopic image of the dried debonded hydrogel with the tip of the debonded area.

These instabilities are better imaged in Figure 5b, where post-mortem observations of the delaminated film are shown: by drying the film, the debonding of the film is frozen, which allows to image the debonded area with a microscope with enhanced resolution. The images show that the debonded part of the film exhibits a regular folding pattern which looks similar to the so-called telephone-cord architectures reported by Takahashi *et al.*¹² and Xu *et al.*¹³ for various kinds of thin, water-swollen hydrogel films, as briefly detailed in Chapter 1. These authors ascribed the phone-cord features to buckling instabilities resulting from the swelling-induced compressive stresses acting over the low adhesion areas. Here, the difference is that debonding and buckling over the passivated line defects are followed by the slow extension of the delaminated area outside the defect, that is, over the grafted film/substrate interface. In

addition to the action of compressive stresses, the buckling of the film is also promoted by the in-plane expansion of the film, which results from the release of the lateral constraints when the film debonds from the substrate. Accordingly, calculations detailed below show that the stretch ratio in a direction perpendicular to the debonding line and parallel to the film is increasing from 1 to 1.9 when it delaminates.

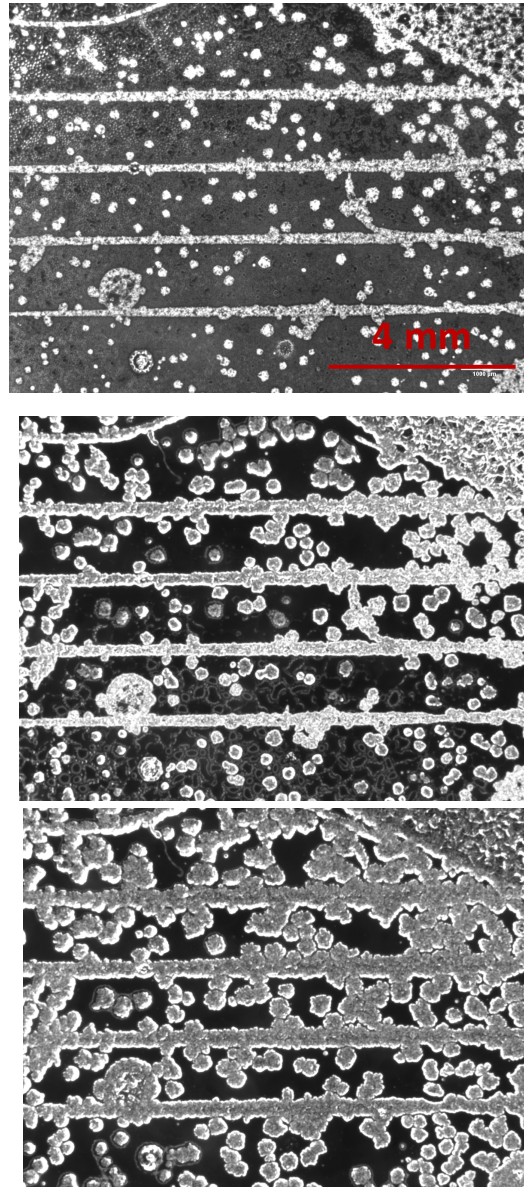


Figure 6: Debonding of a PDMA film grafted with 20% of mercaptosilane ($h = 0.6 \mu\text{m}$, $S = 3.4$, $L_0 = 9 \mu\text{m}$). Four defect lines are imaged. Time increases from top to bottom. In addition to delamination from the lines, spontaneous nucleation of delamination is observed outside the passivated defect lines.

When the amount of mercaptosilane used to graft the interface was considerably lowered, the phone cord delamination pattern was observed to co-exist with spontaneous nucleation of

circular debonding areas outside the passivated defect lines (Figure 6), which reflects the decreased interfacial strength.

Some additional observations regarding water transport close to a debonding line in the phone cord regime also deserve further comments. Figure 7 shows a network of condensation droplets close to a propagating phone cord debonding line. From Fig.7(i) to Fig.7(iv), as time goes by, the tip of the debonded line is propagating, and simultaneously, some of the neighboring water droplets ‘disappear’ thus indicating some water transport induced by delamination. A first hypothesis would be that the corresponding amount of water is absorbed within the delaminated part of the film. Indeed, we reported in paragraph 2.2 that the water volume fraction of the film is increasing from about 0.63 to 0.74 when the film debonds. Making the assumption that the contact angle of a water droplet on the swollen PDMA film is about 20° , a typical droplet diameter of $100\ \mu\text{m}$ yields a water volume of about $2.6 \cdot 10^{-13}\ \text{m}^3$. Taking into account the differential swelling ratio between the bounded and unbounded parts of the film, a delaminated strip of width $100\ \mu\text{m}$ would require a length of about $1\ \text{mm}$ to absorb the volume of a single droplet. This estimate is inconsistent with our observations. Instead, we make the assumption that the water of the droplets is trapped beneath the delaminated film. Indeed, an estimate of the volume of a blister $100\ \mu\text{m}$ in width (taking into account that the in-plane extension of the debonded film occurs by a factor of about 1.9) indicates that the volume of a water droplet would be trapped in a blister channel of about $400\ \mu\text{m}$ in length which seems consistent with the observations reported in Figure 7. It should also be mentioned that, for the considered thickness and swelling ratio, the film exhibits wrinkles (chapter 2, 3.3). Some channeling flow of water through the network of creases formed at the free surface of the gel could thus promote water transport from the droplets to the blister.

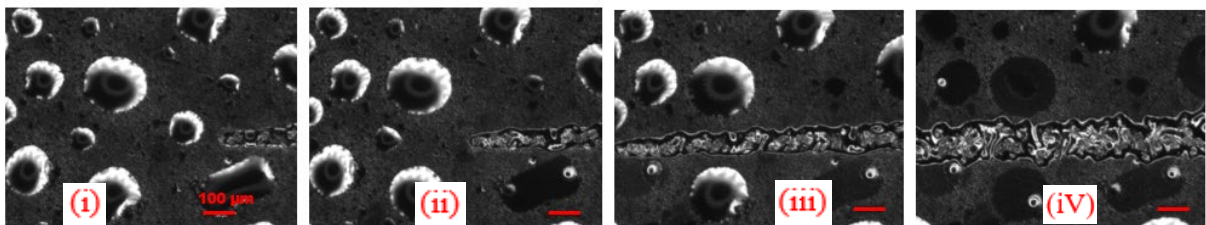


Figure 7: Water transport close to the tip of a debonding line in the phone cord regime ($h = 1.5\ \mu\text{m}$, $S = 2.5$, and $L_0 = 20\ \mu\text{m}$). Images taken (ii) 17 s, (iii) 71 s and (iv) 210 s after (i). Water condensation droplets are observed to disappear close to the debonded area.

4.2. Dendritic delamination patterns

The above reported phone-cord debonding mechanisms are observed to evolve with film thickness and swelling ratio.

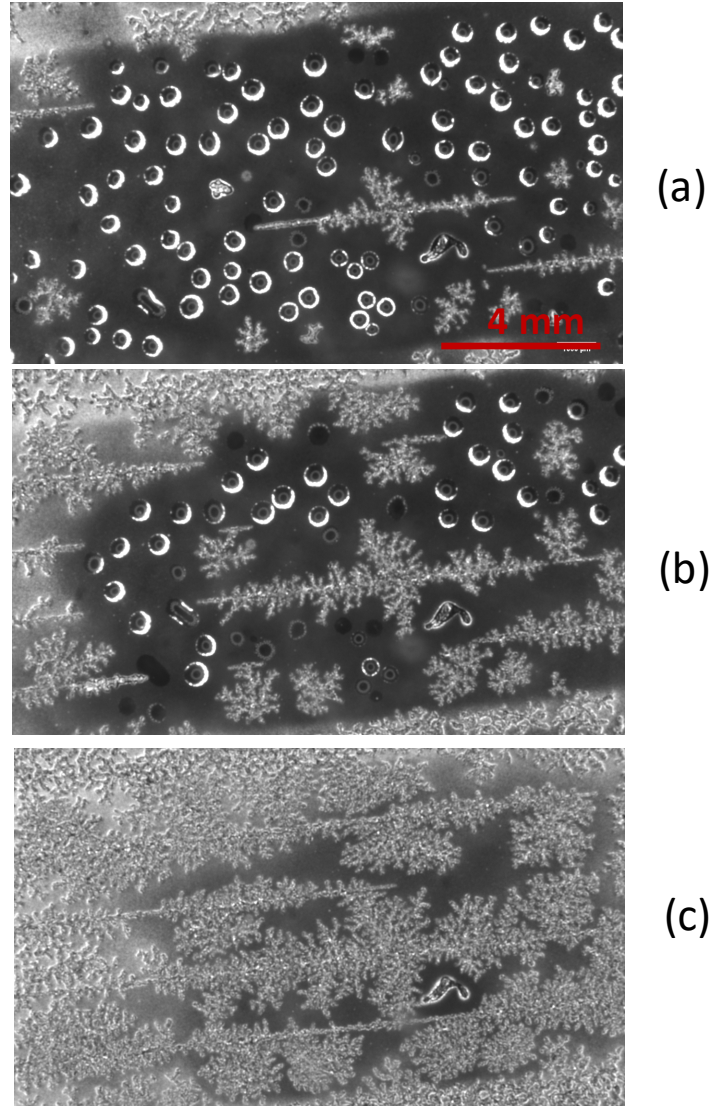


Figure 8: Dendritic delamination pattern achieved for a swollen PDMA film with $h = 3.2 \mu\text{m}$, $S = 3.4$ at (a) 300 s (b) 380 s (c) 510 s after exposure to humid airflow (100%M, $L_0 = 9 \mu\text{m}$). Dendrites are formed from a set of 4 parallel passivated lines (water condensation droplets are also seen in the images).

Figure 8 shows the delamination images for a PDMA hydrogel film with a larger thickness ($h = 3.2 \mu\text{m}$) and swelling ratio ($S = 3.4$) than in Figure 5, and the same grafting conditions (100%M) as before. The film starts to delaminate according to a phone cord mechanism which rapidly evolves toward a dendritic pattern. The enhanced delamination of the film at higher thicknesses can be qualitatively explained by the increased strain energy available in the

swollen film to debond the interface (the strain energy is proportional to the volume of the swollen gel, *i.e.*, to its thickness).

4.3. Phase diagram for debonding mechanisms

A phase diagram showing the domains for the existence of the phone cord and dendritic patterns is shown in Figure 9 as a function of dry film thickness h and swelling ratio S for interfaces grafted with 100% mercaptosilane. It turns out that the phone cord debonding mechanism is only promoted for low film thicknesses, typically less than 1.2 μm , except for the lowest swelling ratio ($S \sim 2$), where the boundary between the phone cord and dendritic regimes is shifted at higher film thicknesses. When the percentage of mercaptosilane used to graft the film is lowered down to 20%, the phone cord mechanism observed for $h < 1.2 \mu\text{m}$ remained unchanged, except that spontaneous nucleation was also observed outside the passivated line defects (see above). Nevertheless, we will see below that the debonding rate is drastically enhanced when the grafting density is reduced.

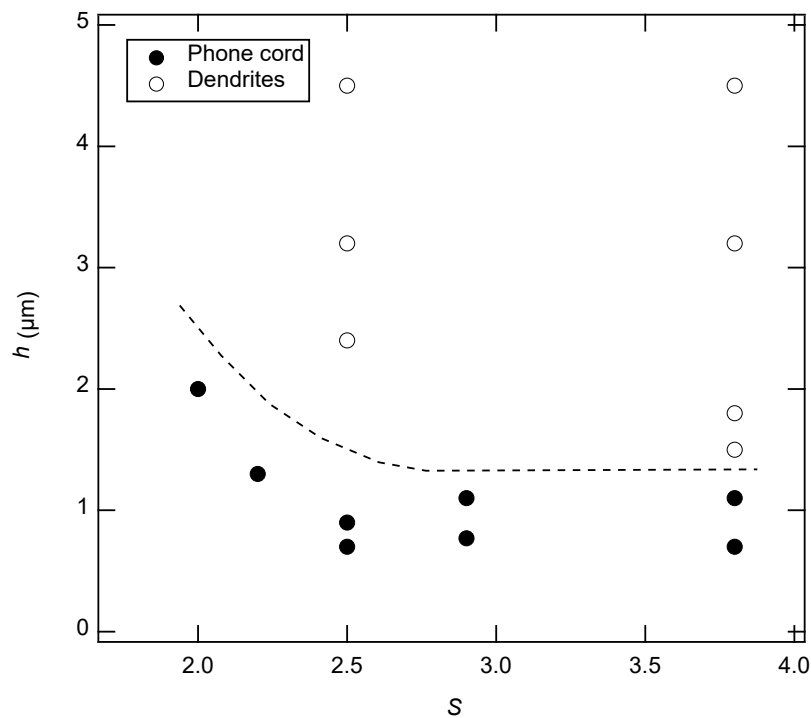


Figure 9: Phase diagram delimiting the regimes where phone cord and dendritic delamination are observed as a function of the dry thickness h of the film and of its equilibrium swelling ratio S (100%M).

At high film thicknesses and swelling ratios, the development of dendritic patterns can be attributed to the enhanced energy available for debonding as a result of the increase in the swelling stress (for increased S) and in the volume of the stressed network (with h).

Within the framework of this study, the objective is to evaluate quantitatively the interfacial strength of the film/substrate as a function of the grafting density. For that purpose, we focus in what follows on debonding mechanisms in the phone cord regime where a comprehensive fracture mechanics analysis of interface properties remains tractable (see below). So, all the experiments to be reported below are carried out for thickness h below $1.2 \mu\text{m}$.

5. Debonding in the phone cord regime

In this section, we provide a refined description and interpretation of the debonding mechanisms in the phone cord regime. For the purpose of quantitative measurements, the debonding velocity along the lines defects and perpendicular to it are carried out using the methodology described below.

5.1. Measurement of the debonding velocity

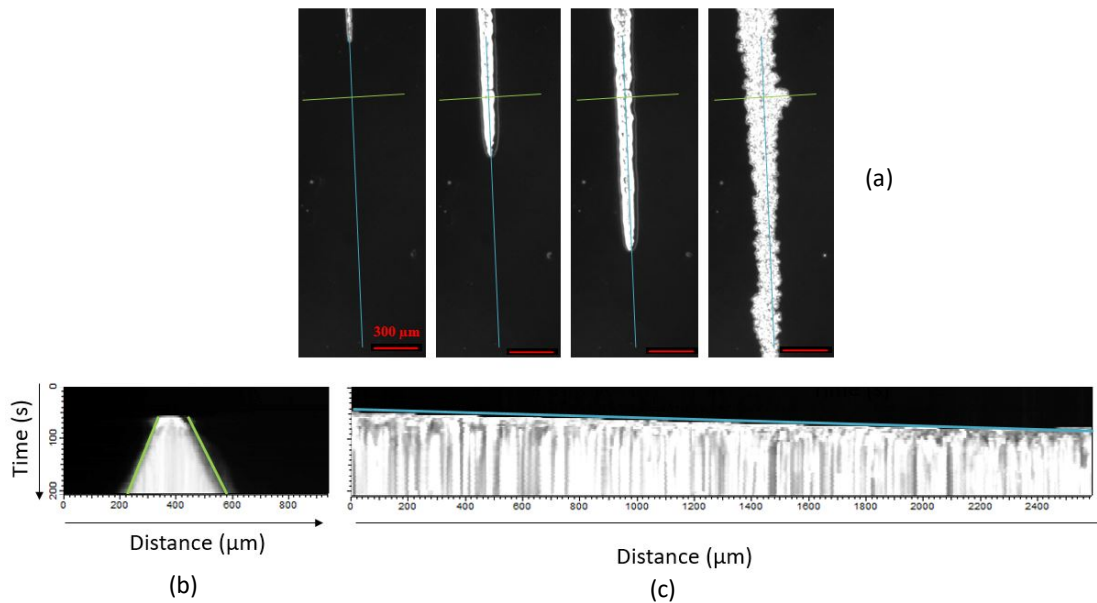


Figure 10: Measurement of the longitudinal (V_l) and transverse (V_t) debonding velocities in the phone cord regime. (a) images of the debonding line at increasing times; (b) space-time plot of profiles taken perpendicularly to the defect line at the position indicated by the green line; (c) space-time plot of profiles taken along the defect line at the position indicated by the blue line. In (b) and (c), the time derivative of the position of the crack (green and blue lines) provides $V_t(t)$ and $V_l(t)$.

In order to measure the debonding rate both along and perpendicular to the passivated defect line, we extract space-time plots along specified line profiles from sequences of gray level images, as shown in Figure 10. From an image processing of these time-space plots, we detect

the coordinates of the boundary between the bounded and delaminated areas (the red and blue lines in Figure 10(b) and (c)). A time derivative of these boundaries then yields the longitudinal, $V_l(t)$, and transverse, $V_t(t)$, velocities as a function of time. In what follows, the time origin will be taken as the time at which debonding is first detected along the profile which used to plot the time-space representation.

When the debonding line presents some waviness (see below), we increase the width of the line profile used to extract the space-time image in order to get an average position of the crack front (the width of the line profile is then taken larger than the wavelength of the crack front).

We first compared the transverse to the longitudinal velocities for a set of hydrogel films with different thicknesses, swelling ratios, and grafting densities. It turns out that the ratio of the longitudinal to transverse velocity V_l/V_t is always of order 10^2 to 10^3 . This observation can be rationalized by noticing that in the longitudinal direction, there is no grafting between hydrogel and substrate, and once the debonding nucleates, it propagates without breaking covalent bonds. Conversely, breaking covalent bonds is involved in the case of transverse debonding. This observation is the first indication of the sensitivity of the debonding velocity on grafting density.

In what follows, we focus on the transverse velocity V_t which is carrying the relevant information regarding the dependence of the gel/film interface on the surface density of thiol groups available for grafting at the surface of the silicon wafer.

5.2. Relevance of buckling stresses to delamination mechanisms

Phone-cord mechanisms were extensively reported for rigid film/substrate systems where the film is in a state of biaxial compression as a result, for example, of thermal expansion mismatches^{14,15}. Interface failure in these systems often results in the formation of regions, such as the phone cord blisters, where the film has been buckled away from the substrate. Buckling of the film then loads the edges of the interface cracks, thus promoting further interfacial crack propagation. This is schematically depicted in Figure 12a). In order to assess the relevance of such a driving force for crack propagation in our gel system, we measured the initial debonding rate V_{ini} in the transverse direction as a function of the width L_0 of the line defect. V_{ini} is measured for a width of the debonding area, which does not exceed 5% of L_0 . The results are plotted in Figure 11 as a function of L_0 and show that V_{ini} is not significantly affected by the initial defect width L_0 . *i.e.*, by the size of the delaminated blister. This observation indicates that

delamination of the film is not driven by buckling-induced stress, which is expected to depend on the width of the blister.

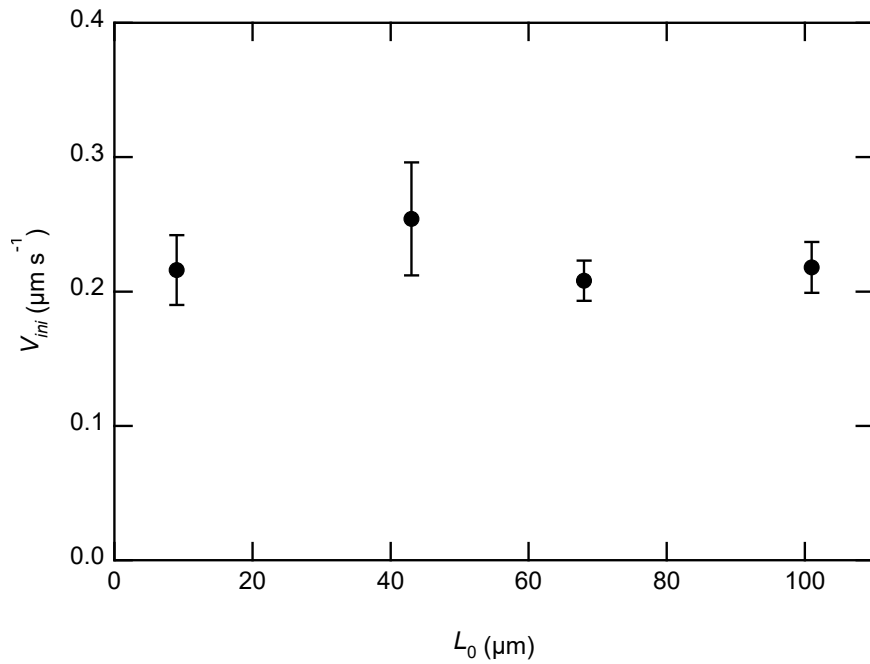


Figure 11: Initial transverse debonding rate V_{ini} as a function of the width L_0 of the line defect ($h = 680$ nm, 100% M , swelling ratio $S = 3.4$)

Instead, we should rather consider that debonding results from localized stresses close to the crack. As depicted in Figure 12b), we offer to take into account the difference in swelling state between the grafted and delaminated parts of the film, which leads to differential swelling stresses close to the crack tip. This conclusion is further supported by the observation that the debonding rate is not significantly affected when delamination is induced from an edge defect, *i.e.*, when $L_0 \rightarrow \infty$ (results not shown).

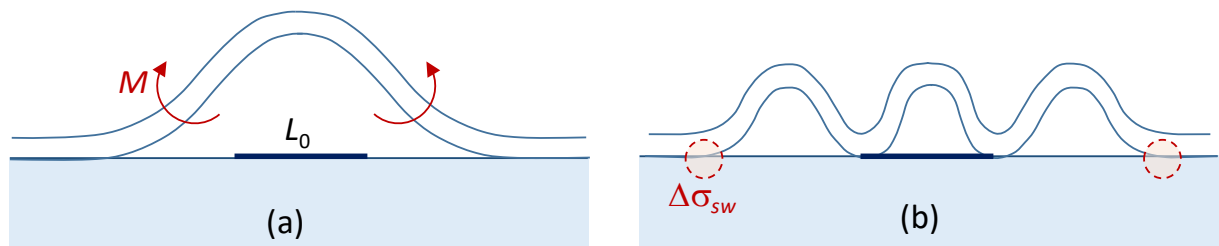


Figure 12: Schematic of potential delamination mechanisms from a defect line of width L_0 . (a) debonding induced by flexural momentum M resulting from the buckling of the film; (b) debonding induced by localized differential stress $\Delta\sigma_{sw}$ between the bounded and delaminated parts of the film close to the crack tip. For the considered hydrogel film systems, (b) is the relevant mechanism.

5.3. Dependence of transverse velocity on time

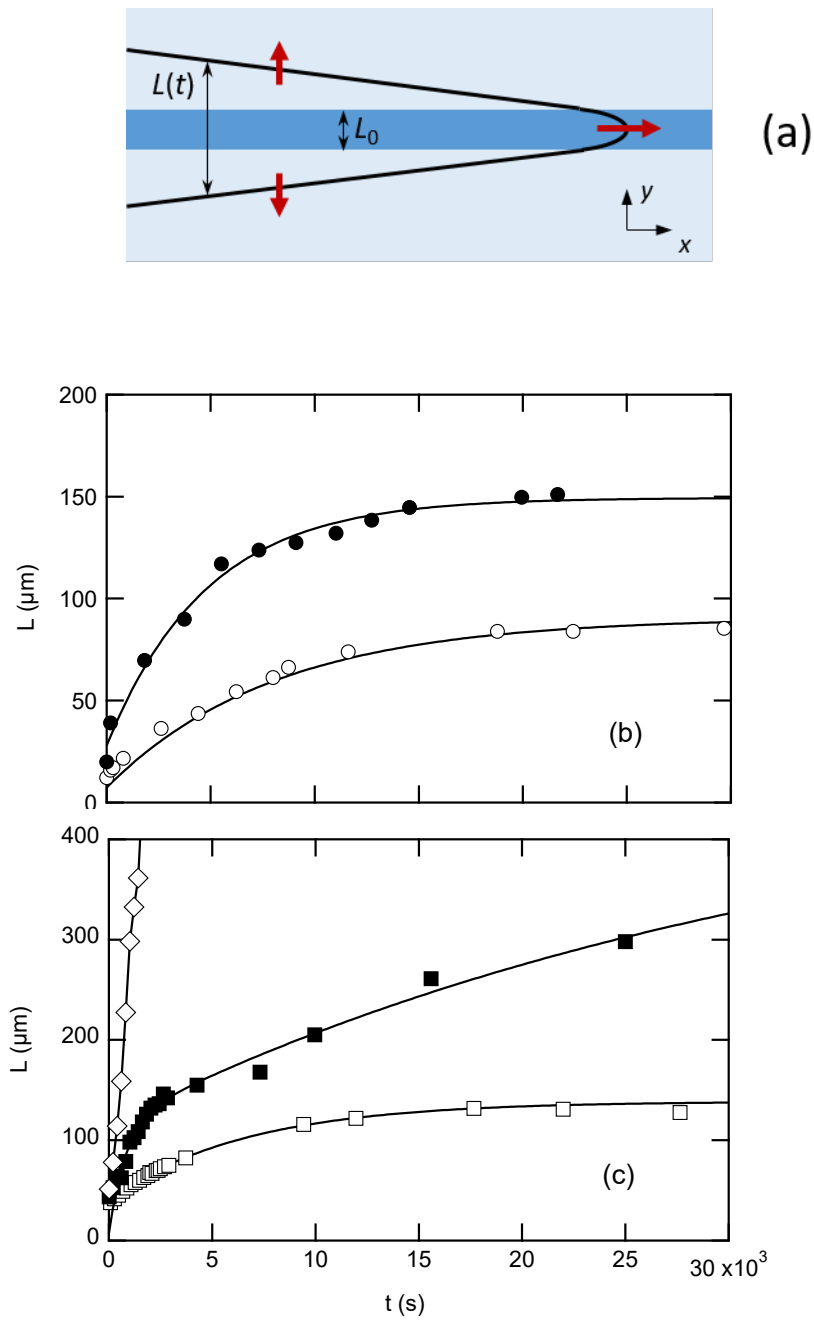


Figure 13: Width L of the debonded area as a function of time ($L_0 = 9 \mu\text{m}$). (a) schematic of delamination width $L(t)$ along y direction from an interface defect L_0 with $L(t = 0) \sim L_0$ (b) Films grafted with 100% mercaptosilane; (\circ) $h = 770$ nm (\bullet) $h = 1130$ nm; (c) hydrogel films grafted with 50% mercaptosilane; (\square) $h = 480$, (\blacksquare) $h = 700$ and (\diamond) $h = 1060$ nm.

We now focus on the time-dependence of the lateral extension of line defects for a silicon substrate grafted with various amounts of mercaptosilane and for gel films with thicknesses h

in the range 700-1130 nm. All the results presented here are obtained with a line defect of width $L_0 = 9 \mu\text{m}$. In Figure 13, the width $L(t)$ of the measured delaminated part is measured over time, as depicted in Figure 13a). The results are plotted in Figure 13b), c). It turns out that delamination progressively stops at some width which increases with film thickness (Figure 13b), except for the thickest film with the lower grafting density ($h = 1060 \text{ nm}$, 50%M), where no delamination arrest is evidenced (Figure 13.c).

In Figure 14, the saturated debonding width L_∞ is plotted as a function of dry thickness for different grafting densities of the silicon substrate. L_∞ increases with the thickness of the film or when the grafting density is lowered. For thicker films and lower grafting density, no saturation is observed, and debonded areas generated from neighboring defect lines eventually merge, thus resulting in a complete delamination of the hydrogel coating.

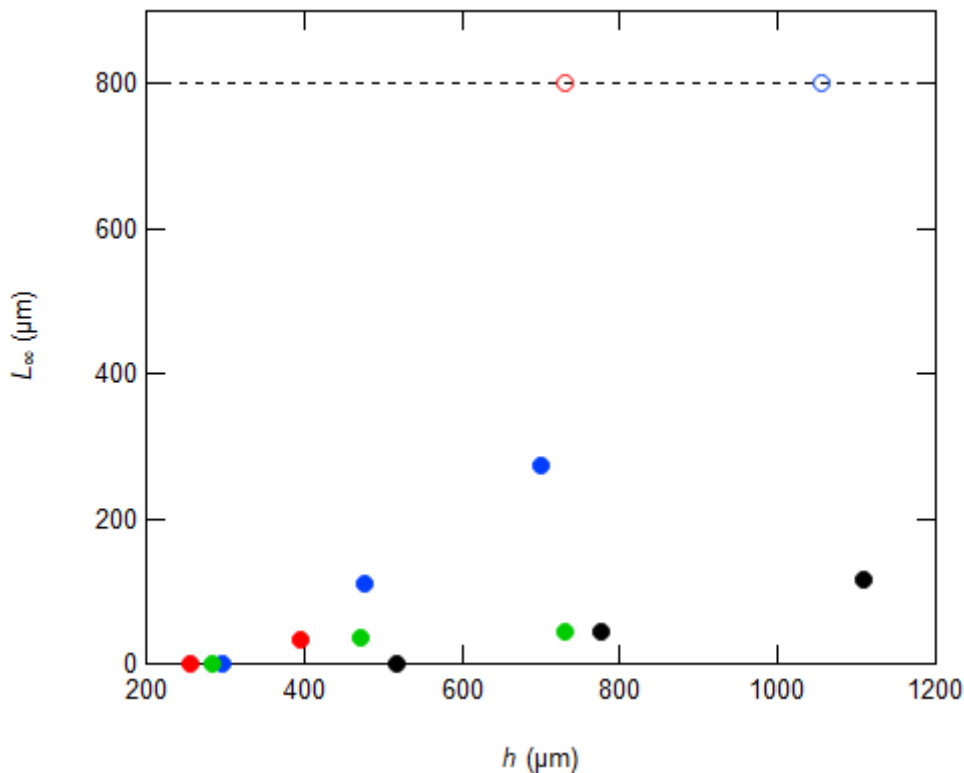


Figure 14: Saturated debonded width L_∞ as a function of the dry film thickness h for film grafted with (•) 25%, (•) 50%, (•) 75%, and (•) 100% mercaptosilane. Dotted line and open symbols denotes situations where no saturation is observed and debonded areas coming from neighboring line defects eventually merge to induce a complete debonding of the film.

In order to investigate the mechanisms behind the slowing down of the debonding process, we dried the samples at different debonding times in order to freeze the debonded morphology, and

we imaged them with enhanced resolution using a microscope in a low humidity atmosphere. A typical example is shown in Figure 15 for a film $1.2 \mu\text{m}$ in thickness grafted with 100% mercaptosilane, together with the corresponding $L(t)$ relationship.

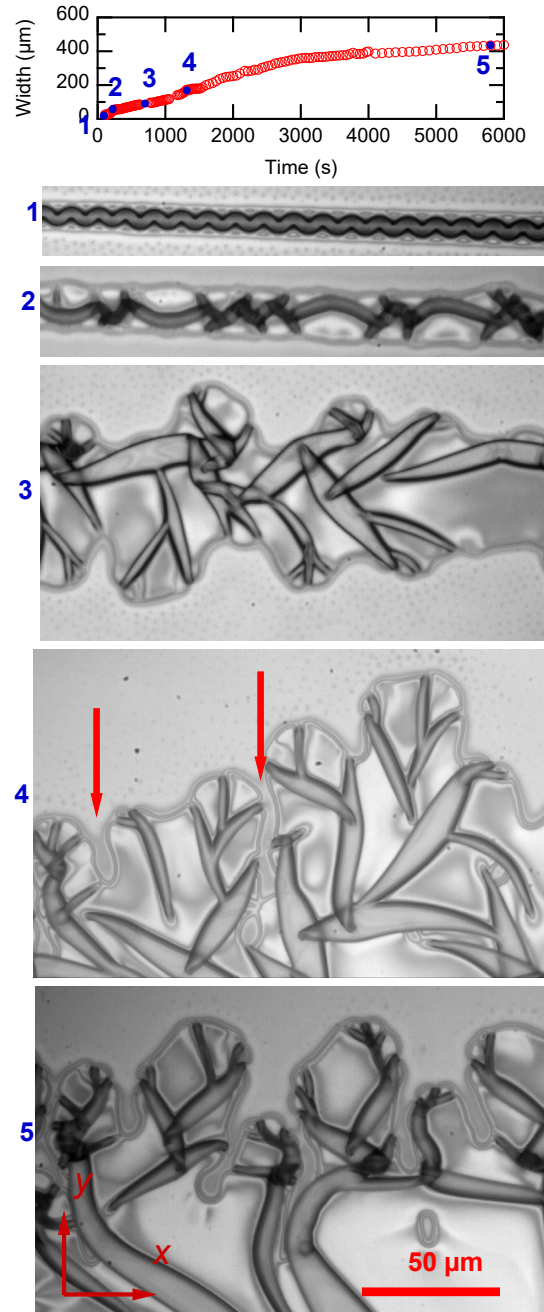


Figure 15: Microscope images of a dried debonded hydrogel film at different stages of the delamination. ($h = 1.2 \mu\text{m}$, 100 % M). (a) width L of the debonded line as a function of time. (b) Images of the debonded line taken at different times denoted 1 to 5 in (a). Only half of the debonded line is shown in images (4) and (5). All the microscopic images are taken after drying the film. Adhering film digits with a width of about ten times the film thickness is shown by arrows.

It turns out that the gradual decrease in transverse velocity is correlated to the development of a wavy crack line with an approximately constant wavelength of around 40 μm , i.e., about ten times the thickness of the swollen film. We found that this ratio is preserved when the film thickness which is varied from 470 to 1100 nm and the amount of mercaptosilane from 50 to 100%. As the delamination front moves forward, digits of adhering film with increased lengths are formed (shown by red arrows in Figure 15). Noticeably, the width of these digits is close to the thickness of the swollen films. For such a situation, the compressive swelling stress within the digits is likely to be relaxed along the longitudinal x-axis, thereby taking the driving mechanism for crack propagation along the y-axis below the threshold stress.

The development of such a waviness in the delamination front could tentatively be accounted for by fluctuations in the swelling stresses of the film along the crack front, which arises when the latter becomes curved as a result, for example, of non-homogeneities in the interface strength. Figure 16 presents a schematic representation of a wavy crack front viewed from the top in the (x,y) plane. When the crack is a line, swelling stresses only relax in the x direction. When the crack is wavy, swelling stress relaxation also occurs along the y -axis, and is likely to be favored when the crack front is convex with respect to the bonded part of the film as a result of the release of lateral constraints along this direction. Accordingly, the available strain energy for crack propagation and thus the debonding rate (denoted V_2 in Figure 16) will decrease. Conversely, swelling stress relaxation should be less efficient when the crack front is concave; thus, $V_1 > V_2$. Such differences in the debonding rate along the crack line will eventually result in enhancement of the amplitude of its waviness, as it is experimentally observed.

We can rationalize in a more quantitative way these assumptions by considering that the material close to a concave crack tip (region [1] in Figure 16) is approximately under a plane strain state, whereas close to a convex crack tip (region [2]) it is rather under a plane stress state. This hypothesis is justified by the fact that in [1], the length along the y direction is much higher than the length scales in the other two directions; conversely, after the finger-like instability is fully developed, the width in the y direction is comparable to the characteristic lengths in the two other directions. Using these assumptions, we can tentatively attribute the development of the finger-like instabilities by the fact that the free energy density of the bounded film in-plane strain is lower than that under plane strain.

For plane strain swelling, we get from equation Eq.7 the following expression for the free energy density $f_{Pstrain}$

$$f_{Pstrain} = G_0[\lambda^2 - 1 - \ln\lambda^2] + \frac{kT}{\nu} \left[(\lambda^2 - 1) \ln \left(1 - \frac{1}{\lambda^2} \right) + \chi \left(1 - \frac{1}{\lambda^2} \right) \right] \quad \text{Eq. 24}$$

Plane stress swelling is the same as the free swelling state described by Eq. 9. Accordingly, the corresponding free energy density $f_{Pstress}$ writes

$$f_{Pstress} = \frac{G_0}{2} [3\lambda^2 - 3 - 2\ln\lambda^3] + \frac{kT}{\nu} \left[(\lambda^3 - 1) \ln \left(1 - \frac{1}{\lambda^3} \right) + \chi \left(1 - \frac{1}{\lambda^3} \right) \right] \quad \text{Eq. 25}$$

Taking $G_0 = 800$ kPa and $\chi = 0.57$, the change of the free energy density $\Delta f = f_{Pstrain} - f_{Pstress}$ is found from Eq. 24 and 25 to be $\Delta f = 944 \cdot 10^3 \text{ J/m}^3 = 944 \text{ kPa} \sim G_0$, which means that under plane stress (i.e., in the finger-like regions) the free energy density is lower and of the same order of magnitude as the shear modulus.

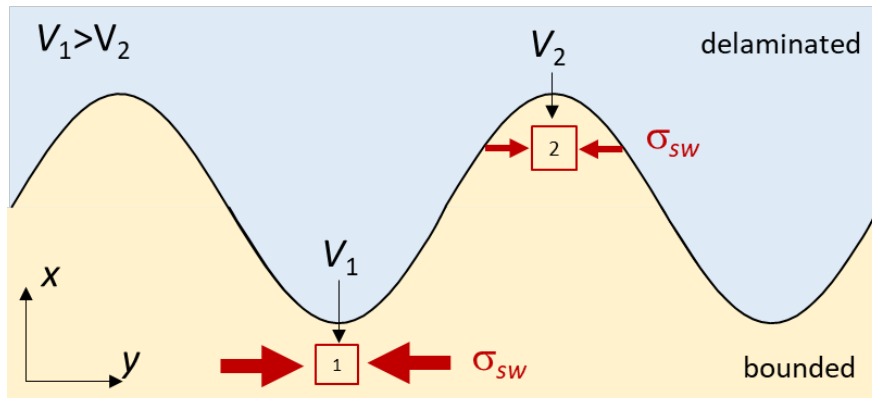


Figure 16: Debonding along a wavy crack front. Blue and yellow areas correspond to the delaminated and bounded part of the film, respectively. The crack line is moving from top to bottom when the crack front as a downward culture, and the relaxation of the compressive stresses σ_{sw} and y-axis is favored as compared to a crack front with an upward curvature. As a result, $V_1 > V_2$, which will enhance the amplitude of the crack front.

A prediction of the wavelength of the instability would require a more quantitative analysis which is beyond the scope of this paper. However, one could anticipate that this wavelength should be proportional to the film thickness, which is the only available length scale in the problem. Interestingly, in the literature, experimental^{16,17} and theoretical¹⁸ investigations of the peeling of thin films in confined geometries reveal the occurrence of similar crack front

instabilities with a characteristic wavelength of the order of 3-4 times the film thickness, a value close to that measured in the present study.

5.4. Threshold thickness for the occurrence of debonding

In what follows, we investigate the dependence of the initial debonding velocity as a function of film thickness. Figure 17 shows the relationship between debonding velocity and film thickness for different grafting densities (25, 50, 75, and 100% mercaptosilane). Here, the velocity V_0 is measured at the beginning of the debonding for a debonding width L of 20 μm (for a defect width $L_0 = 9 \mu\text{m}$), i.e., in a regime where the debonding line is predominantly linear as in image (1) and (2) in Figure 15. The measured velocities are plotted as a function of film thickness h in Figure 17. Our results clearly show that there is a threshold thickness above which the hydrogel coating delaminates. This threshold thickness h^* clearly increases with the amount of mercaptosilane used to graft the substrate (Figure 18). Above this threshold, orders of magnitude changes in the initial debonding velocity are measured when the film thickness is increased up to the μm range (Figure 17).

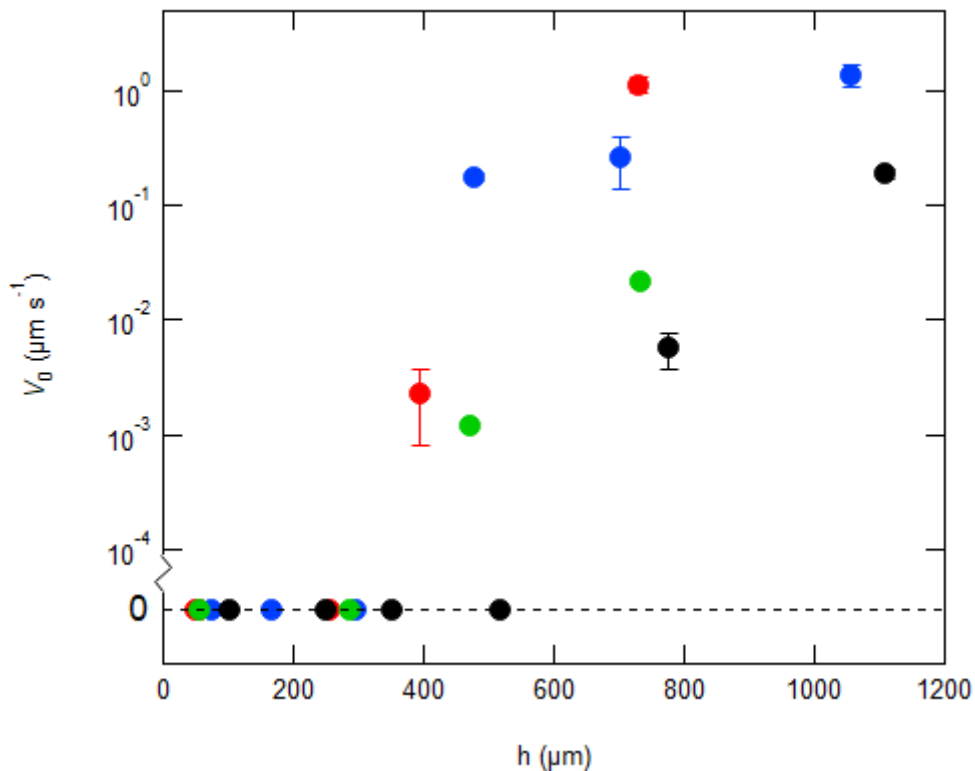


Figure 17: Initial debonding rate V_0 as a function of the dry film thickness h for films grafted with 25%, (•) 50%, (•) 75%, and (•) 100% mercaptosilane ($S = 2.9$).

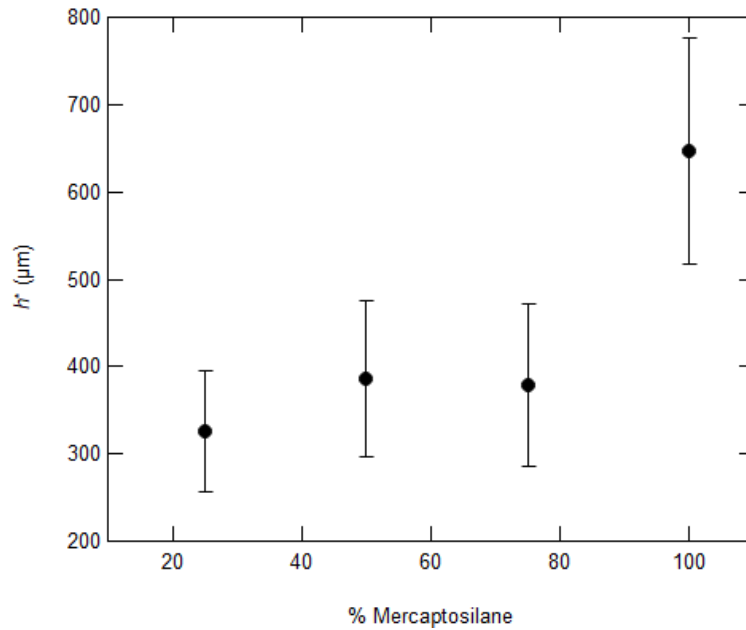


Figure 18: Threshold thickness h^* for delamination as a function of mercaptosilane content (h^* is determined from Figure 17 as the median thickness between two successive data points i, j with $V_0^i = 0$ and $V_0^j > 0$).

The existence of a threshold thickness for debonding can be qualitatively accounted for by a simple scaling argument where the elastic energy U_e per unit length released in the delamination of the constrained film is equated to the fracture energy of the interface Γ_0 . Taking $U_e = \sigma^2 h / E$, with E the Young's modulus, the threshold swelling stress for the occurrence of debonding scales as $\sigma_0 \approx \sqrt{\Gamma_0 \frac{E}{h}}$, i.e., it is decreasing as $1/\sqrt{h}$ for a given swelling ratio.

The measured transverse debonding velocities V_0 above the threshold are plotted in Figure 19 for hydrogel films with a thickness of 734 ± 31 nm, a swelling ratio of $S = 2.9$, and silicon substrates functionalized with 20 % to 100 % mercaptosilane. Order of magnitudes changes in V_0 is evidenced.

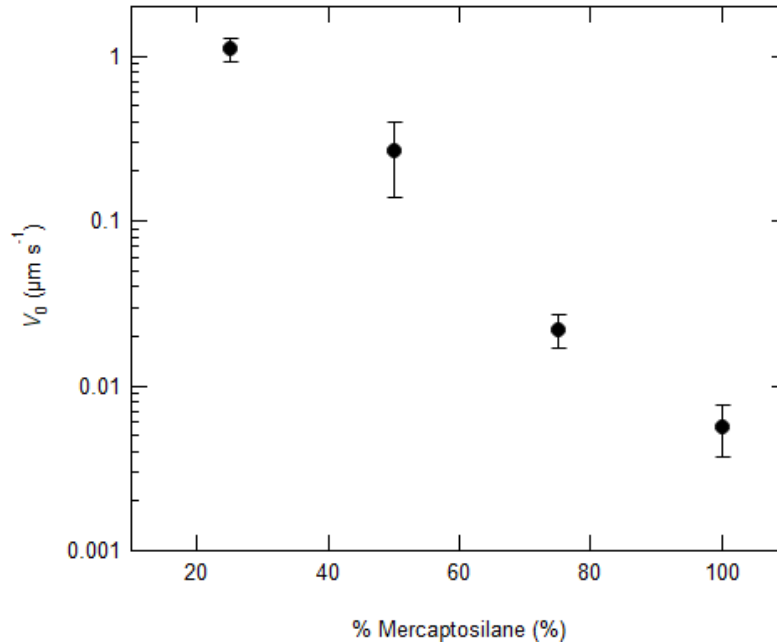


Figure 19: Initial debonding velocity as a function of mercaptosilane ratio at the substrate/gel interface for hydrogel films with thickness $h = 734 \pm 31$ nm ($L_0 = 9$ μm).

In the next section, we develop a more refined fracture mechanics analysis of delamination, which takes into account the nonlinearities of the swollen polymer network. From this analysis, we will especially derive quantitative values of the interface fracture energy Γ_0 from the measured thickness threshold h^* .

6. Theoretical crack model

In collaboration with Chung Yuen Hui and Bangguo Zhu at Cornell University, a fracture mechanics analysis of delamination was developed, which takes into account the nonlinear swelling of the polymer network.

Briefly, a nonlinear fracture mechanics approach to the debonding threshold is developed based on a calculation of the amount of energy that is released when the bonded, constrained layer, separates from the substrate and further swells. Here, this analysis is developed in the limit of a straight crack line propagating along the direction denoted as 1 in Figure 20, i.e., for the initial stages of delamination. The main assumption of the model is that debonding arises from

localized stresses induced by the differential swelling of the film in the grafted and delaminated states. Specifically, we make the assumption that close to the crack tip, the delaminated film is allowed to swell only in directions 1 and 2, i.e., the film is in a plane strain deformation state, while in the bonded part, the film is only allowed to swell in direction 2 by virtue of lateral constraints. In addition, we make the hypothesis that the only relevant stress in the bonded part of the hydrogel is the compressive swelling stress σ_{11} and that the debonded part is traction free. This latter hypothesis is justified by the extensive folding of the debonded film, which is observed experimentally.

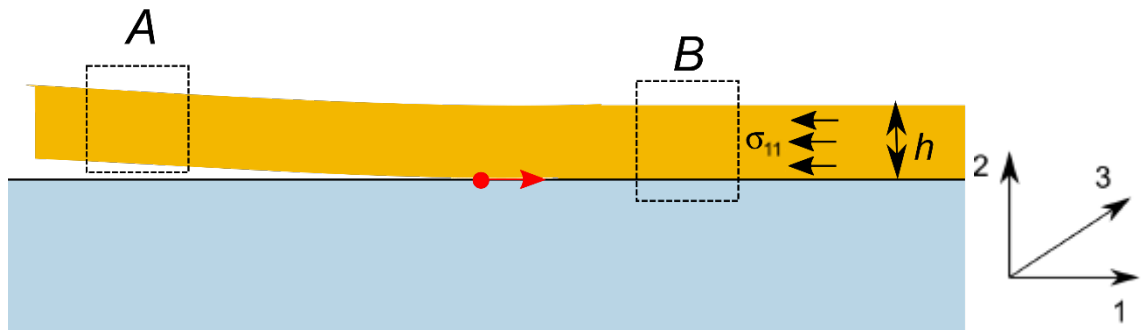


Figure 20: Reference configuration of the delaminated gel film of thickness h on a rigid substrate (before swelling). At point A, the material undergoes free swelling in-plane strain, whereas, at B, the material is constrained to swell only in direction 2. The out-of-plane direction is 3. Due to plane strain, the gel film at B is under a state of in-plane biaxial stress.

In the calculations, we also consider that the hydrogel is in a state of equilibrium with the solvent, i.e., the chemical potential of the solvent molecules inside the hydrogel is homogenous and equal to that of the solvent outside the network. This assumption is justified by the fact that we intend to determine the *equilibrium* conditions corresponding to the debonding threshold. After some calculations detailed in appendix B, the strain energy release rate Γ is expressed as

$$\begin{aligned} \frac{\Gamma}{G_0 h} = & \left[\left(\frac{\lambda_B^2 - 1 - 2 \ln \lambda_B}{2} + \ln \lambda_A^2 + \frac{1}{\lambda_A^2} - \frac{1}{\lambda_B} \right) \right] \\ & + \frac{kT}{\nu G} \left[(2\chi - 1) \left(\frac{1}{\lambda_A^2} - \frac{1}{\lambda_B} \right) + \frac{\chi}{\lambda_B^2} - \frac{\chi}{\lambda_A^4} \right] \end{aligned} \quad \text{Eq. 24}$$

Where λ_A (respectively λ_B) is the swelling ratio in the debonded state A (resp. bonded state B).

Figure 21 shows the calculated normalized strain energy release rate Γ/G_0h as a function of the shear modulus G_0 of the hydrogel for a value of the Flory interaction parameter $\chi = 0.57$.

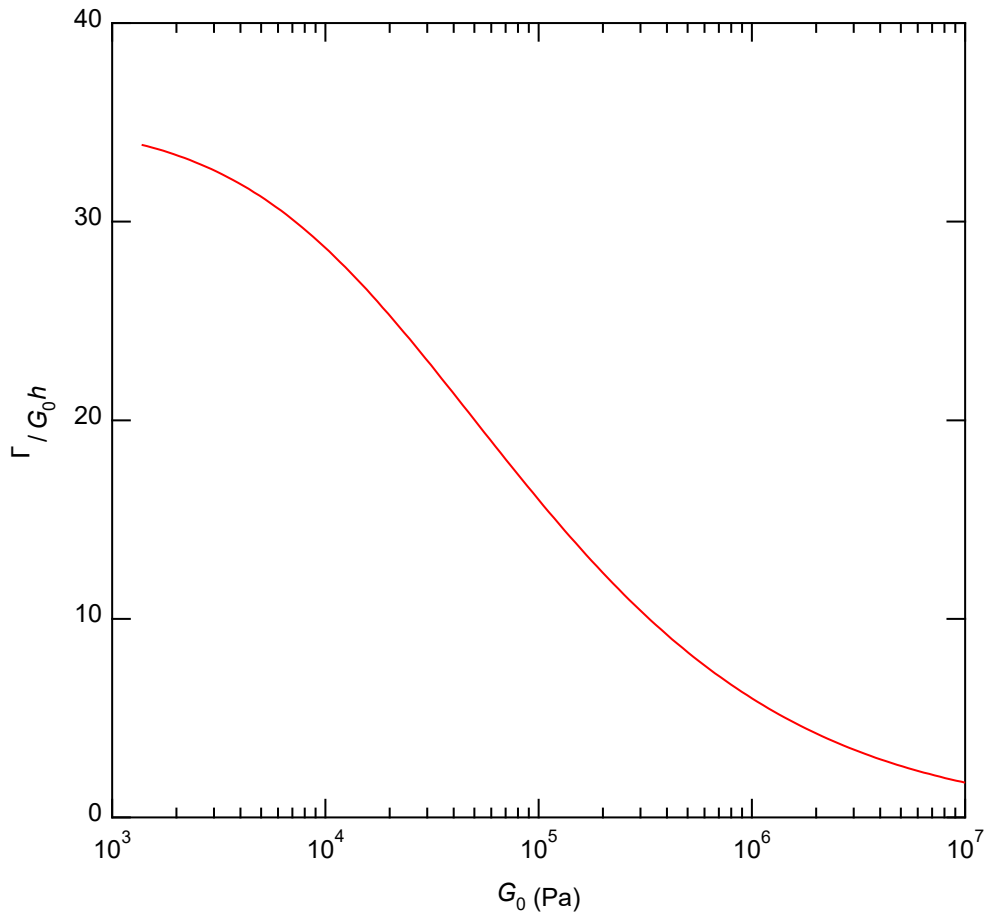


Figure 21: Non dimensional strain energy release rate Γ/G_0h (Eq (24)) for the delamination of a film with dry thickness h as a function of the shear modulus G_0 of the drained hydrogel network ($\chi = 0.57$).

7. Discussion

Under the action of swelling-induced stresses, well-controlled delamination of PDMA film from pre-existing defects with low adhesion was evidenced. The rate and extent of the debonding depend on the thickness of the film and on the grafting density of the substrate with thiol groups prior to the film deposition. The existence of a threshold thickness h^* below which the hydrogel does not debond is also evidenced. This threshold thickness corresponds to the

situation where the strain energy release rate Γ reaches the fracture energy of the interface Γ_0 , i.e., $h^* = \Gamma_0/G_0$.

Taking into account the value of the shear modulus deduced from swelling equilibrium in Section 2.4 Figure 3, i.e., $G_0 = 800$ kPa, Figure 21 provides $\Gamma_0/G_0h^* = 6.7$. When the amount of mercaptosilane is increased from 25% to 100 %, h^* is varying from 320 ± 70 nm to 650 ± 130 nm, and the associated threshold energy for delamination $\Gamma_0 = 6.7 G_0h^*$ is thus in the range of 1.7 to 3.5 J m⁻².

These values can be discussed in the light of simple molecular arguments taking into consideration the energy required to break stretched network chains that are grafted to the substrate. Such an approach was initially proposed by Lake and Thomas¹⁹ for rubber fracture and recently revisited by Akagi *et al.* in the context of the fracture of water-swollen polymer gels.²⁰ This theory states that when each bond breaks, the bond energy of each bond is irreversibly and fully lost. In our system, assuming that only the chains grafted to the silicon wafer do break and release energy, the threshold energy for crack initiation writes

$$\Gamma_0 = \eta U_b \Sigma \quad \text{Eq. 25}$$

Where η is the average number of bonds of the chains, Σ is the surface density of chains grafted on the silicon wafer and. U_b is the dissociation energy of the C-C bond, which is typically $U_b \approx 350$ kJ.mol⁻¹. From the value of the shear modulus, $G_0 = 800$ kPa, we can estimate the average molecular mass between crosslinks as $M_c = \rho RT/G_0 \approx 4.6$ kg mol⁻¹ and thus $\eta = M_c/m_n \approx 30$ with $m_n = 99$ g mol⁻¹ where with m_n the molar mass of the monomer. Finally, the surface density Σ is taken to be that of the thiol groups that are active for grafting, which was estimated from the XPS and ToF SIMS experiments reported in chapter 2, 3. The thiol surface density Σ was found to vary between 0.1 and 0.6 nm⁻² when the amount of mercaptosilane in the reactive silane mixture is varied from 20% to 100%. According to equation 40, the corresponding threshold fracture energy Γ_0 is found to be of the order of a few J m⁻² from Eq.40, which is consistent with the values derived from equation 24.

Here, we have derived values of the threshold fracture energy corresponding to the onset of delamination when the gel film is in a state of swelling equilibrium. A theoretical analysis of the debonding rate V_0 would require much more involved calculations taking into account the dissipative processes at skate when the crack front is moving. As detailed by Bouklas *et al.*²¹, the determination of the transient energy release rate needs to take into account the effect of

solvent diffusion, *i.e.*, to separate the energy lost in diffusion from the energy available to drive crack growth.²¹ Such an approach requires extensive numerical simulations, which are beyond the scope of this study.

8. Conclusion

Under a humid airflow ensuring full saturation of the gel network, swelling-induced stresses within the investigated PDMA hydrogel films were observed to induce delamination from pre-existing patterned line defects with low adhesion. We were able to show that the driving force for debonding is localized differential stresses close to the crack tip, which results from the difference in the swelling state of the film in the bounded and delaminated state, respectively. These mechanisms differ from blistering delamination in rigid coatings where bending stresses in the buckled film are the driving force for interface crack propagation

Our analysis of interface strength in relation to the grafting density was focused on a regime where the so-called telephone cord instability was the dominant instability. The debonding rate is found to decrease over two orders of magnitude when the amount of mercaptosilane in the reactive silane mixture is increased from 20% to 100%, *i.e.*, when the surface density of thiol groups available for grafting is increased from 0.1 to 0.6 nm⁻². A threshold thickness for the occurrence of debonding is also observed, which increases with the amount of mercaptosilane used to graft the substrate.

We derived quantitative values of the interface fracture energy from the measured thickness threshold using the fracture mechanics model, taking into account the non linearities of the highly swollen network. The values of the threshold fracture energy release rate obtained with this model are consistent with an independent approach based on an estimate of the energy required to break the covalent bonds between the hydrogel and the substrate at the interface.

9. References

- (1) Flory, P. J. *Principles of Polymer Chemistry*; Cornell University Press, 1953.
- (2) Flory, P. J.; Rehner, J. Statistical Mechanics of Cross-Linked Polymer Networks I. Rubberlike Elasticity. *The Journal of Chemical Physics* **1943**, *11* (11), 512–520. <https://doi.org/10.1063/1.1723791>.

- (3) Flory, P. J.; Rehner, J. Statistical Mechanics of Cross-Linked Polymer Networks II. Swelling. *J. Chem. Phys.* **1943**, *11* (11), 521–526. <https://doi.org/10.1063/1.1723792>.
- (4) Doi, M. *Soft Matter Physics*; Oxford University Press: Oxford, 2013. <https://doi.org/10.1093/acprof:oso/9780199652952.001.0001>.
- (5) Rubinstein, M.; Colby, R. H. *Polymer Physics*, 1st edition.; Oxford University Press: Oxford ; New York, 2003.
- (6) Treloar, L. R. G. *The Physics of Rubber Elasticity: By L.R.G. Treloar*, 3rd ed.; Oxford classic texts in the physical sciences; Clarendon Press ; Oxford University Press: Oxford : New York, 2005.
- (7) Flory, P. J. Thermodynamics of High Polymer Solutions. *Journal of Chemical Physics* **1941**, *9*, 660.
- (8) Flory, P. J. Thermodynamic Relations for High Elastic Materials. *Trans. Faraday Soc.* **1961**, *57*, 829. <https://doi.org/10.1039/tf9615700829>.
- (9) Wall, F. T.; Flory, P. S. Statistical Thermodynamics of Rubber Elasticity. *Journal of Chemical Physics* **1951**, *19*, 1435.
- (10) Delavoipière, J.; Heurtefeu, B.; Teisseire, J.; Chateauminois, A.; Tran, Y.; Fermigier, M.; Verneuil, E. Swelling Dynamics of Surface-Attached Hydrogel Thin Films in Vapor Flows. *Langmuir* **2018**, *34* (50), 15238–15244. <https://doi.org/10.1021/acs.langmuir.8b03206>.
- (11) Gundogan, N.; Okay, O.; Oppermann, W. Swelling, Elasticity and Spatial Inhomogeneity of Poly(N,N-Dimethylacrylamide) Hydrogels Formed at Various Polymer Concentrations. *Macromol. Chem. Phys.* **2004**, *205* (6), 814–823. <https://doi.org/10.1002/macp.200300174>.
- (12) Takahashi, R.; Miyazako, H.; Tanaka, A.; Ueno, Y. Dynamic Creation of 3D Hydrogel Architectures via Selective Swelling Programmed by Interfacial Bonding. *ACS Appl. Mater. Interfaces* **2019**, *11* (31), 28267–28277. <https://doi.org/10.1021/acsami.9b05552>.
- (13) Xu, B. B.; Liu, Q.; Suo, Z.; Hayward, R. C. Reversible Electrochemically Triggered Delamination Blistering of Hydrogel Films on Micropatterned Electrodes. *Adv. Funct. Mater.* **2016**, *26* (19), 3218–3225. <https://doi.org/10.1002/adfm.201504769>.

-
- (14) Hutchinson, J. W.; Suo, Z. Mixed Mode Cracking in Layered Materials. *Advances in applied mechanics* **1991**, *29*, 63–191.
- (15) Gioia, G.; Ortiz, M. Delamination of Compressed Thin Films. *Advances in Applied Mechanics* **1997**, *33*, 119–192. [https://doi.org/10.1016/S0065-2156\(08\)70386-7](https://doi.org/10.1016/S0065-2156(08)70386-7).
- (16) Ghatak, A.; Chaudhury, M. K.; Shenoy, V.; Sharma, A. Meniscus Instability in a Thin Elastic Film. *Physics Review Letters* **2000**, *85*, 4329–4332.
- (17) Mönch, W.; Herminghaus, S. Elastic Instability of Rubber Films between Solid Bodies. *Europhysics Letters* **2001**, *53* (4), 525–531.
- (18) Vilmin, T.; Ziebert, F.; Raphaël, E. Simple View on Fingering Instability of Debonding Soft Elastic Adhesives. *Langmuir* **2010**, *26*, 3257–3260.
- (19) Lake, G. J.; Thomas, A. G. The Strength of Highly Elastic Materials. *Proceedings of the Royal Society of London Series A* **1967**, *300*, 108–119. <https://doi.org/10.1098/rspa.1967.0160>.
- (20) Akagi, Y.; Sakurai, H.; Gong, J. P.; Chung, U.; Sakai, T. Fracture Energy of Polymer Gels with Controlled Network Structures. *J. Chem. Phys.* **2013**, *139* (14), 144905. <https://doi.org/10.1063/1.4823834>.
- (21) Bouklas, N.; Landis, C. M.; Huang, R. Effect of Solvent Diffusion on Crack-Tip Fields and Driving Force for Fracture of Hydrogels. *Journal of Applied Mechanics* **2015**, *82* (8). <https://doi.org/10.1115/1.4030587>.

General conclusion and perspectives

In this study, we have investigated the link between the grafting density at the interface between hydrogel thin films and silicon substrates and the resistance to debonding of these films under the action of swelling stresses.

For that purpose, a new strategy has been developed to vary the grafting density at the gel/substrate interface by varying the amount of reactive thiol groups on the substrate. This goal was achieved by mixing reactive mercaptosilane and unreactive propylsilane at different ratios, thiol being the functional group that anchors the hydrogel to the substrate. Using a combination of XPS and ToF-SIMS, we were able to quantitatively measure the density of the thiol groups at the surface of the silicon substrate. We observed that the amount of thiol groups grafted on the substrate depends non linearly on the amount of mercaptosilane added in the reactive silane mixture, the efficiency of the grafting being drastically increased at high mercaptosilane ratios.

In order to induce debonding from well-controlled surface defects with low adhesion, we developed a new strategy that can passivate the substrate locally over well-controlled areas. We found that allyl butyl ether is a good candidate to passivate the thiol groups grafted on the silicon surface. In combination with photolithography techniques, this molecule allowed to pattern the silicon substrate with controlled line defects. Both ellipsometry microscopy and ToF-SIMS imaging confirmed the efficiency of the deposition of allyl butyl ether along the patterned defects.

Hydrogel thin films were successfully synthesized on the grafted and patterned surfaces by using Cross-Linking And Grafting (CLAG) strategy by thiol-ene click chemistry. Using this approach, we synthesized homogenous films with controlled thickness (0.1-2 μm) and swelling ratio (2-3.8) in order to vary the elastic energy available for debonding and the swelling stresses.

A homemade setup was developed, which allows to monitor the debonding mechanisms under a humid airflow ensuring steady-state swelling of the hydrogel films. We observed that hydrogel films debond according to a telephone cord mechanism for low thicknesses ($h < 1.2 \mu\text{m}$) and swelling ratios (in the range of 2.0 to 3.8). When the thickness and/or swelling ratios are larger, dendrites are formed as a consequence of increased swelling stresses inside the hydrogel (when the swelling ratio is increased), or increased elastic energy stored in the film (when thickness is increased).

We evidenced that the driving force for debonding results from localized differential swelling stresses close to the crack tip. Indeed, the hydrogel bonded to the substrate can swell only in one direction, while the delaminated hydrogel film can swell freely in all directions, making it possible to absorb more water. The delamination mechanism we evidenced for swollen hydrogel films is thus completely different from the widely acknowledged buckling instabilities involved in the debonding of rigid coatings.

The debonding velocity was systematically measured when hydrogel debonds over the grafted substrate. We evidenced that it progressively vanishes with time except for thicker samples and lower grafting density samples. This decrease in the debonding velocity was related to the appearance of a wavy debonding line with finger-like instabilities. From an estimate of the free energy density stored in the swollen film in plane strain or plane stress conditions, we proposed that the development of the finger-like instabilities could be attributed to differences in the release of the lateral constraints close to the crack tip depending on the curvature of the debonding line.

A better understanding of these mechanisms would require a more refined study debonding as a function of the curvature of the crack front. For that purpose, we could benefit from the versatility of the patterning techniques we have developed to realize silicon substrates patterned with disk defects with different radius.

In order to account progressive development of wavelength of the finger-like instabilities, it would also be interesting to have a more detailed analysis of the deformation state of the film close to the crack tip. For the analysis of our experiments, we assumed that a uniform plain strain state along the debonding line. However, we observed that the debonded film folded extensively at some distance from the delamination front. It would therefore be interesting to know how such a folding could affect the homogeneity of the deformation of the delaminated

part of the film very close to the crack tip. For that purpose, we could develop interferometric measurements of the gap between the film and the substrate close to the crack front.

The debonding rate is found to decrease over nearly two orders of magnitude when the amount of mercaptosilane in the reactive silane mixture is increased from 20% to 100%, *i.e.*, when the surface density of thiol groups available for grafting is increased from 0.1 to 0.6 nm⁻². A threshold thickness for the occurrence of debonding is also observed, which increases with the amount of mercaptosilane used to graft the substrate.

In order to discuss the experimental observations, we developed a fracture mechanics model taking into account the non linearities of the swollen film. From this model, we derivated an expression of the threshold interface fracture energy corresponding to the onset of debonding at the thickness threshold. The values of this threshold fracture energy obtained from the model are consistent with independent estimates based on the determination of the energy required to break the covalent bonds between the hydrogel and the substrate. This agreement is justified by the fact that the threshold fracture energy determined from the model using the experimental threshold thickness corresponds to an equilibrium state, where no significant viscous dissipation at the crack front due to water transport is involved. A better understanding of the changes in the debonding velocity when the grafting density is varied would require much more involved numerical calculations of the energy release rate in the presence of poroelastic water flow within the hydrogel network close to the crack tip.

Our studies revealed that the durability of the film under the action of swelling stresses could be improved by increasing the grafting density or decreasing thickness. At the same time, for anti-mist coatings, a higher delay in mist formation requires higher thicknesses and swelling ratios. This contradictory requirement may be conciliated by the development of multi-layered films. As an example, it could be advantageous to make a multi-layered film in which a first layer of hydrogel with high crosslink and grafting density to the substrate would promote a good interface strength, while a second layer on top of the first layer with a higher swelling ratio would form a good reservoir to delay mist formation.

APPENDIX A

Spectroscopic ellipsometry

The thickness of hydrogel films deposited on an oxidized silicon substrate was measured using a spectroscopic ellipsometer UNISEL (Horriba Jobin Yvon) with wavelength (λ) ranging from 400 to 800 nm in air and water. The angle of incidence is always kept constant at 60° . In situ swelling thickness was measured by sealing the sample in a cell filled with water with two thin glass walls perpendicular to the incident and reflected light.

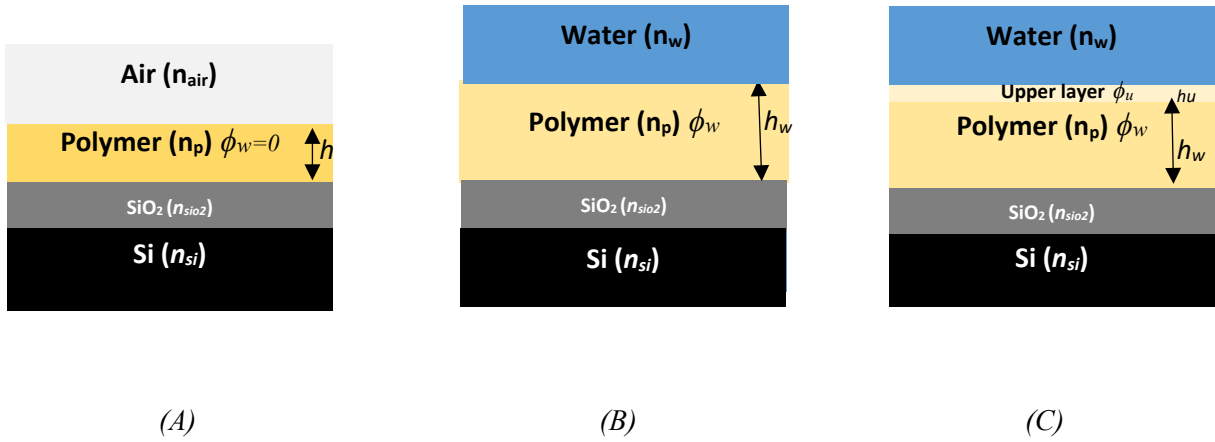


Figure 1: Schematic of a polymer film deposited on an oxidized silicon wafer in the presence of (A) air, and (B) water. In (B): swollen polymer/water interface is sharp. In (C): swollen hydrogel with an upper layer of thickness h_u .

The IS and IC are ellipsometric intensities which vary with wavelength (λ) and are measured and compared to simulated variations with λ using a model with several layers separated by sharp interfaces as depicted in Figure 1 (A, B). We will discuss the hypothesis of a sharp interface with water at the end of this Appendix (figure 1.C). IS and IC are the functions of ellipsometric angles Δ and ψ , where

$$IS = \sin(2\psi) * \sin(\Delta) \quad \text{Eq. 1}$$

$$IC = \sin(2\psi) * \cos(\Delta) \quad \text{Eq. 2}$$

The complex refractive index (n_{si}) used for silicon wafer is $3.93 + 0.002i$ at 600 nm wavelength. The second layer contains SiO_2 ($n = 1.46$ at λ is 600 nm) which is measured by ellipsometry prior to the film deposition.

Here we use a Cauchy transparent model to describe the variation of the refractive indices of both the dry polymer n_p and water n_w with the wavelength λ which is given by the Eq 3. These A, B, and C values are different for each material and also with different water volume fraction ϕ_w in the hydrogel.

$$n(\lambda) = A + \frac{B \cdot 10^4}{\lambda^2} + \frac{C \cdot 10^9}{\lambda^4} \quad \text{Eq. 3}$$

As A, B, C values for dry PDMA film is unknown, we use the A, B and C values of PMMA from the literature¹. The values of A, B and C of water is also taken from literature². These values are given in table 1.

| | A | B | C |
|----------------|----------|----------|----------|
| Polymer | 1.479 | 0.548 | -0.172 |
| water | 1.32 | 0.519 | -0.256 |

Table 1: A, B and C values for Cauchy transparent model for dry polymer and water refractive indices (see eq.3).

The refractive index of swollen gel (n) layer depends on the volume fraction (ϕ_w) of water in the gel. A simple mixing rule can be assumed to describe the variations of n with ϕ_w as in equation 4.

$$n(\lambda, \phi_w) = \phi_w n_w(\lambda) + (1 - \phi_w) n_p(\lambda) \quad \text{Eq. 4}$$

Where ϕ_w is calculated by eq. 5 with swelling thickness h_w . The swelling thickness h_w of a hydrogel can be measured by keeping swollen thickness as a fitting parameter while ellipsometric intensities IS and IC were adjusted using a three-layered model as in Figure 1(B) with sharp interfaces between layers.

$$\phi_w = \frac{h_w - h}{h_w} \quad \text{Eq. 5}$$

Where h is the dry thickness of the film.

Measurement of dry film thickness

The dry thickness h of hydrogel film is measured first. All the measurements were done at 5 nm increment steps for the wavelength λ from 400-800 nm. Figure 2 shows the variations of the IS and IC as a function of the wavelength λ measured in air for two samples from same mother batch where the concentration of the polymer is varied. Ellipsometric intensities IS and IC are adjusted using a three-layered model as shown in Figure 1(A) with dry thickness h as a fitting parameter. It is observed from figure 2 that for both samples, the fit is very well superimposed, and their thickness was noted. This confirms that there is a sharp layer between each interface and Cauchy model with parameters from Table 1 for n_p is valid. As expected, the increase in thickness is consistent with the concentration of the polymer solution used to make the films (chapter 2: Figure 2).

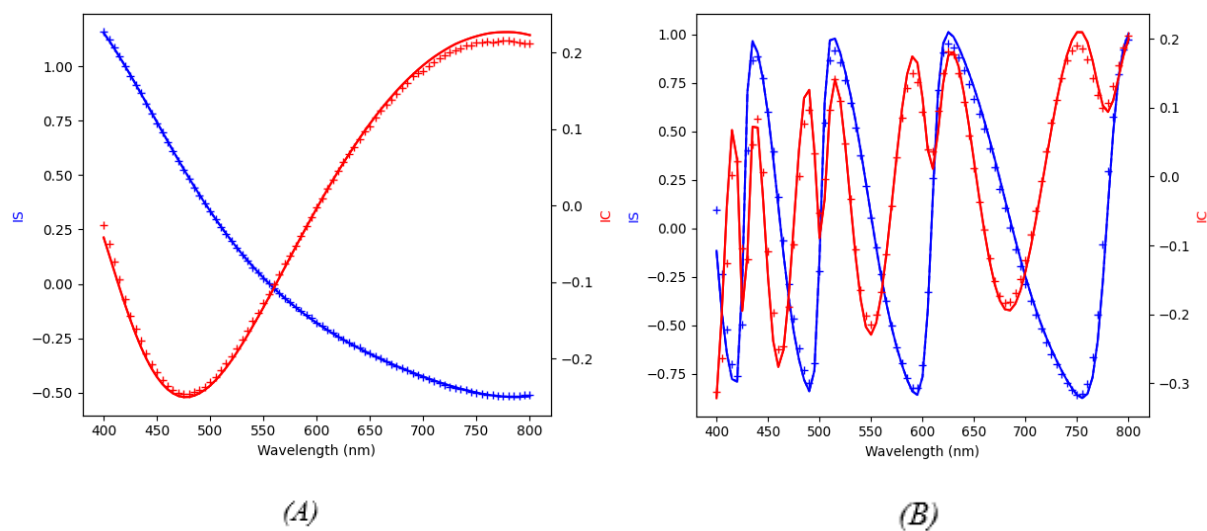


Figure 2 variations of the ellipsometric intensities IS and IC as a function of the wavelength for two samples from the same mother batch. The best fit to the model was obtained for thickness h : (A) $h = 193$ nm, and (B) $h = 1100$ nm.

Measurement of swollen film thickness

The swelling thickness h_w of the same hydrogel samples immersed in water was measured by the ellipsometer. Here all the measurements are done at 1 nm increment steps for the wavelength λ . Figure 3 shows the variations of the IS and IC as a function of the wavelength λ measured in water.

Ellipsometric intensities IS and IC were first adjusted using a three-layered model as in Figure 1(B) with sharp interfaces between layers with swollen thickness h_w as a fitting parameter. With Eqs. 3, 4, and 5, the ellipsometric intensities only depend on h_w consistently.

It is observed from figure 3(A) where the dry thickness h is 193 nm, the fit is very well-superimposed with the data. The swollen thickness h_w obtained is noted and the water volume fraction ϕ_w of the film is calculated by eq. 5 and shown in table 2.

In figure 3 (B) the dry thickness h of the sample is 1100 nm. It can be seen in Figure 3 (B) that the fit is not superimposing in amplitude even though the periods of oscillation are the same as the data. This may be due to the hypothesis of a sharp interface between hydrogel and water layer during swelling. We nevertheless report the swollen thickness h_w and volume fraction ϕ_w in Table 2.

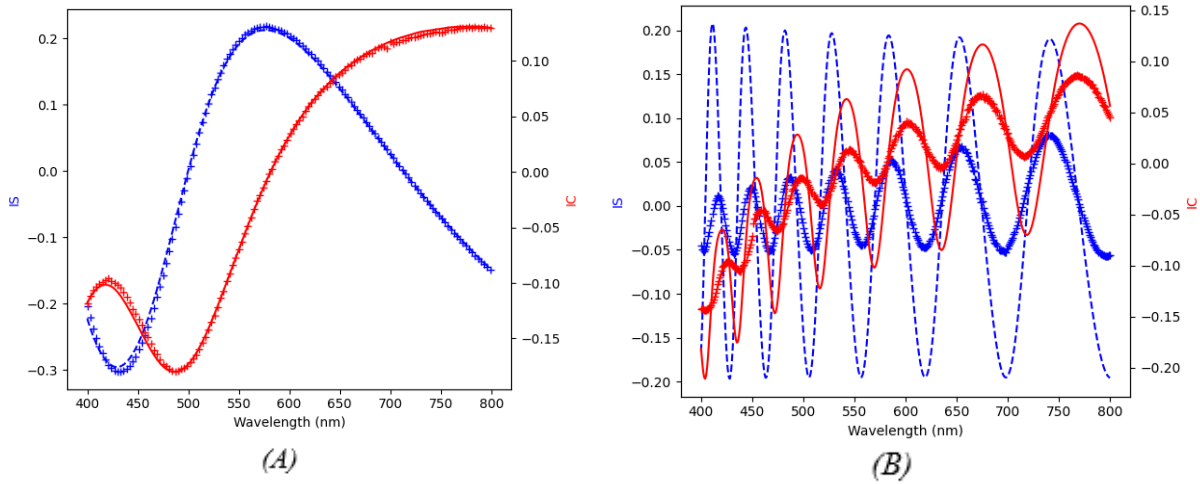


Figure 3: variations of the ellipsometric intensities IS and IC as a function of the wavelength for two samples whose dry thickness h are (A) 193 nm, and (B) 1100 nm. The best fit to the model (figure 1.B) is obtained for swollen thickness h_w : (A) 452 nm, and (B) 3450 nm.

| Dry thickness h (nm) | Swelling thickness h_w (nm) | ϕ_w |
|------------------------|-------------------------------|----------|
| 193 | 452 | 0.57 |
| 1100 | 3450 | 0.66 |

Table 2: Water volume fraction ϕ_w is measured using eq 5 with dry thickness from figure 2 and swelling thickness from figure 3

Now, in order to improve the fit for the thicker samples, we are considering the swollen hydrogel not as a single layer, but as two layers (Figure 1.C) with a top layer which can swell more than the rest of the hydrogel. In this model, we keep the bottom (bulk) layer thickness h_w and volume fraction ϕ_w as measured with model 1(B) and we adjust the thickness h_u of the upper layer. In Figure 4, we can see a better fit and we measured the upper layer thickness h_u and calculated the upper water volume fraction ϕ_u of the swollen film. Here ϕ_u is 0.84 while ϕ_w is only 0.66. This means that the upper layer swells more than the bulk layer.

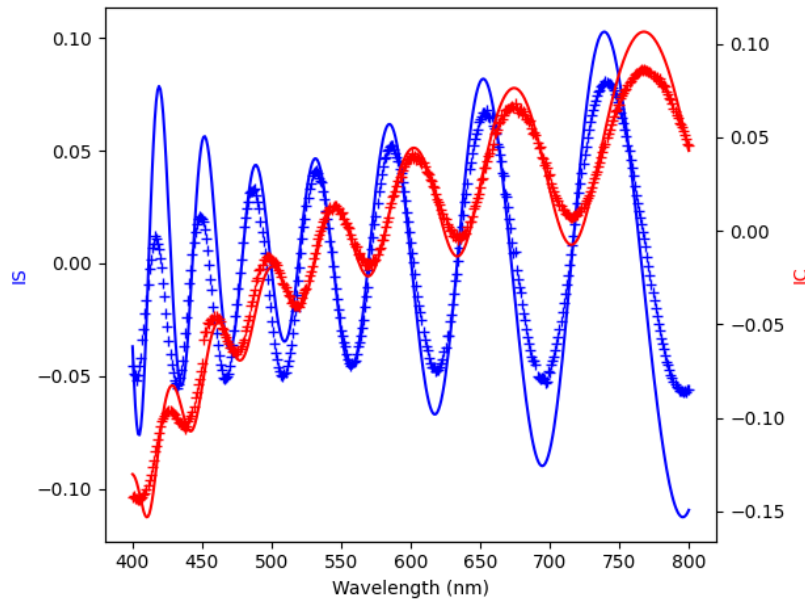


Figure 4: variations of the ellipsometric intensities IS and IC as a function of the wavelength for the sample with a dry thickness h of 1100 nm. The best fit to the model is obtained from a four-layer model (Figure 1.C). The swollen thickness of the bulk layer of the hydrogel is kept as in the model figure 1(B) is $h_w = 3450$ nm. $\phi_w = 0.66$. The upper layer thickness measured from the four-layer model where $h_u = 160$ nm and water volume fraction ϕ_u is 0.84.

The swelling thickness of samples with different grafting densities.

We systematically measured the ellipsometric intensities on samples with different grafting densities (25-100%) of thiol and different thicknesses h (50-1200 nm) made from same polymer batch synthesized. The results were analyzed with model 1B first to get h_w and ϕ_w , then model 1C is used to measure h_u and ϕ_u . Figure 5 shows the water volume content ϕ_w and ϕ_u and swollen film thicknesses h_w and h_u as a function of dry thickness h for different grafting densities.

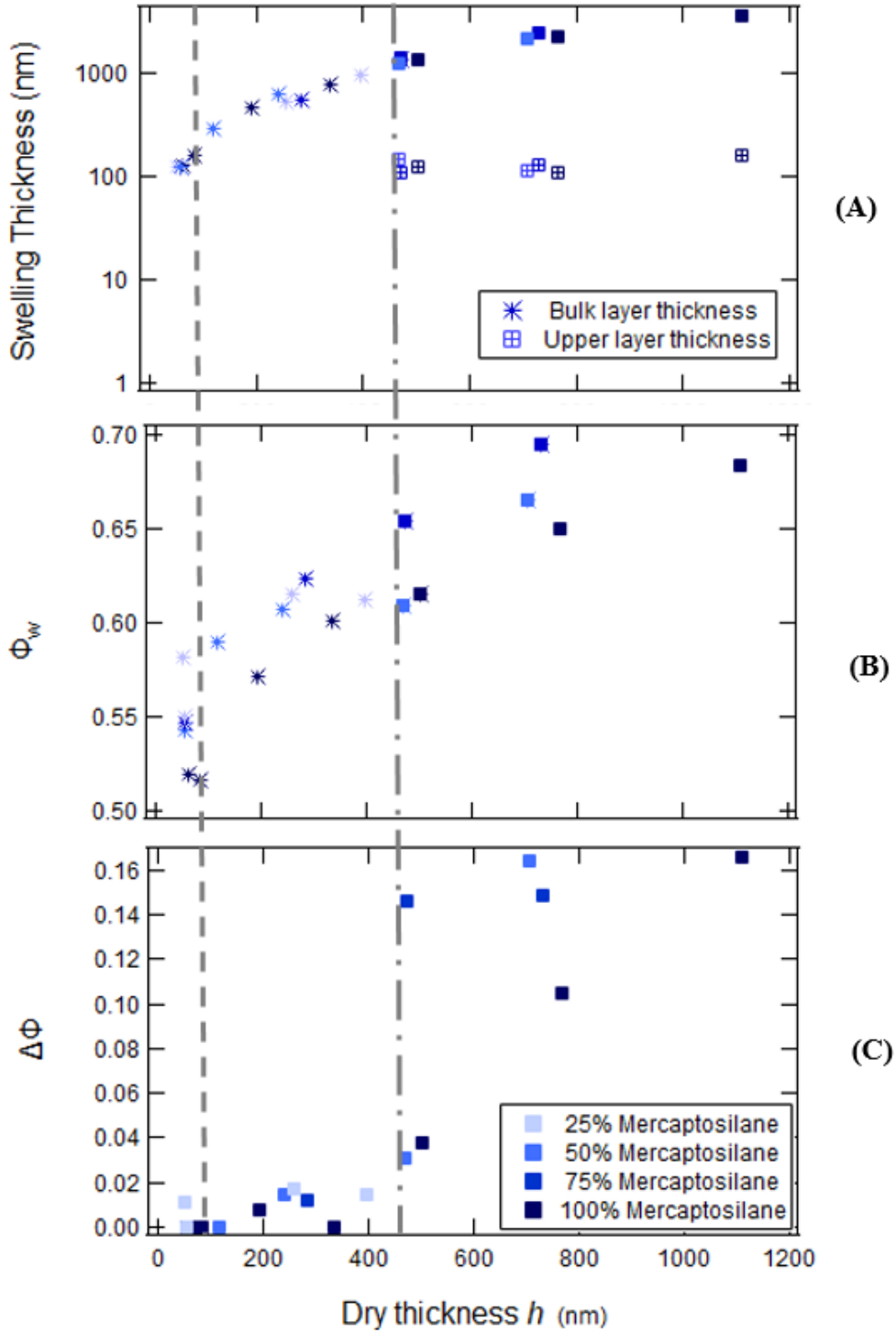


Figure 5. The study of swelling of PDMA as a function of the dry thickness h of hydrogel film for grafting density of 25%, 50%, 75%, and 100% mercaptosilane. (A) The swelling thicknesses of the bulk layer and upper layer, (B) The water fraction ϕ_w in the bulk layer, (C) Difference between water fraction $\Delta\phi$ in the upper layer ϕ_u and bulk layer ϕ_w as a function of the dry thickness h of PDMA film.

In figure 5(A), the swelling thickness of the bulk layer is plotted as a function of the dry thickness h of the film in a log-lin plot. The swelling thickness h_w of the bulk layer increases with the dry thickness h as expected.

Figure 5 (B) depicts the water volume fraction ϕ_w as a function of dry thickness h . Below dry thickness $h = 100$ nm, it is observed from figure 5 (B) that ϕ_w is only 0.52 for 100% mercaptosilane sample which is lower compared to samples above 100 nm. And it can be seen from figure 5 (B) that below 100 nm, the ϕ_w is sensitive to grafting density while above it doesn't. These observations are in line with previous results when ϕ_w was measured by neutron reflectivity to understand the decrease in thicknesses below 100 nm due to substrate effect.³ So, the larger the grafting density, the larger the effect of the substrate on the hydrogel swelling.

Above 100 nm, the ϕ_w increases with dry thickness h . The reason for this is unknown for now and would need further studies. Currently, in our studies, we have taken ϕ_w as an average which is 0.62 ± 0.04 .

From the model (Figure 1.C), we have seen that there is an upper layer on the surface of the hydrogel. In Figure 5 (C) the difference between the water volume fraction ($\Delta\phi$) of bulk layer ϕ_w and upper layer ϕ_u is plotted as a function of dry thickness h . In figure 5 (C), $\Delta\phi$ is almost zero below 470 nm. Above 470 nm, there is a sharp increment of $\Delta\phi$ of 0.16. That means the upper layer exists only for thicknesses greater than 470 nm.

In figure 5 (A), the swelling thickness of the upper layer h_u is plotted as a function of the dry thickness h of the film on a log-lin plot. It can be observed in figure 5 (A) that the upper layer thickness is around 100 nm irrespective of the thickness of the film and grafting density. So, the samples where thickness is above 470 nm have an upper layer with higher water content, and its thickness is always around 100 nm.

From our studies, we saw that there is an upper layer in swollen hydrogel film, which comes to valid only after a certain threshold thickness where ϕ_u sharply increases. This may be connected to the wrinkles (chapter 2:3.4) on the surface of the hydrogel. We observed that the wrinkles exist only above a threshold thickness where buckling of the free surface occurs and the wavelength of these wrinkles increases with thickness. This may lead to the accumulation of more water content on the upper layer.

A different batch of polymers where the water volume content ϕ_w was supposed to be higher was used to do similar studies and compared the main results with the first series. Figure 6

shows the water volume content ϕ_w and ϕ_u and swollen film thicknesses h_w and h_u as a function of dry thickness h .

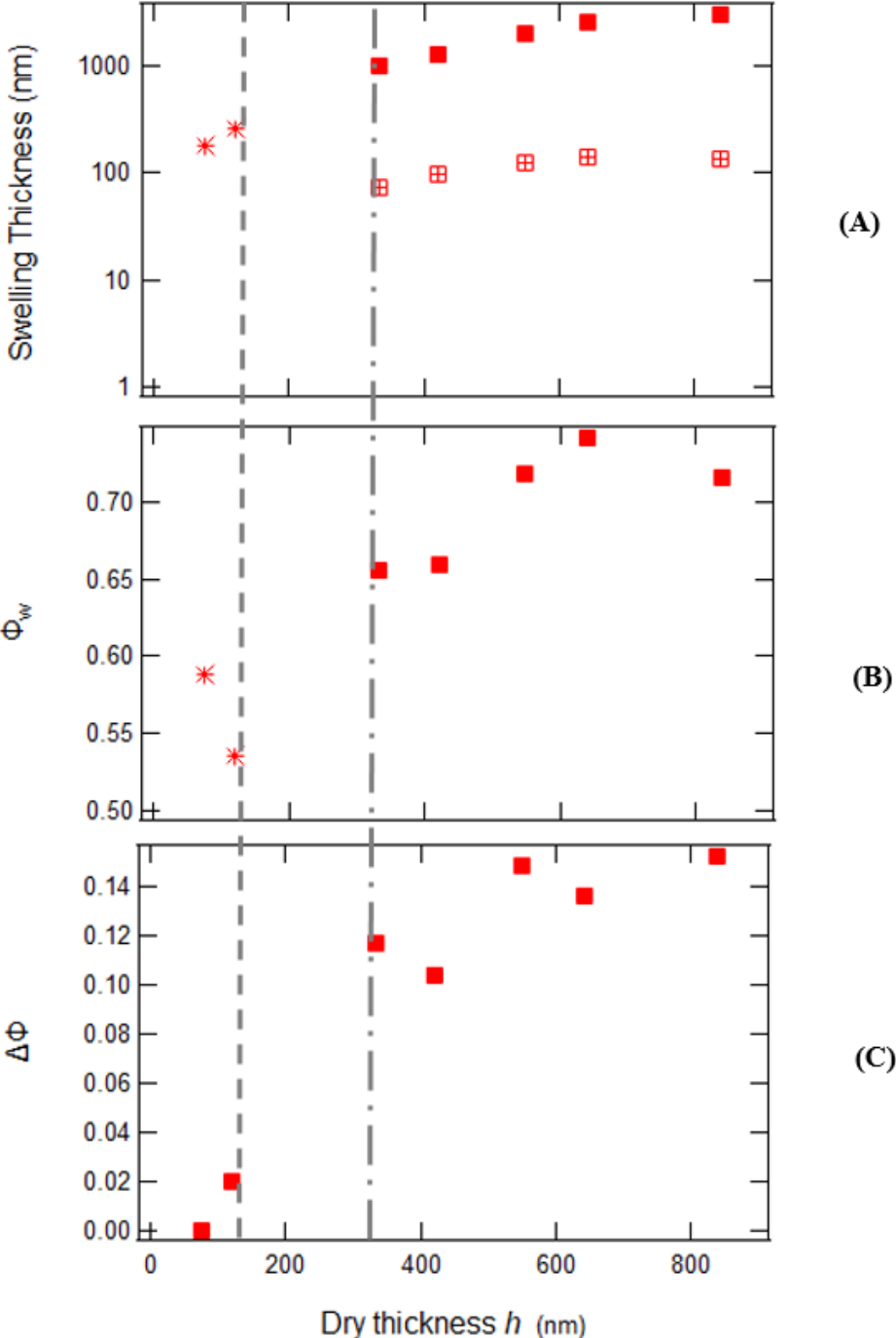


Figure 6. The study of swelling of PDMA as a function of the dry thickness of hydrogel film for grafting density of 100% mercaptosilane. (A) The swelling thicknesses of the bulk layer and upper layer, (B) The water fraction ϕ_w in the bulk layer, (C) Difference between water fraction $\Delta\phi$ in the upper layer ϕ_u and bulk layer ϕ_w as a function of the dry thickness of PDMA film.

In figure 6 (A), the swelling thickness of the bulk layer h_w and the swelling thickness of the upper layer h_u is plotted as a function of the dry thickness h of the film on a log-lin plot. It can be observed that there is an upper layer and the thickness of the upper layer is 100 nm irrespective of the dry thickness of the film, similar to the results we observed from first series.

Figure 6 (B) depicts the water volume fraction ϕ_w as a function of dry thickness h . From figure 6 (B) the average water volume fraction ϕ_w is 0.7 ± 0.04 which is higher than the water volume fraction ϕ_w of the first series.

In Figure 6 (C) the difference between the water volume fraction ($\Delta\phi$) of bulk layer ϕ_w and upper layer ϕ_u is plotted as a function of dry thickness. It can be observed from figure 6 (C) that the threshold thickness to have an upper layer is 332 nm. The threshold thickness is lower compared to Figure 5(C). The threshold thickness to have an upper layer decreases with increase in water volume fraction ϕ_w , which is consistent with the fact that the threshold thickness for buckling on the surface decreases with higher ϕ_w .

For samples around 332 nm, the wrinkles are so small that it is impossible to identify in a microscope. However, wrinkles were observed on samples of dry thickness $h = 332$ nm and $h_w = 996$ nm for $\phi_w = 0.7 \pm 0.04$ with AFM (shown in Figure 7). The amplitude of the wrinkles is around 70 nm and the wavelength of the wrinkles is around 780 nm. We observe that the amplitude of the wrinkles is consistent with the upper layer thickness h_u : they both range in 100 nm.

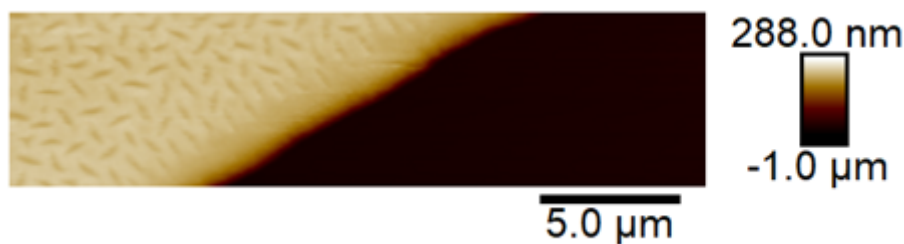


Figure 7. AFM image of the surface of substrate-attached PDMA hydrogel films swollen with water where dry thickness $h = 332$ nm and $h_w = 996$ nm. The black part of the image at the bottom right corner is the silicon wafer due to the scratch made during measurement. Next to it the hydrogel is swollen and its surface wrinkles. The amplitude of the wrinkles is around 70 nm and the wavelength is around 780 nm.

References

- (1) Soave, P. A. Refractive Index Control in Bicomponent Polymer Films for Integrated Thermo-Optical Applications. *Opt. Eng.* **2009**, 48 (12), 124603. <https://doi.org/10.1117/1.3275452>.
- (2) Bashkatov, A. N.; Genina, E. A. Water Refractive Index in Dependence on Temperature and Wavelength: A Simple Approximation; Tuchin, V. V., Ed.; 2003; pp 393–395. <https://doi.org/10.1117/12.518857>.
- (3) Li, M.; Bresson, B.; Cousin, F.; Fretigny, C.; Tran, Y. Submicrometric Films of Surface-Attached Polymer Network with Temperature-Responsive Properties. *Langmuir* **2015**, 31 (42), 11516–11524. <https://doi.org/10.1021/acs.langmuir.5b02948>.

APPENDIX B

Theoretical interface crack model

We have shown experimentally that swelling induced delamination only occurs above a thickness threshold. In what follows we derive a theoretical fracture mechanics model to describe the *equilibrium* interface crack corresponding to this threshold. More specifically, we are addressing a situation where the gel layer close to the crack is assumed to be at swelling equilibrium, *i.e.* the chemical potential of the solvent molecules is constant throughout the gel network. Such an assumption would no longer be valid in the case of a *propagating* interface crack where energy dissipation due to solvent flow at the crack tip should be accounted for, which would require a much more involved analysis.

A classical linear elastic fracture mechanics (LEFM) approach to the debonding threshold would rely on the determination of the amount of energy which is released when the bonded, constrained layer, separates from the substrate and then swells further. However, upon swelling, the volume of the hydrogels films under consideration is increasing by a factor of two or three. Under such conditions a linear analysis using an infinitesimal strain assumption is no longer valid. Instead, a finite strain approach should be considered where a difference is made between the *reference* configuration (the unswollen gel film) and the *current* configuration (here, the gel at swelling equilibrium) and where the non linearities of the material response are accounted for.

Here, such an analysis is developed in the limit of a straight crack line propagating along the direction denoted as 1 in Fig. 1, *i.e.* during the initial stages of delamination. The main assumption of the model is that debonding arises from the localized stresses which results from the differential swelling of the film in the bounded and delaminated states. Specifically, we make the assumption that close to the crack tip, the delaminated film is allowed to swell only in directions 1 and 2, *i.e.* the film is a plane strain deformation state, while in the bonded part the film is only allowed to swell in direction 2 by virtue of lateral constraints.

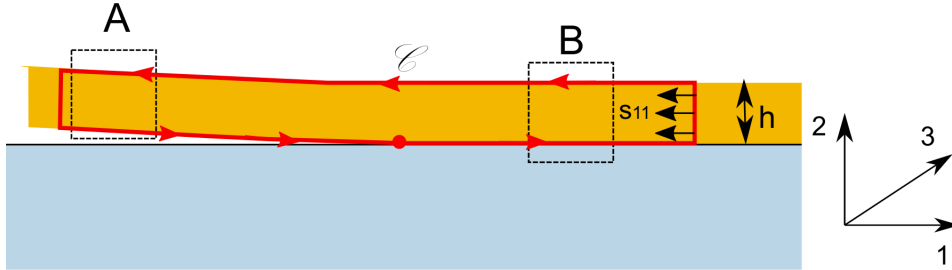


Figure 1: Reference configuration of the delaminated gel film of thickness h on a rigid substrate (before swelling). At point A , the material undergoes free swelling in plane strain, whereas at B material is constrained to swell only in direction 2. The out of plane direction is 3. Due to plane strain, the gel film at B is under in-plane bi-axial stress. C is the contour (red line) over which the \mathcal{J} -integral in Eq. (1) is evaluated.

Following the theoretical work by Bouklas *et al.* [1] for fracture in hydrogel systems, we use to determine the threshold energy release rate $\Gamma \equiv \Gamma_0$ a modified form of the path-independent \mathcal{J} -integral approach initially developed by Rice [2]. Accordingly, Γ_0 is evaluated using the following contour integral \mathcal{J} , where the usual elastic strain energy density is replaced by the

Grand potential \widehat{W}

$$\Gamma \equiv \mathcal{J} = \int_{\mathcal{C}} \left(\widehat{W}_B(\mathbf{F}_B, \mu) N_2 - s_{iJ} N_J \frac{\partial x_i}{\partial X_1} \right) dS \quad (1)$$

where X and x denote the coordinates in the reference and deformed configuration, respectively. \mathbf{F} is the deformation gradient tensor which is introduced to map the material coordinates in the reference and current configurations. N_J is the outward unit normal on the boundary of the reference configuration and s_{iJ} is the nominal (Piola-Kirchoff) stress.

$\widehat{W} = W - \mu C$ is the Grand free energy density in which the independent variables are the deformation gradient tensor \mathbf{F} and the chemical potential μ of the solvent molecules [3] ($W = W_m + W_e$ where W_m and W_e are the mixing and elastic free energy, respectively; C is the concentration of solvent molecules). An evaluation of the \mathcal{J} -integral along the contour \mathcal{C} (Fig. 1) yields

$$\Gamma = h \left[\left(\widehat{W}_B(\mathbf{F}_B, \mu) - s_{11}(B) \right) - \left(\widehat{W}_A(\mathbf{F}_A, \mu) \right) \right] \quad (2)$$

where the subscripts A and B denote that the quantity \widehat{W} is evaluated at A and B (see Fig. 1).

Here we have considered that the gel is in a state of equilibrium and that the chemical potential μ of the solvent molecules within the gel is homogeneous and equal to that of the solvent outside the network. In the above expression, we also made the assumption that the only relevant stress in the bonded part of the gel is the true compression swelling stress s_{11} and that the delaminated part of the gel film is traction free which is justified by the extensive folding of the debonded film which is observed experimentally.

According to Hong et al. [4], the Grand free energy can be written as

$$\widehat{W}(\mathbf{F}, \mu) = \frac{G_0}{2} (I - 3 - 2 \ln J) - \frac{kT}{\nu} \left[(J - 1) \ln \frac{J}{J - 1} + \frac{\chi}{J} \right] - \frac{\mu}{\nu} (J - 1) \quad (3)$$

where $J = \det \mathbf{F}$, $I = \text{Tr}(\mathbf{F}^T \mathbf{F})$, G_0 is the shear modulus of the drained network and ν is the volume of a solvent molecule. In the above expression, the first term is the right hand side corresponds to elastic free energy W_e , the second one to the mixing free energy W_m and the last term to $-\mu C$.

In plane strain (A), $\lambda_1 = \lambda_2 = \lambda_A$, $\lambda_3 = 1$. The above expression of the Grand free potential thus reads

$$\widehat{W}_A(\mathbf{F}_A, \mu) = G_0 (\lambda_A^2 - 1 - \ln \lambda_A^2) - \frac{kT}{\nu} \left[(\lambda_A^2 - 1) \ln \frac{\lambda_A^2}{\lambda_A^2 - 1} + \frac{\chi}{\lambda_A^2} \right] - \frac{\mu}{\nu} (\lambda_A^2 - 1) \quad (4)$$

For the bonded film (B), $\lambda_1 = \lambda_3 = 1$, $\lambda_2 = \lambda_B$. $\widehat{W}_B(\mathbf{F}_B, \mu)$ thus writes

$$\widehat{W}_B(\mathbf{F}_B, \mu) = G_0 (\lambda_B^2 - 1 - 2 \ln \lambda_B^2) - \frac{kT}{\nu} \left[(\lambda_B - 1) \ln \frac{\lambda_B}{\lambda_B - 1} + \frac{\chi}{\lambda_B} \right] - \frac{\mu}{\nu} (\lambda_B - 1) \quad (5)$$

According to the description of swelling equilibrium detailed in the main text (chapter 3), the relationships between the equilibrium swelling ratio λ_A, λ_B and the chemical potential μ is given by

$$\frac{\mu}{\nu} = G_0 \left(1 - \frac{1}{\lambda_A^2} \right) - \frac{kT}{\nu} \left[\ln \frac{\lambda_A^2}{\lambda_A^2 - 1} - \frac{1}{\lambda_A^2} - \frac{\chi}{\lambda_A^4} \right] \quad (6)$$

$$\frac{\mu}{\nu} = G_0 \left(\lambda_B - \frac{1}{\lambda_B} \right) - \frac{kT}{\nu} \left[\ln \frac{\lambda_B}{\lambda_B - 1} - \frac{1}{\lambda_B} - \frac{\chi}{\lambda_B^2} \right] \quad (7)$$

The free energy at A can be expressed in term of λ_A only by substituting (6) into (4) to eliminate the chemical potential, *i.e.*

$$\widehat{W}_A(\mathbf{F}_A, \mu) = G_0 \left(\frac{\lambda_A^2 - 1}{\lambda_A^2} - \ln \lambda_A^2 \right) - \frac{kT}{\nu} \left[1 + \frac{2\chi - 1}{\lambda_A^2} - \frac{\chi}{\lambda_A^4} \right] \quad (8)$$

In the same way, substituting (7) into (5) and taking $\sigma_{11}(B) = -G_0(\lambda_B - 1/\lambda_B)$, we get after some algebra

$$\widehat{W}_B(\mathbf{F}_B, \mu) - s_{11}(B) = \frac{G_0}{2} (\lambda_B^2 - 1 - 2 \ln \lambda_B) + G_0 \left(\frac{\lambda_B - 1}{\lambda_B} \right) - \frac{kT}{\nu} \left[1 + \frac{2\chi - 1}{\lambda_B} - \frac{\chi}{\lambda_B^2} \right] \quad (9)$$

According to eqn. (4), (5) and (2), the threshold energy release rate for debonding is then given by

$$\begin{aligned} \frac{\Gamma_0}{Gh} = & \left[\frac{\lambda_B - 1 - 2 \ln \lambda_B}{2} + \ln \lambda_A^2 + \frac{1}{\lambda_A^2} - \frac{1}{\lambda_B} \right] \\ & + \frac{kT}{\nu G_0} \left[(2\chi - 1) \left(\frac{1}{\lambda_A^2} - \frac{1}{\lambda_B} \right) + \frac{\chi}{\lambda_B^2} - \frac{\chi}{\lambda_A^4} \right] \quad (10) \end{aligned}$$

Bibliography

- [1] Nikolaos Bouklas, Chad M. Landis, and Rui Huang. Effect of Solvent Diffusion on Crack-Tip Fields and Driving Force for Fracture of Hydrogels. *Journal of Applied Mechanics*, 82(8):081007, August 2015.
- [2] J. R. Rice. A path independent integral and the approximate analysis of strain concentration by notches and cracks. *Journal of Applied Mechanics*, 35(2):379–386, 1968.
- [3] Wei Hong, Zishun Liu, and Zhigang Suo. Inhomogeneous swelling of a gel in equilibrium with a solvent and mechanical load. *International Journal of Solids and Structures*, 46(17):3282–3289, August 2009.
- [4] Wei Hong, Xuanhe Zhao, Jinxiong Zhou, and Zhigang Suo. A theory of coupled diffusion and large deformation in polymeric gels. *Journal of the Mechanics and Physics of Solids*, 56(5):1779–1793, May 2008.
- [5] P. J. Flory and J. Rehner. Statistical mechanics of crosslinked polymer networks. ii swelling. *journal of Chemical Physics*, 11(11):521–526, 1943.

RÉSUMÉ

Les revêtements d'hydrogel sont des réseaux de polymères transparents et hydrophiles capables d'absorber plusieurs fois leur épaisseur en eau. Cependant, les contraintes induites par le gonflement du film peuvent entraîner un décollement préjudiciable de l'hydrogel ce qui peut limiter l'utilisation pratique de ces revêtements. Dans cette étude, nous proposons de décrire les mécanismes de décollement de films minces d'hydrogel en fonction de leur densité de greffage à l'interface film/substrat. Le but est de pouvoir contrôler et prédire la dégradation des revêtements hydrogel pendant le gonflement ou sous des contraintes de contact. Dans ce but, nous avons développé une méthodologie permettant de mesurer l'initiation et la propagation de la délamination induite par le gonflement de films minces d'hydrogel à partir de défauts d'interface préexistants bien contrôlés.

Des films minces d'hydrogel de poly(diméthylacrylamide) (PDMA) attachés à la surface sont préparés sur des plaquettes de silicium à partir de la réticulation et du greffage simultanés (CLAG) de chaînes polymères fonctionnalisées par la chimie click thiol-ène. Cette stratégie permet de faire varier l'épaisseur du film (0.1 - 2 μm) et de contrôler le taux de gonflement du réseau, ici fixé à 2, tout en assurant une densité de réticulation homogène. Afin de faire varier la résistance de l'interface film/substrat, le substrat en silicium est greffé avec des mélanges de mercaptosilane (réactif) et de propylsilane (inerte) dans différentes proportions avant le dépôt du film mince. Alors que le mercaptosilane est capable de former des liaisons covalentes avec le réseau PDMA, le propylsilane ne réagit pas, ce qui permet de contrôler le taux de greffage du film mince d'hydrogel sur le substrat. Nous caractérisons la fraction de surface de mercaptosilane ainsi obtenue par des analyses XPS et TOF-SIMS. Par ailleurs, toujours à l'interface substrat/film, des défauts linéaires bien contrôlés ayant une faible adhérence (largeur entre 10 et 100 μm) sont créés sur le substrat en passivant de façon localisée les groupes thiol réactifs par microlithographie. Ces défauts nucléent le décollement des films de façon bien localisée, ce qui permet ensuite de suivre la propagation de la décohésion à partir de ces défauts.

Le décollement du film induit par le gonflement est réalisé sous un flux de vapeur constant assurant la saturation du film en eau. En observant le décollement progressif du film à partir des défauts linéaires préexistants, nous retrouvons un motif d'instabilité classique dit de fil de téléphone et nous montrons que le décollement résulte de contraintes de gonflement localisées proche de la ligne de décollement. Nous mesurons la vitesse de propagation du décollement dans la zone où le film est greffé sur le substrat et nous observons qu'elle augmente de deux ordres de grandeur lorsque la quantité de propylsilane dans le mélange de silanes réactifs passe de 0 à 90 %, c'est-à-dire lorsque le taux de greffage du film décroît. Un seuil d'épaisseur pour le décollement est également observé, les films pouvant se décoller étant d'autant plus minces que le taux de greffage du film est faible. Les mesures de ce seuil sont discutées à partir d'un argument simple de mécanique de la rupture qui permet de rendre compte semi quantitativement de nos mesures.

MOTS CLÉS

Films minces d'hydrogel, Interface hydrogel/substrat, Greffage, Défaut interfacial, Résistance interfaciale, Décollement, Contraintes de gonflement.

ABSTRACT

Hydrogel coatings are transparent and hydrophilic polymer networks that absorb a lot of water and can be suitable candidates for anti-mist coatings. However, swelling-induced stresses within the film can result in detrimental debonding of hydrogel and may fail. In this study, these debonding processes are investigated in the relation to the grafting density at the film/substrate interface, so as to control and predict the failure of the coatings during swelling or under contact stresses. For that purpose, we have developed a methodology consisting in monitoring the initiation and the propagation of swelling-induced delamination from well-controlled preexisting interface defects.

Surface-attached poly(dimethylacrylamide) (PDMA) hydrogel thin films are prepared on silicon wafers from the simultaneous Cross-Linking And Grafting (CLAG) of functionalized polymer chains by thiol-ene click chemistry. This strategy allows to tune the film thickness (0.1-2 μm) while ensuring a homogeneous crosslinking density. In order to vary the strength of the film/substrate interface, the silicon wafer is grafted by mixing reactive mercaptosilane and unreactive propylsilane in various proportions prior to the formation of the hydrogel film. We characterize the mercaptosilane surface fraction thus obtained by XPS and TOF-SIMS analyses. Well-controlled line defects (width between 2 and 100 μm) are also created to nucleate delamination of the hydrogel from the substrate.

Swelling-induced debonding of the film is achieved under a constant vapor flow ensuring water saturation. Optical observations show the progressive debonding of the film from the pre-existing line defects under the action of localized swelling stresses. We obtain delamination pattern of typical so-called telephone cord instability. We measure the propagation velocity where the hydrogel is grafted to the substrate. The debonding rate is found to decrease over two orders of magnitude when the amount of mercaptosilane in the reactive silane mixture is increased from 10% to 100% while increasing the covalent bonds between hydrogel and substrate. A threshold thickness for debonding is also observed. This threshold thickness increases with the amount of mercaptosilane used to graft the substrate. We derived quantitative values of the interface fracture energy from the measured thickness threshold with a simple fracture mechanics model.

KEYWORDS

Hydrogel thin films, Hydrogel/substrate interface, Grafting, Interfacial defect, Interfacial strength, Delamination, Telephone cord instability, Swelling stresses.